

## ABSTRACT

Title of Dissertation:                   IMPROVING THE SPEED AND OPTICAL  
SECTIONING OF FLUORESCENCE  
MICROSCOPY TECHNIQUES FOR  
BIOPHYSICAL ANALYSIS OF  
SUBCELLULAR PROCESSES

John Paul Giannini Jr, Doctor of Philosophy,  
2019

Dissertation directed by:           Professor Wolfgang Losert  
Department of Physics

This dissertation focuses on novel fluorescence microscopy techniques and the biophysical analysis of cell biology enabled by such techniques. Modern cell biology research benefits greatly from the ability to accurately visualize the inner workings of cells. Fluorescence microscopy is particularly well suited to imaging live cells, as it is gentle enough to avoid damaging cells, provides sufficient spatial resolution to image small cellular features, and targets and visualizes specific cell structures and processes with high contrast. An additional feature that is often desirable in fluorescence microscopy is the ability to image rapidly enough to freeze the motion of dynamic cell processes, yet technical limitations make imaging with both high spatial and temporal resolution challenging. In this thesis I address methods for improving the speed, spatial resolution, and optical sectioning of fluorescence microscopy techniques. I then apply some of these innovations to study actin

structures and dynamics in epithelial cells. Because of its role in driving cellular motion, targeted studies of the actin cytoskeleton using fluorescence microscopy can be used to examine cell migration dynamics. In both *in vivo* and *in vitro* experiments, I use high spatiotemporal resolution fluorescence microscopy techniques to provide insight into the role of the actin cytoskeleton in responding to external structural stimuli.

IMPROVING THE SPEED AND OPTICAL SECTIONING OF  
FLUORESCENCE MICROSCOPY TECHNIQUES FOR BIOPHYSICAL  
ANALYSIS OF SUBCELLULAR PROCESSES

by

John Paul Giannini Jr

Dissertation submitted to the Faculty of the Graduate School of the  
University of Maryland, College Park, in partial fulfillment  
of the requirements for the degree of  
Doctor of Philosophy  
2019

Advisory Committee:

Professor Wolfgang Losert, Chair  
Professor José Feijó, Dean's Representative  
Associate Professor Arpita Upadhyaya  
Assistant Professor Giuliano Scarcelli  
Adjunct Professor Hari Shroff

© Copyright by  
John Paul Giannini Jr  
2019

## Acknowledgements

I would first like to thank my advisor, Dr. Wolfgang Losert. Since he helped me get started at UMD, working with me to design and teach introductory physics labs to biologists, Dr. Losert has continued to provide me with amazing opportunities and help guide me through them. I would especially like to thank him for challenging me to become a biologist and teaching me the value in approaching things from an interdisciplinary perspective. I would also like to thank Dr. Hari Shroff for his incredible mentorship and support. Dr. Shroff has taught me vast amounts about microscopy, but perhaps more importantly about problem solving and communicating effectively, challenging me to become a better scientist. In addition, I am grateful to NIBIB and Dr. Shroff for financial support of my work over the past five years. I am grateful to the other members of my committee, Professor José Feijó, Professor Arpita Upadhyaya, and Professor Giuliano Scarcelli, for their time, consideration, and feedback.

I owe many thanks to Dr. Andrew York for his extensive training in coding and optical design. Dr. York inspired me with his creativity and problem-solving skill, but I am most thankful to him for making long coding or alignment sessions seem like just hanging out with a friend.

I am grateful to the entire Shroff Lab for their help, company, and engaging conversation. Dr. Harshad Vishwasrao taught me the basics of cell culture, answered a ton of questions, and put up with sharing an office with me. I would also like to thank Dr. Jiji Chen, Dr. Min Guo, and Ivan Adolfo Rey Suarez for their help and

advice. I owe a great deal to other friends and collaborators around NIH, including Dr. George Patterson, Dr. Chris Combs, Dr. Robert Fisher, and Dr. Maria Ingaramo.

I would like to thank the entire Losert Lab at UMD. In particular, I am thankful to Dr. Xiaoyu Sun for showing me her exciting nanotopography work and helping me get started. I am also thankful to Matt Hourwitz and Eleni Baker for their help crafting nanopatterned substrates, and to Lenny Campanello for all of his help with data analysis.

My family and friends have been hugely supportive to me throughout my graduate studies (and life), and I owe them a great deal. I am grateful to my parents, Connie and John, for all their support and for calling to check in on me and keep me motivated. I am grateful to my sisters, Jennifer and Julia, for cheering me up and sending me dog videos, but also for being inspiring young scientists and challenging me in a family J Giannini h-index race. I am thankful to all my friends for their amazing support. I am particularly thankful to David Ryder and Victoria Anania for their support and putting up with me while writing this thesis.

# Table of Contents

Acknowledgements.....	ii
Table of Contents.....	iv
List of Figures.....	vi
Chapter 1 Introduction.....	1
Chapter 2 Background.....	4
2.1 The Role of Actin in Cell Structure and Motility.....	4
2.2 Light Microscopy.....	9
2.3 Challenges in Fluorescence Microscopy.....	12
2.4 Subverting the Diffraction Limit.....	17
2.5 Improving the Speed and Optical Sectioning of Fluorescence Microscopy.....	22
Chapter 3 Cellular Actin Structures in Response to Nanotopography.....	27
3.1 Introduction.....	27
3.2 Materials and Methods.....	33
3.2.1 Cell Culture.....	33
3.2.2 Transient Transfection.....	33
3.2.3 Plating Cells onto Substrates.....	34
3.2.4 Drug Treatments.....	34
3.2.5 Live Cell Imaging.....	34
3.2.6 STED Imaging.....	35
3.2.7 Optical Flow Analysis.....	35
3.3 Results.....	37
3.3.1 Actin Structures in U2OS Cells on Nanogrooves.....	37
3.3.2 Fixed Cell STED Image Analysis.....	40
3.3.3 Live Cell Actin Structure and Dynamics.....	44
3.4 Discussion.....	49
Chapter 4 Anticipating, Measuring, and Minimizing MEMS Mirror Scan Error to Improve Laser Scanning Microscopy's Speed and Accuracy.....	53
4.1 Introduction.....	53
4.2 Materials and Methods.....	56
4.2.1 Laser Scanning Test Rig.....	56
4.2.2 Point Scanning Microscope Test Rig.....	58
4.3 Results.....	60
4.3.1 MEMS Mirror Characterization.....	60
4.3.2 Mirror Control Optimization Algorithm.....	62
4.3.3 Point-scanning Microscopy Application.....	68
4.4 Discussion and Conclusions.....	69
Chapter 5 Single-shot Super-resolution Total Internal Reflection Fluorescence Microscopy.....	72
5.1 Introduction.....	72
5.2 Results.....	73
5.3 Discussion.....	81
5.4 Methods.....	83
5.4.1 Instant TIRF-SIM.....	83

5.4.2 Estimating the evanescent field depth.....	85
5.4.3 Diffraction-limited TIRF comparisons .....	86
5.4.4 Comparisons with commercial TIRF-SIM .....	87
5.4.5 Flat Fielding.....	87
5.4.6 Deconvolution.....	87
5.4.7 Bleach Correction .....	88
5.4.8 Delining Data.....	88
5.4.9 Drift Correction.....	89
5.4.10 Image Display .....	89
5.4.11 Tracking.....	90
5.4.12 Bead Samples.....	92
5.4.13 DNA Nanorules .....	92
5.4.14 Fixed Samples.....	92
5.4.15 Live Jourkat T Cells.....	93
5.4.16 Live U2OS Cells .....	94
5.4.17 Membrane Imaging.....	95
5.4.18 Myosin Imaging.....	95
5.4.19 Actin Imaging .....	96
5.4.20 Live INS-1 Cells .....	96
5.4.21 Live SK-MEL Cells.....	97
Chapter 6 Discussion .....	98
Chapter 7 Appendices .....	103
A1.....	103
A1.1 Laser Scanning Test Rig Components List.....	103
A1.2 Point Scanning Microscope Test Rig Components List .....	103
Supplementary Figure 1 .....	104
Supplementary Figure 2.....	104
A2.....	105
Supplementary Figure 1 .....	105
Supplementary Figure 2.....	106
Supplementary Figure 3.....	107
Supplementary Figure 4.....	108
Supplementary Figure 5.....	109
Supplementary Figure 6.....	109
Supplementary Figure 7.....	110
Supplementary Figure 8.....	112
Supplementary Figure 9.....	113
Supplementary Figure 10.....	114
Supplementary Figure 11 .....	115
Supplementary Figure 12.....	116
Supplementary Figure 13.....	117
Supplementary Figure 14.....	119
Supplementary Figure 15.....	120
Bibliography .....	122

## List of Figures

Figure 2.1 Actin protrusions .....	6
Figure 2.2 Diffraction limited imaging .....	16
Figure 2.3 The Moiré effect .....	20
Figure 2.4 TIRF microscopy .....	23
Figure 3.1 Actin structures in live cells .....	39
Figure 3.2 3D Super-resolution imaging of actin structures in fixed cells .....	41
Figure 3.3 Actin structure shape characterization.....	42
Figure 3.4 Curvature in actin structures.....	43
Figure 3.5 2D Actin structures and dynamics in live cells .....	45
Figure 3.6 2D Timelapse imaging of actin structures in live cells .....	46
Figure 3.7 3D Actin dynamics in live cells.....	47
Figure 3.8 Effects of latrunculin on actin structures in live cells .....	49
Figure 4.1 Laser scanning test rig .....	57
Figure 4.2 Point scanning microscope test rig .....	59
Figure 4.3 Naïve input voltages become inaccurate for high-speed MEMS operation .....	61
Figure 4.4 Landweber-based deconvolution optimization.....	63
Figure 4.5 Using linear deconvolution to determine input voltage improves scan accuracy compared to naïve voltages .....	65
Figure 4.6 Overview of iterative, measurement-based deconvolution method for precise MEMS mirror control.....	66
Figure 4.7 Response of the MEMS mirror after using iterative, measurement-based deconvolution.....	67
Figure 4.8 Optimized illumination scanning improves fluorescence image quality ..	69
Figure 5.1 Resolution enhancement via instant TIRF-SIM .....	75
Figure 5.2 Instant TIRF-SIM enables high speed super-resolution imaging at the plasma membrane over hundreds of time points .....	77
Figure 5.3 Rapid dynamics of Rab11 are resolved at 100 Hz with instant TIRF-SIM. EGFP-Rab11 was transfected into U2OS cells and imaged at 37°C at 100 Hz.....	80
Figure 7.1 Input voltage comparison .....	104
Figure 7.2 Masking the residual in unimportant areas.....	104
Figure 7.3 Instant TIRF- SIM instrument schematic .....	105
Figure 7.4 Comparative (non-TIRF/TIRF) excitation and emission patterns after micro-optics .....	106
Figure 7.5 Estimating evanescent field decay length with silica beads placed in fluorescent dye .....	107
Figure 7.6 Qualitative instant SIM comparisons highlight the effect of TIRF. ....	108
Figure 7.7 Delining instant-TIRF SIM data.....	109
Figure 7.8 Residual intensity variations after delining procedure .....	110
Figure 7.9 Intensity fluctuations in delined EGFP-Rab11 data along the vertical direction are no greater than along the horizontal direction .....	111
Figure 7.10 Representative bead images .....	113
Figure 7.11 Biological resolution standards in instant TIRF-SIM .....	114

Figure 7.12 Instant TIRF-SIM better resolves Ras microdomains than diffraction-limited TIRF.....	115
Figure 7.13 Simulating diffraction-limited TIRF data from instant TIRF-SIM data	116
Figure 7.14 Displacement and mean speed of tracked EGFP-Rab11 particles. ....	117
Figure 7.15 Effect of temporal undersampling and spatial blurring on automated tracking on EGFP-Rab11 particles .....	118
Figure 7.16 Diffractive or motion blur obscures vesicle motion at the plasma membrane.....	119
Figure 7.17 Motion blur in Traditional TIRF-SIM.....	120

## Chapter 1 Introduction

Fluorescence microscopy is an important tool for investigating cell biology. Gentle and accurate visualization of the inner working of live cells can help to gain a better understanding of cellular processes. This dissertation will provide an overview of current fluorescence microscopy techniques, highlight remaining limitations, and describe innovations for improving the speed and optical sectioning of existing microscopy techniques. Recent improvements in microscopy have allowed for thorough investigation of small, dynamic cellular processes. In this work, I describe cell biology research and biophysical analysis enabled by modern fluorescence microscopy techniques.

In Chapter 2, I provide necessary background information describing cell migration and fluorescence microscopy. Cell migration is often studied because of its role in cancer invasion and other physiological processes, so understanding the mechanisms involved has important implications for treatment. Actin and the cell cytoskeleton are critical in driving cell motion, as actin filaments form protrusions that push the leading edge of cells forward and actin stress fibers help pull the rest of the cell along. To help motivate further research into the structure and dynamics of actin in cells, I will describe the current understanding of actin mechanics in cells. As it has proven to be a valuable tool in studying mechanics such as these, I will also review the current state of fluorescence microscopy. A surge of development over the past few decades has given rise to a variety of microscopy techniques with high spatial and temporal resolution, allowing for the visualization of fast, nanoscale

dynamics in live cells. While these techniques have proven extremely valuable for cell biology research, limitations remain, which I will describe to help motivate future technique improvements.

In Chapter 3, I utilize different fluorescence microscopy techniques to visualize actin structures and dynamics that form in response to nanoscale substrates. Consistent with established results, I find that cells placed on a surface with a grooved pattern, or alternating cliffs and valleys, elongate and align preferentially along the axis of the grooves. In addition, I find that actin structures form in the valleys of the grooves, with a patterning along the axis of the grooves. Using super-resolution microscopy techniques such as instant structure illumination microscopy (iSIM) and stimulated emission depletion (STED), I investigate the nanoscale structure of actin in fixed cells and the dynamics of actin structures in live cells. I then deploy different analytical methods, including a custom 3D optical flow technique, to help characterize the behavior of actin in these cells.

Existing fluorescence microscopy techniques are extremely useful for many cell biology research applications, but because of different imaging constraints, current techniques often involve compromises. Imaging at high spatial resolution, important for investigating small nanoscale cellular structures, often requires sacrificing imaging speed, compatibility with live cell imaging, or optical sectioning. In addition to these inherent tradeoffs, there are also hardware constraints that apply limits to imaging speed. In this work, I address one such hardware constraint, and in Chapter 4, I describe a method for improving control of MEMS mirrors for laser beam steering applications. The accurate, high speed scanning enabled by this method

can be applied to point-scanning or line-scanning fluorescence microscopy methods to improve imaging speed without compromising spatial resolution.

Total internal reflection fluorescence (TIRF) microscopy facilitates excellent optical sectioning, enabling imaging near the base of cells with much higher contrast than other methods. Most existing TIRF techniques either sacrifice spatial resolution to image with high temporal resolution, or vice versa. In order to improve the optical sectioning capabilities of an existing super-resolution fluorescence microscope, I designed and built a beam path to enable TIRF imaging. This technique, instant TIRF SIM, which combines the superior spatiotemporal resolution of iSIM with the optical sectioning of TIRF microscopy, is described in Chapter 5. This enables visualization of biological processes near the base of cells that were not previously observed, which is also described in Chapter 5.

The analysis of actin structures in Chapter 3 yields many additional questions and avenues of investigation, and these will be discussed in Chapter 6. Additional applications of the control algorithm in Chapter 4, including other microscopy techniques, will also be discussed.

## Chapter 2 Background

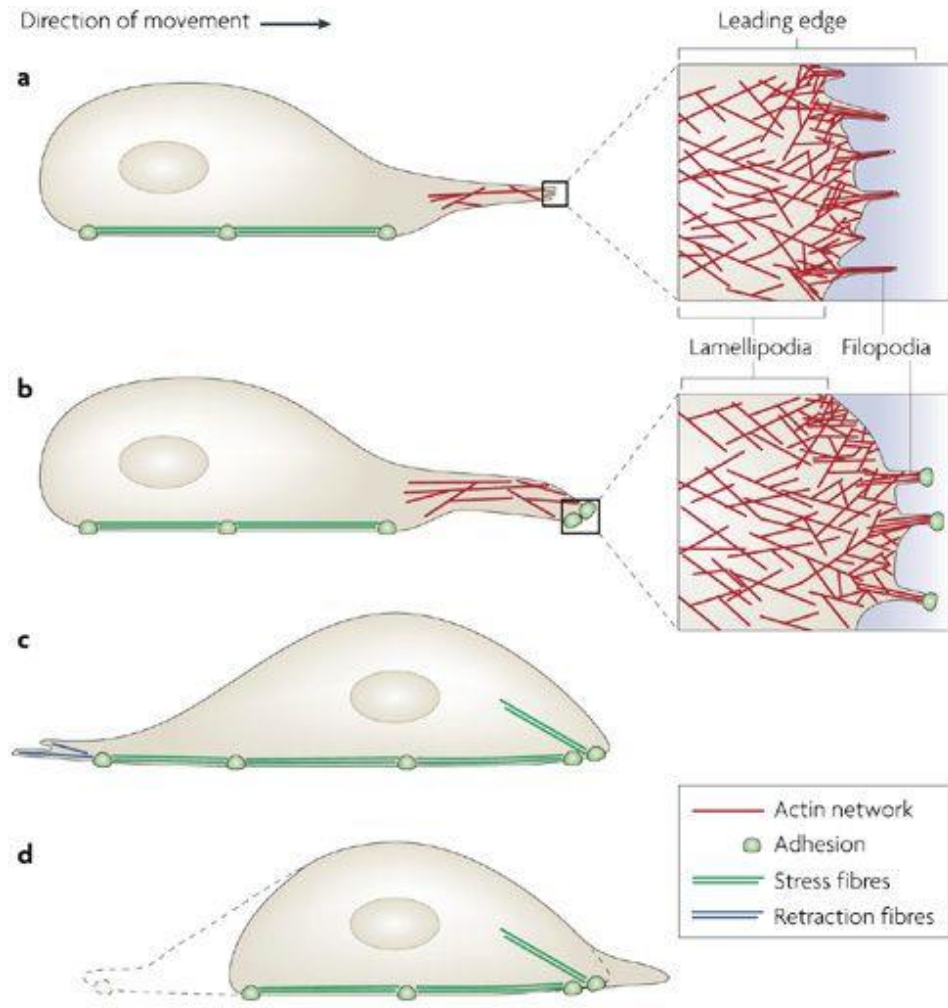
### 2.1 The Role of Actin in Cell Structure and Motility

Cell migration plays an important role in physiology. Cancer invasion and metastasis, embryonic morphogenesis, and wound healing are all driven by collective movement of groups of cells. In developing embryos, groups of cells migrate collectively to different target locations where they differentiate to form complex organs [1]. To heal wounds, many different cell types must respond in a coordinated fashion to a variety of cues. For example, neutrophils, monocytes, and epidermal cells respond to many different of chemotactic and mechanical cues to clot, protect, and regenerate damaged skin [2], [3]. One of the largest causes of death for cancer patients stems from the ability of some cancer cells to break away from the primary tumor, spread through the blood stream, and form new tumors elsewhere. Whether a cancer cell becomes invasive depends heavily on its interactions with its structural and chemical surroundings. Therefore, studying cell motility in response to structural and chemical cues is vitally important for developing treatments to stop the spread of metastatic cancers [4].

Actin, a protein found in a wide variety of cell types, helps form the scaffolding that determines cell shape, as well as driving cell motility and cell division. The actin protein can be found in cells as a free monomer, known as globular (G)-actin, and it also polymerizes into filamentous chains to form F-actin. F-Actin filaments are found in stress fibers supporting the cell body, drive the leading edge in migrating cells, and are contained within a network throughout the body of cells [5]. Myosin, one of many molecular motors that converts chemical energy into

mechanical energy, is responsible for generating contractive forces in cells. Actin and myosin work in close conjunction to drive a variety of types of cell motion [6].

Motile cells harness actin polymerization to form actin-based protrusions, producing physical force and driving motion. The leading edge of migrating cells, termed the lamellipodia (shown in Figure 2.1 a and b), is given structure by branched networks of actin filaments. By forming parallel bundles, actin also helps form spiked protrusions that extend beyond the leading edge of cells, called filopodia [7]–[9] (also shown in Figure 2.1 a and b). Specifically, it has been suggested that filopodia contain helical actin structures, and that the rotation and buckling of these helices (and the resulting contraction of the actin filaments) helps to generate traction that cells use for motility [10]. When moving through a densely packed environment, or extracellular matrix (ECM), some cells use similar actin structures to invade the surrounding area. Proteins that regulate the formation of these protrusions, termed invadopodia and podosomes, are upregulated in some invasive cancer cells [11]. In addition to these structures at the driving edge, actin-myosin stress fibers in cells are also responsible for contracting and pulling the rear end of cells along. These stress fibers, shown throughout Figure 2.1, also provide structure for adhesions points connecting the cell to the surrounding environment.



Nature Reviews | Molecular Cell Biology

Figure 2.1 Actin protrusions

Figure 2.1: Different actin structures in a cell are shown to illustrate their respective roles facilitating cell motility. a) and b) depict the actin structures formed at the leading edge in moving cells, lamellipodia and filopodia. c) and d) show the linking between focal adhesions and actin-myosin stress fibers, along with the contraction force these fibers generate to pull the trailing edge of the cell along. From P. K. Mattila and P. Lappalainen, "Filopodia: molecular architecture and cellular functions," *Nat. Rev. Mol. Cell Biol.*, vol. 9, no. 6, pp. 446–454, Jun. 2008 [9]. Reprinted with permission from Springer Nature.

There are many proteins that are critical in activating and directing actin polymerization, and therefore cell motility. The Arp 2/3 complex binds to existing filaments of actin, initiating the formation of a new branch of actin at a 70 degree angle

with respect to the original filament. The WASP/WAVE family of proteins interact with both existing actin filaments and Arp 2/3 to help localize and activate branching. This branching process helps form the actin structure for lamellipodia in many cells [12]. The Rho family of proteins has also been shown to control and regulate actin protrusions. Rho regulates the formation of both stress fibers and focal adhesions. Actin protrusions in lamellipodia and filopodia are regulated by Rac and Cdc42 [13].

For cells to migrate in one direction, they must have a certain polarity, or difference in structure and/or chemical environment that determines a front and a back. Based on the subunits that form actin filaments, there is a molecular polarity and preferred direction of growth. Free actin subunits preferentially polymerize at the barbed or plus (+) end of filaments, and the other slower-growing end is termed the pointed or minus (-) end [12]. Cells harness this directionality to help drive motion. An effect known as actin treadmilling, where actin subunits depolymerize from the pointed end and polymerize at the barbed end, is thought to help support filopodial protrusions [12]. Chemical conditions, such the localization of proteins Rac and Cdc42, as well as the phospholipid PIP3, towards the leading edge of migrating cells, also plays a role in maintaining polarity [1]. Cell polarity and motility can be studied both in terms of single cell movements, and the patterns and mechanisms for groups of cells [1]. When moving in a group, cells remain connected with neighbors and share some organizational structure [14].

Because of the way they move inside of cells, many pathogens, including *Listeria monocytogenes*, are often used to model the role of actin in cell motility. Once inside the host cells, these pathogens induce the polymerization of actin around them,

and they use these polymerizing actin structures to propel themselves around the cell [15]. In particular, *Listeria monocytogenes* induce the formation of spiral-like actin structures. During this process, the bacteria rotates along its long axis, much like a drill, suggesting there is a twisting force generated by these actin filaments [16]. Some viruses, such as vaccinia virus, have also been shown to utilize a similar actin-based movement mechanism [17]. These pathogens provide insight into the mechanistic role of actin in cell motility, but motility of cells *In vivo* is made more complex by a wide range of structural and chemical factors.

Cells utilize a variety of chemical and structural cues to inform cell motion and other processes. *In vivo*, cells are surrounded by a network of fibers and other macromolecules that provide structural support. This larger-scale extracellular matrix (ECM) also contains many small nanoscale structures that may also provide signals to nearby cells. Cells interact with the surrounding environment through various protrusions and contact points known as focal adhesions. Filopodia, which are supported by parallel bundles of actin, have a role in sensing the cell environment and transmitting signals [18]. It has been suggested that filopodia can detect the stiffness of nearby surfaces by contacting and generating traction forces against them [19]. Substrates with nanofabricated structure can be used to mimic the response of cells to these structures *in vitro* [20]. For example, in response to parallel rows of nanoscale ridges and valleys, multiple cell types have been shown to elongate and migrate preferentially along the axis of the ridges [21]–[23]. Because of its role in cell structure and movement, actin plays an important role in cells interacting with their environment and is often a target for visualization in cellular imaging.

Actin plays a role in many fast-moving processes related to cell migration [11]. Many cell types, such as fibroblasts, keratocytes, and neutrophils migrate *in vivo* at relatively fast speeds of 1-10  $\mu\text{m}/\text{min}$  [24]. Actin structures within migrating cells also dynamically rearrange and change within the cell. Interesting processes related to cell motility, such as actin waves that propagate at  $\sim 6 \mu\text{m}/\text{min}$  [25] occur even in more slowly migrating cells. Thus, to visualize actin dynamics in live cells, biologist utilize a variety of imaging techniques with high-speed acquisition capabilities. While actin forms large-scale cellular structures, individual nanometer-scale subunits also form much smaller structures as well. This necessitates the use of imaging techniques with high spatial resolution to resolve features on the scale of tens or hundreds of nanometers. In Chapter 3, such microscopy techniques will be used to examine actin structures and dynamics that form in response to nanoscale substrates. Light microscopy, in particular fluorescence microscopy, can provide many of the features necessary for imaging small-scale dynamic processes in live cells, and these techniques will be discussed for the remainder of Chapter 2.

## 2.2 Light Microscopy

Light microscopes, from the simple bright field microscope found in many classrooms to those used in cutting-edge biomedical research, are among the most well-known and widely used instruments for performing cell biology research. Light microscopy is particularly useful for biological research because the imaging resolution is on the same spatial scale as many cellular structures and processes, and the light intensities are gentle enough for live cell imaging [26]. Label-free light microscopy techniques, such as brightfield microscopy [27], darkfield microscopy

[28], phase contrast microscopy [29], and Differential Interference Contrast (DIC) microscopy [30] use light absorbed, scattered, and interfered by the sample to create an image. The wavelengths and intensities of light involved with these techniques are gentle enough to image live samples, but the techniques are limited in spatial resolution, contrast, and specificity. Other microscopy techniques enable higher spatial resolution but are not compatible with imaging live cells. For example, electron microscopy enables spatial resolutions down to 5 nm or less [31], but requires chemical or cryo-fixation processes to immobilize and maintain cellular structures, and imaging in a high vacuum [32].

Fluorescence microscopy techniques have enabled cell biologists to image individual proteins inside living cells due the unique combination of gentleness, improved spatial resolution, and specificity they provide [26]. Widefield fluorescence microscopy, one of the most commonly used fluorescence microscopy techniques, uses an objective lens to introduce widefield illumination and collects the resulting fluorescence emitted by the sample onto a camera. The choice of objective lens is important; the focal length of the objective will determine the magnification of the sample to the camera, and the numerical aperture (NA) of the objective will determine the range of angles from which the objective can collect light, which effects signal-to-noise levels and spatial resolution. In widefield microscopy, the objective lens delivers excitation light throughout the entire height of the sample, but only images one focal plane in this region to the camera. Because the camera collects substantial out-of-focus fluorescence in densely labeled samples, this background can obscure useful in-focus information.

Confocal fluorescence microscopy, a popular technique that attempts to solve this issue, uses an illumination beam brought to a point focus in the sample [33]. Because the sample is imaged point-by-point, scanning mirrors are used to raster illumination light throughout the sample, and a point detector such as a photomultiplier tube is used to collect fluorescence. Fluorescence from the sample is focused through a pinhole, which blocks out-of-focus emission from reaching the detector. The spinning disk confocal microscope, a popular instrument in cell biology labs, parallelizes illumination and confocal detection (with multiple illumination foci each matched to a corresponding pinhole), thereby imaging multiple points in the sample simultaneously and greatly improving acquisition speed relative to a traditional confocal microscope.

Fluorescence microscopes rely on a variety of antibodies, dyes, and proteins that fluoresce, absorbing certain wavelengths of light and emitting longer ones. When molecules and atoms in the fluorescent substances absorb incoming light, their electrons are excited to a higher energy state. Fluorescence occurs when an electron relaxes from an excited state to its ground state, emitting a photon with a wavelength characteristic to the energy transition. Various techniques exist to localize (or 'tag') fluorescent molecules to certain objects of interest in cell biology. By filtering the excitation light prior to fluorescence collection, it is then possible to specifically image those tagged biological objects [34]. One of the first fluorescent probes was DAPI, which binds strongly to DNA, absorbing UV light and emitting predominantly blue light [35]. More recently, green fluorescent protein (GFP), originally found in jellyfish, has been developed into an incredibly versatile fluorescent tagging tool [36].

GFP is particularly useful as a fluorescent probe because it gives the ability to tag proteins genetically and is less harmful to living cells than other probes. The work discovering, characterizing, and first utilizing GFP as a fluorescent genetic tag resulted in the award of the 2008 Nobel Prize in Chemistry [37]. The ability to attach fluorophores to specific molecules genetically enabled biologists to detect specific cellular components and make quantitative measurements of their behavior. For example, there are a variety of stains for visualizing F-actin in cells. One such stain, Lifeact, is particularly useful for visualizing the structure and dynamics of actin in live cells, as it was designed to limit interference with cell physiology [38]. Phalloidin, a toxin derived from mushrooms, has a very high affinity for filamentous actin and is thus useful for selectively targeting fluorophores to actin, but is also toxic to live cells [39].

### 2.3 Challenges in Fluorescence Microscopy

While enabling for many *in vivo* cell biology applications, fluorescence microscopy has several limitations. First, every fluorescence microscopy technique is heavily dependent on the specific fluorophores used [40]. Fluorescent probes have distinct sizes, absorption and emission wavelengths, absorption coefficients, quantum efficiencies, and many other properties that impact imaging. An initial challenge is in sample preparation, as fluorescent probes must be introduced to the cells without disrupting cellular structure or function. For fixed-cell experiments, there are straightforward techniques to introduce antibody stains and dyes to label cells [41]. It can be more challenging to introduce foreign objects to live cells without affecting

cell health, but reproducible and effective techniques such as lipofection [42] and electroporation [43] have been developed.

There are additional challenges once the fluorophores are inside the cell. In live cells, fluorophores would ideally function indefinitely without disrupting the dynamics of the protein or cellular structure to which they are localized or becoming toxic to the cell, but this is often not the case. With repeated exposure to excitation light, fluorescent molecules can be chemically altered and lose their ability to fluoresce, a process known as photobleaching. While photobleaching can be useful for certain microscopy techniques [44], in general the resulting loss of fluorescence signal degrades imaging contrast. The levels of excitation light necessary to induce measurable fluorescence can often be damaging, leading to a delicate balance between collecting enough fluorescence for good image contrast and keeping cells alive. Exposure to prolonged excitation light can lead to the creation of chemically reactive free radicals such as singlet and triplet oxygen, which are damaging to cell function [45]. It is therefore important to be economical with excitation light and fluorophore emission cycles, as the total number of photons that can be collected from each fluorophore before photobleaching or photodamage is limited.

Another set of imaging challenges stem from the limitations in spatial and temporal resolution that arise in fluorescence microscopy. To provide insight into dynamic cellular processes, these microscopes must be capable of imaging at rates fast enough to freeze the motion of the process. Temporal resolution is limited both by the hardware of each individual instrument, and more fundamentally by the fluorescence emission rate from the sample. Instruments must be able to deliver the

excitation light to the sample quickly and efficiently, and collect and record the resulting data. Both efficient illumination delivery and collection geometry can limit imaging speed. The fluorophores in the sample must be plentiful enough and imaged over enough excitation/emission cycles to provide enough signal to collect an image with contrast. Gathering enough signal from fluorophores while also using minimum excitation light levels can limit imaging speed [46]. These imaging speed limitations provide significant barriers to the biology that can be studied using fluorescence microscopes. Depending on the technique involved, image acquisition rates can range from milliseconds to minutes [47]. Imaging molecular motor proteins like myosin, kinesin, or dynein, which move  $\sim$ microns/second [48], requires rates  $\sim$ 100 Hz. To measure the propagation of calcium waves, which move  $\sim$ 10-30 microns/second, imaging rates an order of magnitude faster are required [49].

In addition to phototoxicity and temporal resolution, many imaging techniques are limited by their ability to resolve fine nanoscale detail in samples. As described by Ernest Abbe in 1873 [50], the diffractive nature of light fundamentally limits the spatial resolution of optical microscopes. Light from individual fluorophores, which can be approximated by point source objects, will be observed as blurred spots with a minimum size determined by diffraction, shown in Figure 2.2 A. For visible light microscopy, this limits spatial resolution to 200-300 nanometers, a length scale far larger than minute cellular structures. Collecting light with one objective lens, as with most optical microscopes, further limits resolving ability along the optic axis. Because of this, axial resolution is at least 2-3 times worse than lateral resolution [51]. Many cellular structures are completely obscured at these resolutions, as two

proximal small features will be viewed as blurred together, shown in Figure 2.2A. For example, actin, which is an important part of the cytoskeleton of eukaryotic cells, forms structures that are 10s of microns long, but individual actin monomers are <10 nm in diameter [5]. Therefore, while large-scale actin structures can be imaged easily, observing fine detail, such as polymerizing actin filaments, requires finer resolution. Figure 2.2B shows the scale of many biological structures when compared to the diffraction limit for imaging. In general, the ability to observe how sub-diffractive individual proteins interact to form larger scale structures is critical for the further study of structural biology.

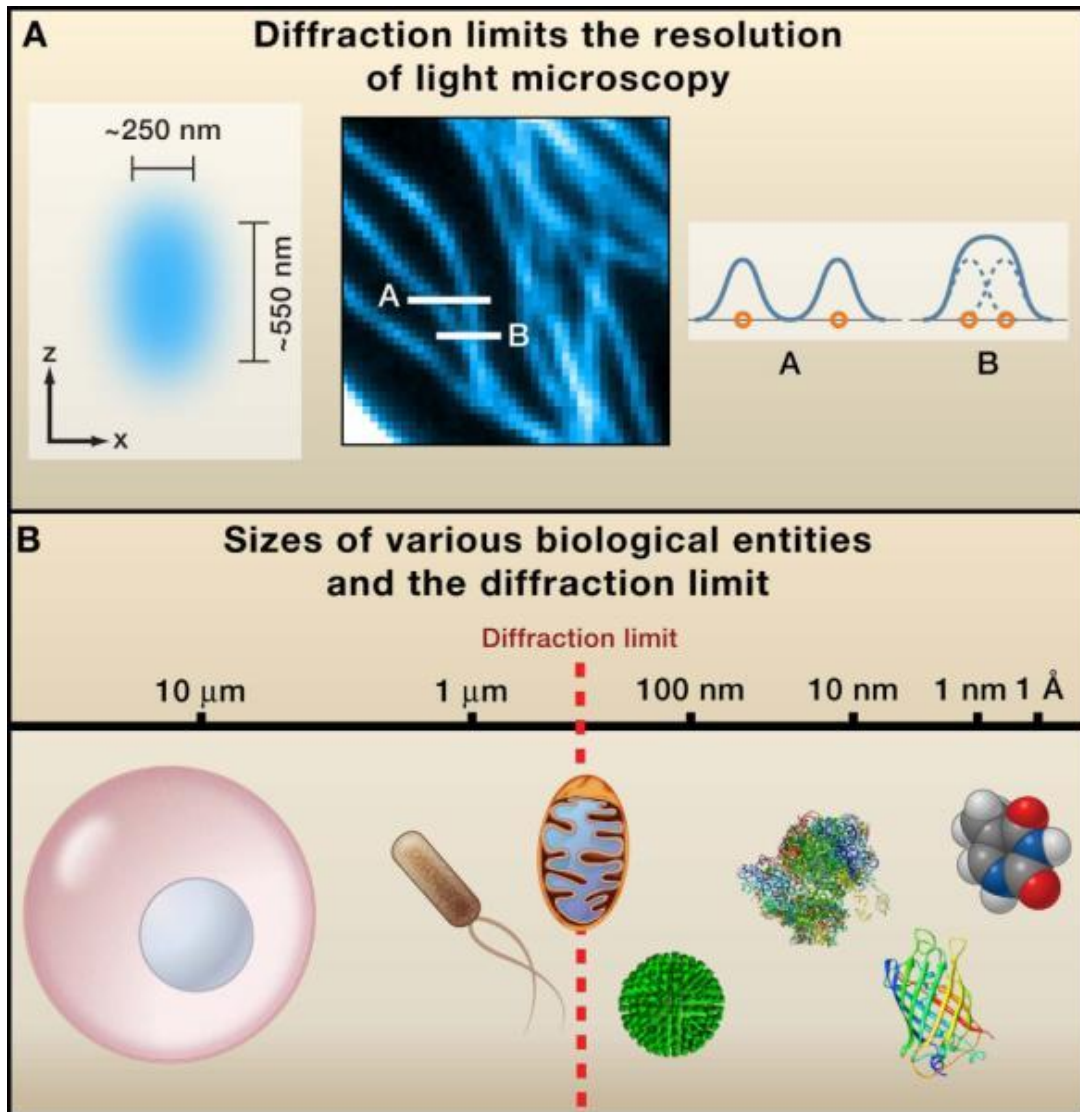


Figure 2.2 Diffraction limited imaging

Figure 2.2: Diffraction-Limited Resolution of Conventional Light Microscopy. A) shows shape of point source when viewed through a diffraction limited imaging system. It also shows the limitations of diffraction limited imaging, as two proximal small features are viewed as blurred together. B) shows the scale of biological structures compared to the diffraction limit. (Left to right) A mammalian cell, a bacterial cell, a mitochondrion, an influenza virus, a ribosome, GFP, and thymine. From B. Huang, H. Babcock, and X. Zhuang, “Breaking the Diffraction Barrier: Super-Resolution Imaging of Cells,” *Cell*, vol. 143, no. 7, pp. 1047–1058, Dec. 2010 [52]. Reprinted with permission from Elsevier.

## 2.4 Subverting the Diffraction Limit

Optical microscopy is only limited by diffraction when techniques require the light to travel distances much larger than its wavelength. Many of the first techniques to subvert the diffraction limit avoid this idea by placing a nanoscale mechanical probe very near the sample. This idea, which gave rise to so-called near field microscopy techniques, was first suggested in the 1920s by EH Synge [53], and was later demonstrated in 1972 by Ash and Nicholls [54]. These techniques can achieve sub-diffractive spatial resolution, achieving resolutions of 50-150 nm [54], [55], but because of the probe constraints (must be physically close to observation target) are limited to surface-level observation, which limits biological applications. To look farther into cells, techniques were required that operate farther away, or in the far-field. While one of the first demonstrations of far-field super-resolution occurred in 1966 [57], the field has primarily developed in the last 30 years.

More recently, a variety of far-field fluorescence microscopy techniques have been developed for subverting the Abbe diffraction limit and achieving finer spatial resolution. Some of the theoretical framework for breaking the diffraction limit with structured illumination was established by C.J.R. Sheppard in 1988 [58]. Sheppard described a method of pixel reassignment that would enable a factor of two resolution improvement for confocal microscopy, but his theory would not be experimentally verified until a decade later. The first modern far-field fluorescence technique developed to break the diffraction limit was stimulated emission depletion (STED) microscopy [59] in 1994 by Hell and Wichmann. In 1999, Heintzmann and Cremer experimentally demonstrated the use of structured illumination for fluorescence

microscopy with improved resolution [60]. In the twenty years since this field was pioneered, there has been an explosion of innovation. In fact, the 2014 Nobel Prize in Chemistry was awarded to Stefan Hell, William Moerner, and Eric Betzig for their work developing super-resolution techniques [61].

In general, three strategies are used to achieve sub-diffractive resolution, each with their respective strengths and weaknesses. STED microscopy [59] uses a diffraction-limited excitation beam along with donut-shaped depletion beam to confine fluorescence to a smaller region. While the depletion beam is still limited in size by diffraction, STED techniques use high depletion beam intensities to saturate the fluorophores in the donut region. With sufficiently high depletion beam intensities, the region of emitting fluorophores remaining is subdiffractive, and allows for super-resolution imaging. Because of the laser intensities involved, this technique can be damaging to live samples, and because it is a point scanning technique, large fields of view can be time-consuming to acquire. Both STED and a larger group of techniques known as reversible saturable optical linear fluorescence transitions (RESOLFT) [62] use fine control of the volume of fluorophores being excited to improve resolution, typically in the range of 20-100 nm [47]. Localization approaches, such as photoactivation localization microscopy (PALM) [63] and stochastic optical reconstruction microscopy (STORM) [64], uses the process of reconstructing images from many frames containing diffraction-limited images of sparse, isolated emitters to break the diffraction limit. PALM and STORM techniques enable spatial resolution down to 10-20 nanometers, but because they require many frames to compile a complete image, they can be time intensive (~30 sec-minutes per

image) and damaging to the sample [47]. Because of the high levels of laser illumination and longer acquisition times involved, these categories of techniques are not traditionally used for live cell imaging over long durations or to provide volumetric time-lapse (4D) images of living samples.

The third category of techniques are structured illumination microscopy approaches. Because of the limitations of objectives, lenses, and other components, optical microscopes are limited in their ability to transmit fine detail (high spatial frequencies in the Fourier domain). In general, structured illumination techniques use fine structure in their illumination patterns to achieve improved resolution. To do this, structured illumination techniques utilize a phenomenon known as the Moire effect, shown in Figure 2.3, which describes how when two patterns with fine structure are overlaid, the resulting pattern has both fine and coarse structure. In microscopy, when an illumination pattern with fine structure is overlaid with a sample containing fine detail, additional coarse emission light patterns are created that can be transmitted by the microscope. Utilizing knowledge of the illumination pattern, these coarse patterns can be analyzed to infer additional fine detail about the sample.

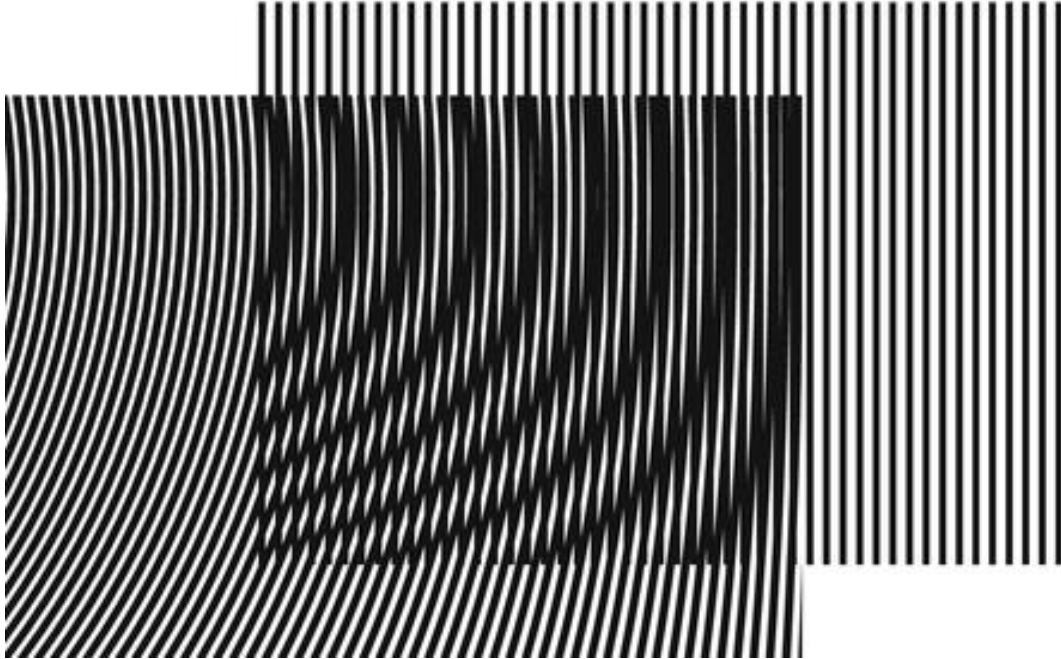


Figure 2.3 The Moiré effect

Figure 2.3: When two patterns with fine structure are overlaid, the resulting pattern has both fine and coarse features. From K. Wicker, “Super-Resolution Fluorescence Microscopy Using Structured Illumination,” in *Super-Resolution Microscopy Techniques in the Neurosciences*, E. F. Fornasiero and S. O. Rizzoli, Eds. Totowa, NJ: Humana Press, 2014, pp. 133–165 [65]. Reprinted with permission from Springer Nature.

In 1999, Heintzmann and Cremer implemented a technique which used a diffraction grating to create a laterally modulated illumination pattern. Soon after, Gustafsson demonstrated an improved implementation of this technique which was the first to experimentally verify the factor of two resolution improvement proposed by Sheppard [66]. These widefield implementations use a sinusoidal illumination pattern which is scanned and rotated with respect to the sample to collect multiple raw images. These raw images are combined computationally to reconstruct a higher resolution final image; using knowledge of each specific illumination pattern,

encoded high spatial-frequency information is shifted to its true location in the frequency domain, allowing for finer resolution.

In addition to these widefield techniques, many point scanning approaches like confocal microscopy were adapted to improve spatial resolution. The first of these techniques was developed in 2010 by Müller and Enderlein [67]. As in confocal microscopy, an illumination point is scanned through the sample, and the corresponding fluorescence pinholed and imaged onto a detector. For point scanning structured illumination approaches, the point detector is replaced with a CCD chip or another array of detectors, which allows information about the entire shape and intensity of the emission to be collected. Each pixel in the detector contains information about the structure of the illumination in the sample shifted slightly from its true position. By shifting this signal back to its correct location, an image with improved signal and resolution can be constructed [68]. This pixel reassignment was first conducted digitally, with extensive postprocessing.

Like confocal imaging, this technique could be improved with the parallelization of illuminating and collecting multiple points simultaneously, an advance made by York and Shroff in 2012 with the development of the multifocal structured illumination microscope (MSIM) [69]. This technique was further improved with the realization that pixel reassignment could be done optically instead of computationally. York and Shroff developed the instant structured illumination microscope (iSIM) [70], which uses arrays of microlenses to create an array of illumination point foci in the sample and then to scale and shift the resulting fluorescence emission. Similarly, Manders and De Luca developed re-scan confocal

microscopy (RCM) [71], another technique for all-optical pixel reassignment. This technique uses decoupled scan and rescan mirrors to alter the magnification of the object with respect to the magnification of the scanning spot.

## 2.5 Improving the Speed and Optical Sectioning of Fluorescence Microscopy

Many other techniques have been developed to improve the speed, gentleness, and optical sectioning of fluorescence microscopy. Developed in the 1980s, total internal reflection fluorescence (TIRF) [72] microscopy is a technique particularly useful for imaging structures and processes that occur very close to the cell-coverslip boundary. TIRF microscopy relies upon a property of light at a boundary between higher and lower refractive index media, which is that if light hits the boundary at an angle larger than a certain critical angle, it will be completely reflected and will not pass the boundary. The critical angle depends on the refractive indices of the two media. In Figure 4, this boundary between water and glass is shown, and the critical angle,  $\alpha$ , of the illumination light is shown. This property is useful for microscopy because when laser illumination is totally internally reflected at the cell coverslip-aqueous medium boundary, it creates an evanescent light field that extends only a few hundred nanometers into the sample. TIRF illumination is useful in cell biology as it allows for very selective excitation of fluorophores near the base of the cell [72]. In Figure 4, the evanescent field is shown selectively illuminating vesicles and microtubules close to the media boundary. More recently, TIRF microscopy has been combined with principles of structured illumination microscopy to allow for super-resolution imaging with excellent optical sectioning [73], [74]. These techniques are

limited to imaging speeds  $< 11\text{Hz}$ , as they sacrifice some temporal resolution for spatial resolution. Some dynamic processes near the cell-coverslip boundary require faster imaging to properly visualize, and more technique development is required. This will be discussed further in Chapter 5.

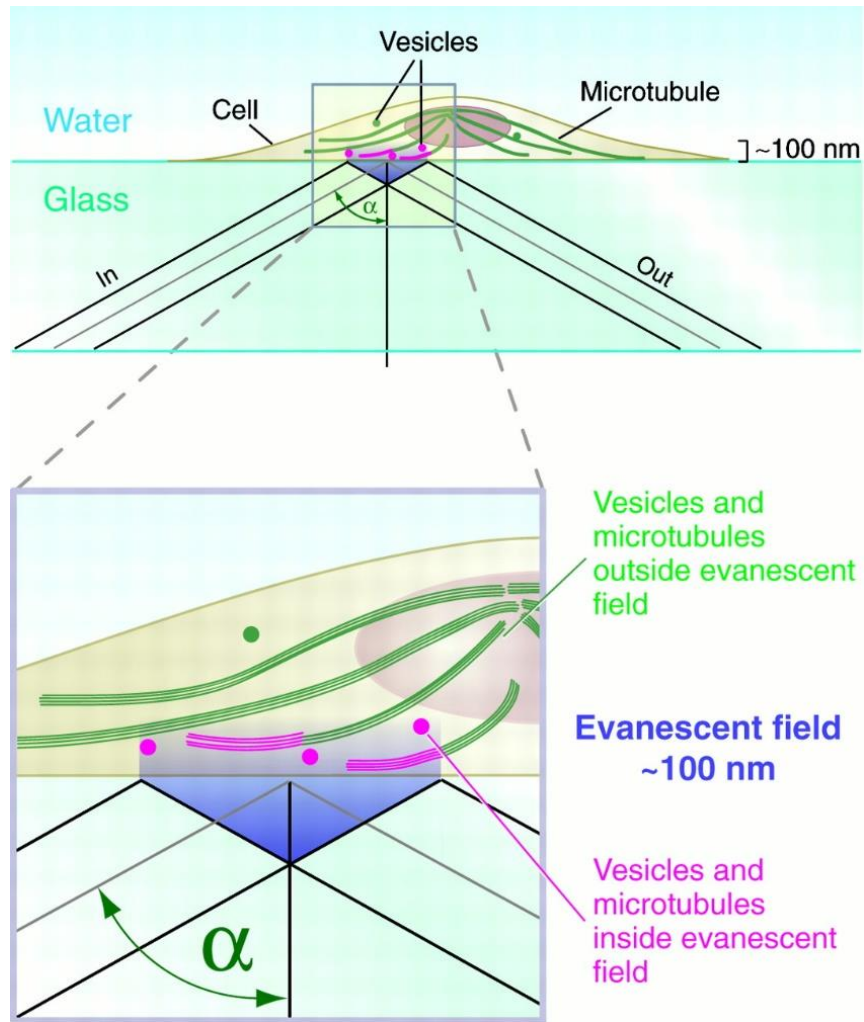


Figure 2.4 TIRF microscopy

Figure 2.4: When illumination light approaches a water/glass boundary edge from a sufficiently high angle,  $\alpha$ , an evanescent field is created at the boundary. This field, which only extends approximately 100 nm, can be utilized to selectively image features close to the boundary. From D. J. Stephens and V. J. Allan, “Light Microscopy Techniques for Live Cell Imaging,” *Science*, vol. 300, no. 5616, pp. 82–86, Apr. 2003 [75]. Reprinted with permission from AAAS.

Another approach that minimizes out-of-focus fluorescence is light sheet microscopy, also known as selective plane illumination microscopy (SPIM) [76]. This technique involves using a set of two orthogonal objectives to illuminate and observe the sample. One objective creates a light sheet of illumination in the sample, and the other is oriented so that its focal plane is along that same sheet, as to detect the resulting fluorescence. Because only one cross-section of the sample is illuminated at a time, this technique has two major benefits. First, because the illumination light sheet only excites fluorophores in the plane being observed by the observation objective, there is little out-of-focus fluorescence generated. Secondly, the overall laser illumination dose to the sample is greatly reduced, so the effects of photobleaching and photodamage are minimized.

One important technical feature of light sheet microscopes is the mechanism for creating the light sheet illumination. Some light sheet devices use a cylindrical lens to create a static light sheet, illuminating the entire imaging plane at once. Because no laser beam scanning is required, this method allows for very fast imaging rates (hundreds of Hz) [77]. This method is generally limited in terms of spatial resolution to that of a widefield microscope laterally, and axially by the product of light sheet thickness and detection objective axial resolution. Another method for generating a light sheet is to scan a low numerical aperture laser beam quickly across the imaging plane. This procedure allows for increased control over the dimensions, intensity, and other properties of the light sheet illumination, but the beam scanning speed can limit imaging rates. When coupling the line illumination with a confocal

slit it is possible to provide slightly improved contrast compared to a static light sheet [78].

One of the limiting factors in SPIM, confocal microscopy, and other laser scanning microscopy techniques is beam scanning speed. Multiple devices are utilized to perform fast laser beaming scanning, each with associated positive and negative attributes [79]. For example, many beam scanning applications utilized galvanometer-controlled mirrors, but these are best suited for slower step-stop motion or fast resonant scanning, and laser scanning microscopy techniques often require fast customizable scan patterns. One of the primary disadvantages of galvanometer-controlled mirrors is the inertia involved with accelerating the mass of the mirror. Raster scanning for confocal microscopes is often performed with resonant galvanometers, including in many commercial systems [75].

Rotating polygonal mirrors provide constant speed, one dimensional scanning without the inertial disadvantages of galvanometers. While they have proven useful for some optical microscopy applications [80], the axial path length varies during each scan, which requires optical correction. Acousto-optic deflectors (AOD), which use a tunable diffraction grating to control laser beam output angle, are also used for fast laser scanning. The absence of moving mechanical parts allows AODs to scan at very rapid speeds, which has proven useful for microscopy applications [81]. These devices are limited to a small scan range ( $<4$  degrees) and are highly dispersive, which limits their usefulness for rescan microscopy applications.

Microelectromechanical systems (MEMS) scanners have the technical capabilities to enable accurate high-speed scanning: they are available in a range of

sizes (~0.5-5 mm), can access moderate angles ( $> \pm 10$  degrees optical), can scan at high speeds (300 Hz to 6 kHz line rates), and have the capability to scan in two dimensions. Because of their mechanical workings and mirror sizes, MEMS mirrors suffer slightly less from the inertia problems of galvanometer-controlled mirrors. MEMS scanners have proven useful in a variety of applications, including many in fluorescence microscopy [82], [83]. One of the main issues with MEMS scanning at high speeds is hardware control, as mirror response to fast scanning signals often deviates from the desired scan pattern. Control methods for MEMS scanners will be discussed further in Chapter 4.

In Chapter 3, advanced microscopy techniques will be used to enable examination of fine actin structures that would be obscured by lower-resolution techniques. In Chapter 4 and 5, technical improvements to microscopy techniques to improve imaging speed and optical sectioning will be discussed.

## Chapter 3 Cellular Actin Structures in Response to Nanotopography

Xiaoyu Sun performed many of the preliminary experiments motivating this work. Eleni Baker, Matt Hourwitz and Xiaoyu Sun prepared the nanotopography surfaces. Leonard Campanello wrote 2D optical flow analysis code. John Giannini designed experiments, imaged cells, and analyzed data.

### 3.1 Introduction

Cell motility and collective migration are critical to a variety of important physiological processes. The study of how cells move in response to structural and chemical cues has important implications for cancer invasion and metastasis [4], embryonic morphogenesis [1], and wound healing [2]. In particular, understanding the mechanisms that enable metastatic cancer cells to invade their surroundings could lead to life-saving new treatments. The signaling pathways and cellular mechanisms that drive cell motility are complex, and they occur on a spatial scale that approaches or exceeds the limitations of diffraction-limited imaging. Fibroblasts, keratocytes, and neutrophils move at maximal migration speeds between 1-10  $\mu\text{m}/\text{min}$  [24], and faster moving cells require fast imaging rates to effectively observe. Even in cells that migrate at slower rates, interesting processes related to cell motility occur at similar speeds, such as actin waves that propagate at  $\sim 6 \mu\text{m}/\text{min}$  [25]. Dynamic processes inside cells often move at faster speeds than overall cell migration, requiring a balance of speed and fine spatial resolution to capture. Many advances in the fields of microscopy [70] and biophotonics [38] have made it possible to visualize specific protein dynamics while limiting the disruption of cellular processes. By examining the individual proteins at work, it is possible to gain insight into the cellular processes that control cell motility.

Actin, a protein that helps form the scaffolding in most eukaryotic cells, plays a key role in driving cell motility. Actin is one of the major structural components in cells, and also is present in a variety of protrusions that help cells move. The lamellipodium, which forms the leading edge that drives a cell forward, is primarily composed of actin filaments. Furthermore, spiked protrusions that interact with the surrounding environment, such as filopodia and invadopodia, are formed by bundles of parallel actin filaments [84]. The actin bundles contained in filopodia, which have been observed to have a helical shape, may generate traction for cell motility by rotating, buckling, and changing the length of the protrusions [10]. These protrusions play an important role in exploring the surrounding area and may aid cells in collecting information about the surrounding environment.

The extracellular matrix (ECM), which provides structural support to the cells around it, contains many small, nanoscale structures that may also provide signals to those cells. The process by which cells respond to external structures is known as contact guidance [85]. One proposed mechanism for how cells are guided by contact with external stimuli is known as focal adhesion patterning [21]. This theory suggests that focal adhesions, which are points of interaction between a cell and its surroundings, align differently in response to contact with different structures, and their alignment passes different cues to cells to affect cell shape and motility. Integrins, transmembrane proteins that connect the cell cytoskeleton to the surrounding ECM, are critical in forming focal adhesions. Another theory suggests that filopodia play an important role in sensing the surrounding environment and causing cellular responses [84].

A variety of studies have investigated how cells respond to different topographical cues using many different *in vitro* settings. Nanofabricated substrates allow for controlled investigation into how structures near the base of a cell (and near the focal contacts of the ECM) affect cell motility [20], [22], [23]. Cells placed on a surface with a grooved pattern, or alternating cliffs and valleys, have been shown to elongate and align preferentially along the axis of the grooves. This effect has been shown to be consistent over a variety of cell types and measurable responses have been observed with feature dimensions down to ~100 nm [21]. Some cell types display an ability to sense even smaller features, as fibroblasts grown on grooves with a depth as little as 35 nm (but not finer) were found to align preferentially along the grooves [86]. It has been found that filopodia that protrude from the cell perpendicular from the axis of the grooves retract much more quickly than protrusions along the axis, which may lead to the preferential elongation [14].

In addition to elongation, many cell types also migrate preferentially along grooved patterns. In contrast, the same cell types deposited on flat substrates move more randomly. Many of the motile cells deposited on grooved patterns also move at faster speeds than expected from migration on a flat surface. *Dictyostelium discoideum* were found to elongate and migrate faster and more frequently parallel to nanoridges, and the ridge spacing with the greatest influence on contact guidance was 1.5  $\mu\text{m}$  [22]. Smooth muscle cells showed a preference for migrating along ridges over responding to a wound healing cue and moving towards a wound edge [87]. MCF10A epithelial cells plated on nanoridges and then later fixed also aligned along

nanoridges. F-actin fibers in these cells were observed to have aligned themselves along the ridges before fixation [88].

When considering the intracellular mechanisms of this contact guidance process, we focus on the dynamic actin structures introduced above. Actin polymerization has also been shown to form much more dynamic waves or moving patches in many cell types [89]. These actin waves have been shown to propagate near the cell-substrate border and help generate protrusions when they push up against the cell wall [25]. The exact triggering mechanism for actin waves is still not clear, and possibly arises from random fluctuations, activating adhesions, or membrane tension [90]. In *Dictyostelium* plated on nanoridges, actin waves were shown to propagate preferentially along the ridges, generally within 500 nm of the ridge. These actin waves often fill the grooves between ridges and propagate along the grooves independently of waves in adjacent grooves. Cells migrating perpendicular to ridges still display actin waves parallel to the ridge structure [22]. Substrates with parallel nanoridges have also been used to study actin dynamics in B-cells; in this cell type, B-cell receptors drive modulations in actin dynamics, triggering and amplifying reactions to the surrounding environment [91].

Latrunculin, a drug purified from a Red Sea sponge, associates with actin monomers and prevents them from polymerizing, and can therefore be used to study actin dynamics [92]. When actin is globally depolymerized in *Dictyostelium* cells using latrunculin A, after washing to remove latrunculin, actin filaments reorganize in waves along the bottom surface. These waves are transient, and travel at speeds of  $\sim 10 \mu\text{m}/\text{min}$ . When actin polymerization waves travel near the edge of cells, they can

provide force to push the cell membrane outwards [93]. In addition to Dictyostelium cells, BHK21 fibroblasts and mouse melanoma cells have also been shown to display dynamic actin waves. Actin fiber structures move throughout these cells at speeds of 2-5  $\mu\text{m}/\text{min}$  and can contribute to forming protrusions at the cell membrane [89]. In U2OS human epithelial cells, actin waves near the underside of the cell move at  $1.61 \pm 1.06 \mu\text{m}/\text{min}$  and have been shown to be coupled with integrin-based ECM adhesions [94]. These waves have been well studied in the 2D plane near the cell surface, but because of the imaging challenges of 3D imaging with high spatial-temporal resolution, they were only recently studied thoroughly in 3D. Using advanced microscopy techniques (3D STED, lattice light sheet microscopy (LLSM), and DIC), changes to the actin cytoskeleton of Jurkat T cells in response to cell contact formation were closely examined [95].

The relevant spatial scale for studying cellular response to nanotopography is close to or smaller than the diffraction limit of optical microscopy. For example, collagen, one of the ECM components that is often indirectly modelled with nanofabrication, forms fibers many micrometers in length with a diameter of 260-410 nm [96]. In the ideal case, diffraction-limited optical microscopes can achieve a lateral resolution of  $\sim 250$  nm with 2-3 fold worse axial resolution, so super-resolution microscopy is needed to resolve fine cellular structures below this scale. Multiphoton absorption polymerization (MAP) allows for the creation of customizable acrylic patterns on glass coverslips at the nanoscale necessary to simulate ECM components [97]. These patterns have a similar refractive index to glass, which allows for high resolution optical imaging with limited scattering or refraction. In addition to spatial

resolution constraints, to observe dynamic movement of actin structures, imaging must be both gentle enough for prolonged live cell imaging and fast enough to defeat motion blur. Due to its high spatiotemporal resolution, the instant SIM provides a unique opportunity to resolve the shape and dynamics of small actin structures [70].

After acquiring the data at high spatiotemporal resolution, a variety of methods enable analysis of the resulting data. Visualizations of actin in cells can be processed to isolate and skeletonize actin structures. This data can be used to examine the shape of actin waves [25], [90], as well as the stiffness and other mechanical properties of actin filaments [98]. Valuable information about the size, shape, persistence length, and curvature of collagen [99], [100] and other fibers [101] has also been extracted from microscopy data using a variety of methods. Many of these processing methods can also be applied to actin fibers.

Lifeact, a peptide that stains F-actin structures, can be used to visualize the structure and dynamics of actin while limiting interfering with its physiology [38]. Because it selectively localizes to F-actin, measuring dynamic fluorescence intensity changes in live cells provides information about actin waves. Temporal image sequences can reveal interesting information about cellular processes with proper analytical methods. A variety of methods exist for automated particle tracking [31], but these methods largely presuppose constant well-defined features, such as particle borders. For time-series of images without such features, optical flow analysis can be used to quantify localized motion [103]. Optical flow analysis measures spatial image intensity changes between consecutive image frames to generate a vector flow field describing the motion between frames. Optical flow analysis has proven useful for

analyzing fluorescence signals from live cell time-lapse imaging [104], with the capacity to track fluorescent point sources over distances as small as 160 nm with 3% error [105].

In this work, actin structures formed in cells on nanopatterned substrates will be investigated. Using a STED microscope with 3D super-resolution, the fine structure of actin in fixed cells will be characterized. The structure and dynamics of actin in live cells will be investigated using the fast, gentle, super-resolution imaging capabilities of the iSIM.

## 3.2 Materials and Methods

### 3.2.1 Cell Culture

Human Bone Osteosarcoma Epithelial Cells (U2OS) were cultured in DMEM supplemented with 10% FBS (Life Technologies) in a CO<sub>2</sub> supplied incubator (5%) at 37°C. Cells were passaged at 70–90 % confluency.

### 3.2.2 Transient Transfection

LifeAct Emerald was transfected into U2OS cells using X-tremeGENE HP DNA transfection reagent (Sigma Aldrich). 1 µg DNA was added to 100 µL diluent (Sigma Aldrich HBSS), to which 2.5 µL of transfection reagent was added. The transfection complex was set to incubate at 15-30°C for 15 minutes, and then added to the cell media. Cells were incubated for 24 hours at 37°C before fluorescence measurements.

### 3.2.3 Plating Cells onto Substrates

To create patterned substrates, a master surface is first fabricated using multiphoton absorption polymerization (MAP). The surface consists of grooves 500 nm wide by 1  $\mu\text{m}$  deep, evenly spaced by 1.5  $\mu\text{m}$  (See Figure 3.1a). A PDMS mold is created from the master surface, and from the mold replicates were formed with an acrylic resin on acrylate-functionalized cover glass. Patterned substrate cover slips cleaned in 90% ethanol for at least 4 h and then attached to 25 mm wells using a non-toxic glue (Dow SYLGARD 164 Silicone Encapsulant). Wells were filled with 2 mL DMEM plus 10% FBS and cells were plated directly onto these cover slips.

### 3.2.4 Drug Treatments

Latrunculin A was purchased from Sigma-Aldrich and dissolved in DMSO to a stock of 500  $\mu\text{M}$ . Cells were exposed to 500 nM Latrunculin A and incubated for 4 hours at 37°C before fluorescence imaging measurements.

### 3.2.5 Live Cell Imaging

Fluorescence images were obtained using structured illumination microscopy (iSIM) [70]. Data collection for some experiments was performed at room temperature, and for experiments conducted at 37 °C, the sample was mounted in an incubation chamber (Okolab; H301-MINI). Exposure times for live cell image were approximately 40 ms per frame. Excitation laser wavelength was 488 nm and average laser power before the objective lens was approximately 1-5 mW. 3D data acquisition was performed by taking consecutive images at axial steps of 50 or 100 nm. Presented images represent raw data (i.e. they are not deconvolved).

### 3.2.6 STED Imaging

Fluorescence images were obtained using a Leica SP8 equipped with STED capability. For STED imaging, cells were fixed in 4% paraformaldehyde/PBS for 1 h on patterned substrates. Cells were then washed three times in PBS and permeabilized with 0.5% Triton-X/PBS for 15 min, washed another three times with PBS, and blocked with 1% BSA/PBS for 1 h. Cells were stained with Alexa Fluor 594 Phalloidin in a solution with 1% BSA/PBS. The Leica SP8 used a 100X 1.40 NA oil objective along with a white light laser for excitation light, which was tuned to provide 592 nm excitation and 775 nm depletion. Notch filters for 592 nm and 775 nm light were used to filter excitation and depletion light. Images are an accumulation of 6 line averages/line and 2 frames/image. Image acquisition took approximately ~60 s per frame. Deconvolution was performed with a Leica 3D deconvolution processing wizard using an automatically generated model of the microscope PSF.

### 3.2.7 Optical Flow Analysis

Optical flow analysis was used to calculate optical flow fields for consecutive frames of timelapse imaging. Optical flow analysis algorithms assume all fluctuations in intensity frame-to-frame are due to motion and calculate a series of intensity derivatives to characterize motion between frames. Image features are assumed to be locally constant from frame-to-frame. The Lucas-Kanade method assumes that motion is both small and mostly constant in the neighborhood around the pixel of interest, and then uses a weighted least-squares fit to find the image flow vector for each pixel [106].

Implementations of optical flow analysis attempt to solve the 2D motion constraint equation (Eq. 1) for the x and y components of optical flow,  $\frac{dx}{dt}$  and  $\frac{dy}{dt}$  using image intensity derivative information.

$$\left(\frac{dI}{dx}, \frac{dI}{dy}\right) \cdot \left(\frac{dx}{dt}, \frac{dy}{dt}\right) = -\frac{dI}{dt} \quad (1)$$

Equation 1:  $\frac{dI}{dx}$ ,  $\frac{dI}{dy}$ , and  $\frac{dI}{dt}$  represent image intensity derivatives in terms of x, y, and t, and  $\frac{dx}{dt}$  and  $\frac{dy}{dt}$  represent the x and y components of optical flow at a given pixel.

Because Eq 1 has two unknowns ( $\frac{dx}{dt}$  and  $\frac{dy}{dt}$ ), it is not possible to estimate the optical flow vectors with intensity derivative from just one pixel. By assuming all pixels in a local neighborhood have the same flow vectors, it is possible to employ a series of equations from which the flow vectors can be solved. In effect, a weighting function,  $W(x,y)$  is used to place greater emphasis on pixels closer to the one being analyzed.

$$\sum_{x,y \in \Omega} W^2(x,y) \left[ \left(\frac{dI}{dx}, \frac{dI}{dy}\right)(x,y,t) \cdot \left(\frac{dx}{dt}, \frac{dy}{dt}\right) + \left(\frac{dI}{dt}\right)(x,y,t) \right]^2 \quad (2)$$

Equation 2:  $\frac{dI}{dx}$ ,  $\frac{dI}{dy}$ , and  $\frac{dI}{dt}$  represent image intensity derivatives in terms of x, y, and t, and  $\frac{dx}{dt}$  and  $\frac{dy}{dt}$  represent the x and y components of optical flow at a given pixel.  $\Omega$  represents the small local neighborhood of pixels being considered, and  $W(x,y)$  represents a weighting function which gives more consideration to pixels in the center of the neighborhood.

Minimizing Eq 2 produces a closed form solution for optical flow vectors for 2D calculations. In effect, there is a well-defined solution for the x and y components of optical flow based on matrix calculations involving the spatial and time intensity derivatives  $\frac{dI}{dx}$ ,  $\frac{dI}{dy}$ , and  $\frac{dI}{dt}$ . To ensure that every calculated vector represents actual image flow, the vectors are subjected to a thresholding based on

eigenvalue/eigenvector decomposition of matrices containing spatial intensity derivatives.

### 3.3 Results

#### 3.3.1 Actin Structures in U2OS Cells on Nanogrooves

Due to its high spatiotemporal resolution, the instant SIM provides a unique opportunity to resolve the shape and dynamics of small actin structures within live or fixed cells that are deposited on nanogrooved substrates. With lateral spatial resolution of  $\sim 145$  nm and temporal resolution exceeding 100Hz, the iSIM can capture the rapid movements of small, subdiffractive features [70]. Also, new fluorescent markers, such as LifeAct, now enable the investigation of the role of actin in live cells while limiting interference with the underlying cellular processes [38]. Together, these techniques allow for the examination of actin dynamics in live cells at high speeds.

As described above, nanoscale patterning can be used to examine cellular response to external structures. Grooved patterns 500 nm wide by 1  $\mu$ m deep, spaced by 1.5  $\mu$ m were printed on glass coverslips (Figure 3.1a), with the goal of characterizing of the structure and movement of polymerizing actin in and around the nanogrooves. The imaging of live U2OS cells with transiently transfected LifeAct Emerald allows for a snapshot of the many cellular functions of actin. Figure 3.1b shows f-actin in stress fibers, filopodia, and forming structures along the grooved

substrate. Along the bottom surface of the cell, actin structures mainly form in the valleys of the nanogrooves, and they often have patterning (See Figure 3.1c-f) along the axis of the grooves (y-axis in Figure 3.1a). LifeAct stains filamentous actin (F-Actin), but it is unclear if these structures represent stress fibers, microfilaments, or some other structures. 2D timelapse imaging shows that these actin structures move parallel to the grooves, up and down along the y-axis.

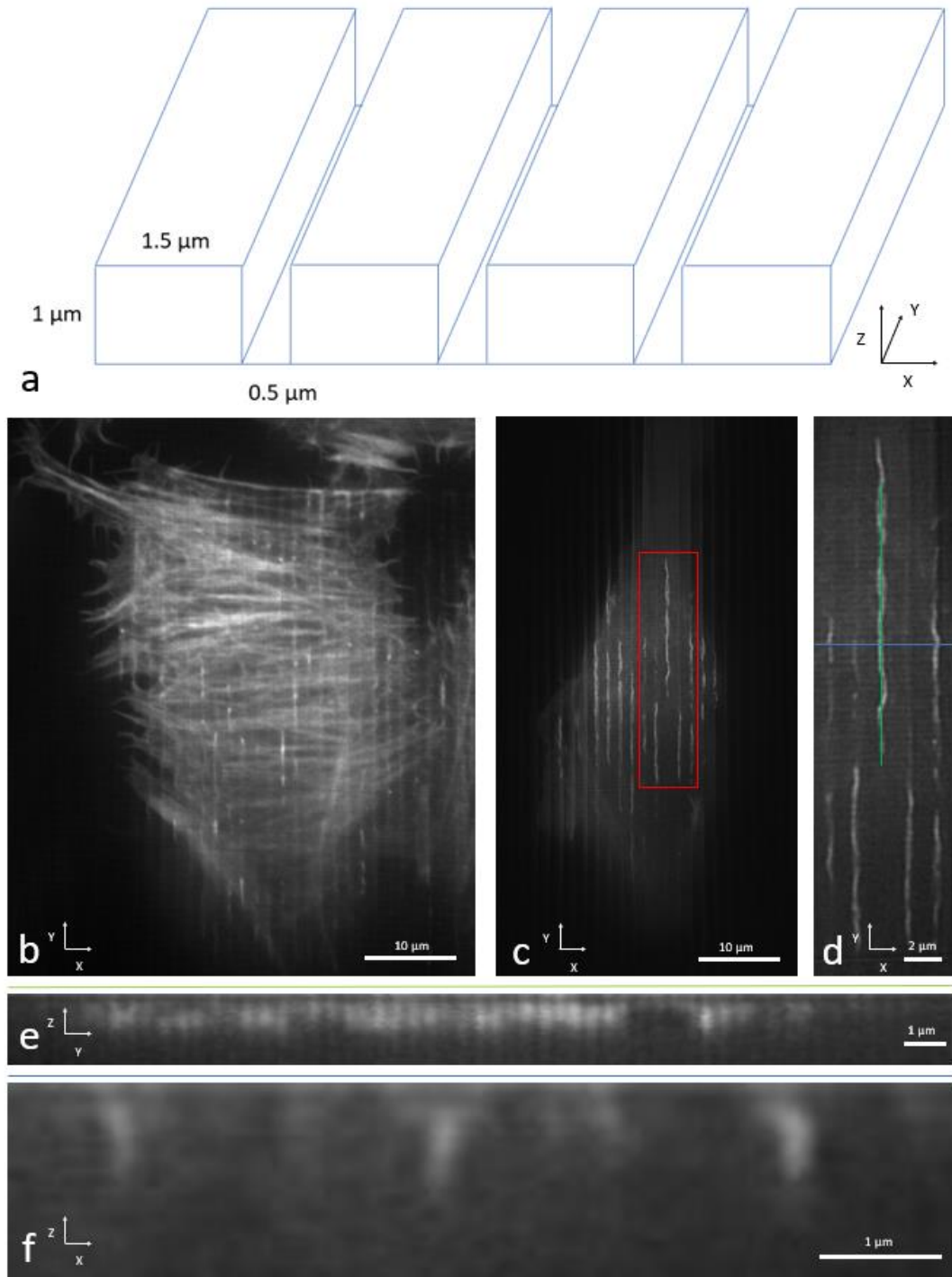


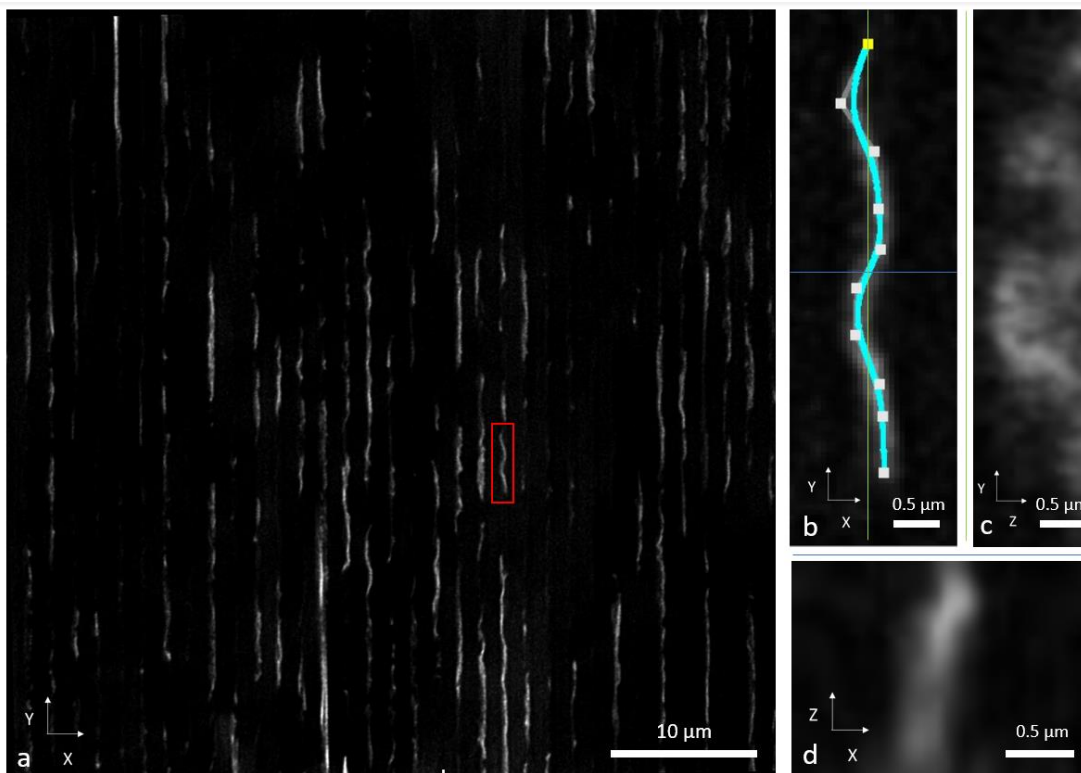
Figure 3.1 Actin structures in live cells

Figure 3.1: a) Nanopatterned groove schematic. b) LifeAct Emerald in live U2OS Cell on nanogrooved pattern. Actin can be seen forming stress fibers, filopodia, and dynamic structures at the cell base. Displayed image is a max-intensity projection over  $2\ \mu\text{m}$  z-axis depth surrounding the grooves. c) LifeAct Emerald in U2OS Cell on another nanogrooved pattern showing wave like structures in XY plane. Displayed image is one plane approximately at the center of the groove depth in z. d) Zoomed in

cutout of red rectangle in (c). e) YZ reslice of (d) along green line. f) XZ reslice of (d) along blue line. 2 cells are shown; data are representative of ~20 observed cells across two experiments.

### 3.3.2 Fixed Cell STED Image Analysis

To further examine the spatial structure of the actin, cells plated on nanogrooved patterns were fixed and stained with Alexa Fluor 594 Phalloidin, and then examined with a Leica SP8 STED microscope. The 3D STED capabilities of the SP8 enables collection of Z-stacks with approximately 100 nm and 200 nm lateral and axial resolution, respectively, i.e with a volumetric resolution ~1.5-fold better than the iSIM. Because of differences between live cell and fixed cell imaging, including the fact that phalloidin and LifeAct GFP stain actin differently, these results are not directly comparable to live imaging described elsewhere. While fixed cell imaging with 3D STED does not provide any additional insight into actin dynamics, the increased spatial resolution should help display fine structure in the observed actin.



*Figure 3.2 3D Super-resolution imaging of actin structures in fixed cells*

Figure 3.2: a) Single XY slice of STED imaging volume showing Alexa Fluor 594 Phalloidin stain in fixed U2OS cell on a nanogrooved pattern. Higher axial resolution allows for the examination of z structure of actin in grooves. b) Zoomed in cutout of red rectangle in (a), shown with point distance minimization curve fit overlaid. c) YZ reslice of (b) at green line. d) XZ reslice of (b) at blue line. 4 cells are shown in a; data are representative of ~25 observed cells across two experiments.

An example STED image can be found in Figure 3.2a, depicting a single slice from a stack of images. The single slice is taken approximately halfway down the groove, showing many actin structures formed within grooved structures. While the fixed actin structures change depth (Z axis) in the groove as a function of position parallel to the groove, as can be seen in Figure 3.2c and d, there is no significant measurable pattern. These structures were examined individually, and curve fitting was performed by point distance minimization using a Fiji plugin [107]. For the full

field of view in Figure 3.2a, all structures above a size threshold (larger than  $\sim 2 \mu\text{m}$ ) were fit to curves. Figure 3.2b shows an example actin structure and the resulting curve fit. These curves were then analyzed using a local derivative approximation (slope) to find relative min/max points throughout each curve. For each curve, relative min/max points were compared to find peak-to-peak amplitude and peak separation. To help mitigate over-fitting, peak measurement values smaller than  $\frac{1}{2}$  pixel were excluded from analysis. A sample curve can be found in Figure 3.3a, along with relative min/max points indicated in red.

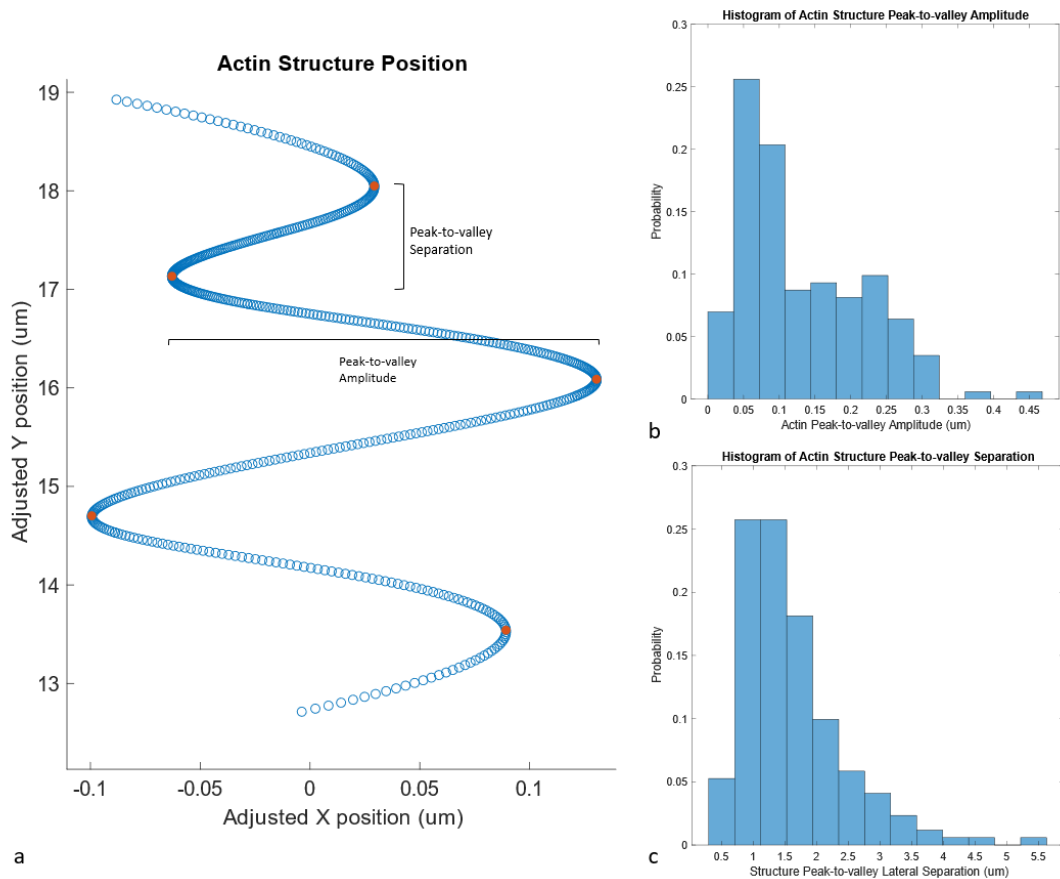


Figure 3.3 Actin structure shape characterization

Figure 3.3: Actin structures were fit to curves, and the resulting curves were analyzed for peak amplitude and separation. a) shows a sample actin structure curve, with identified peaks denoted with red circles. All peaks in Figure 2a were identified computationally, and the distribution of peak amplitude and separation are shown in b)

and c), respectively. Fluorescence localization error is assumed to be less than a detector pixel, or approximately 55 nm, not shown above.

The average peak-to-peak amplitude for the whole field was  $0.13 \mu\text{m} \pm 0.09 \mu\text{m}$ . While the range of amplitudes is wide, all results fall within the  $0.5 \mu\text{m}$  groove width. While it is expected that straight actin structures would have small peak-to-peak amplitudes, roughly half of peak-to-peak amplitudes fall within  $0.1 \mu\text{m}$  to  $0.3 \mu\text{m}$ , suggesting the actin also forms wave-like structures occupying nearly half the groove width (X dimension in 1a). The average peak separation for the whole field was  $1.65 \mu\text{m} \pm 0.93 \mu\text{m}$ . This suggests a peak separation of  $\sim 14\times$  larger than the peak-to-peak amplitude, suggesting the actin structures are pliable enough to display wave-like structure. Intuitively, straight actin structures would have either very short (curve fitting artifact) or very long (few noticeable peaks) peak separation measurements. Because most of these actin structures show a peak-to-peak separation of  $0.5 \mu\text{m}$  to  $3 \mu\text{m}$ , it suggests there is an interesting balance between stiffness and curvature present in these structures.

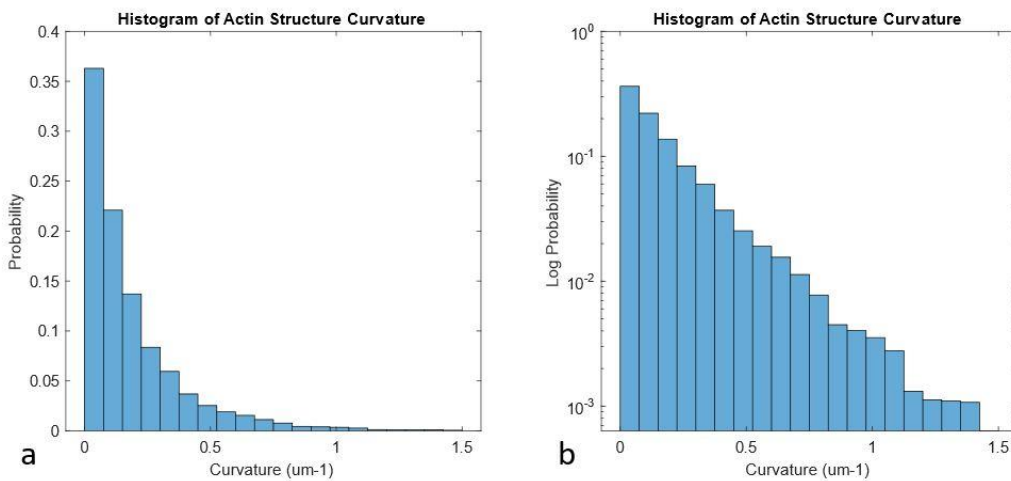


Figure 3.4 Curvature in actin structures

Figure 3.4: Actin structures were fit to curves, and the resulting curves were analyzed for point curvature. a) shows the distribution of point curvature across all actin structures in Figure 2a. b) shows a similar plot on a log scale.

Figure 3.4 shows the distribution of point curvature in all actin structures in Figure 3.2a. The average point curvature was  $0.19 \mu\text{m}^{-1} \pm 0.25 \mu\text{m}^{-1}$ . As a straight line would have near-zero curvature, the distributions in Figure 3.4 show some curvature, but not a statistically significant amount throughout the image.

### 3.3.3 Live Cell Actin Structure and Dynamics

This analysis can be extended to live cell imaging. To further examine the dynamics of actin in live cells, cells plated on nanogrooved patterns were labelled with LifeAct GFP and then examined with the iSIM. In Figure 3.6a, an image with actin structures marked by LifeAct GFP is shown. The structure characteristics are shown in Figure 3.5c and d. The average peak-to-peak amplitude for the whole field was  $0.090 \mu\text{m} \pm 0.078 \mu\text{m}$ . While the range of amplitudes is wide, all results fall within the  $0.5 \mu\text{m}$  groove width. The average peak separation for the whole field was  $2.35 \mu\text{m} \pm 1.38 \mu\text{m}$ . The average point curvature was  $0.08 \mu\text{m}^{-1} \pm 0.2 \mu\text{m}^{-1}$ . In general, these values show that structure characteristics are similar between live and fixed cells. In the data examined, structures are less pronounced in live cells, as the average curvature and structure amplitudes are lower overall.

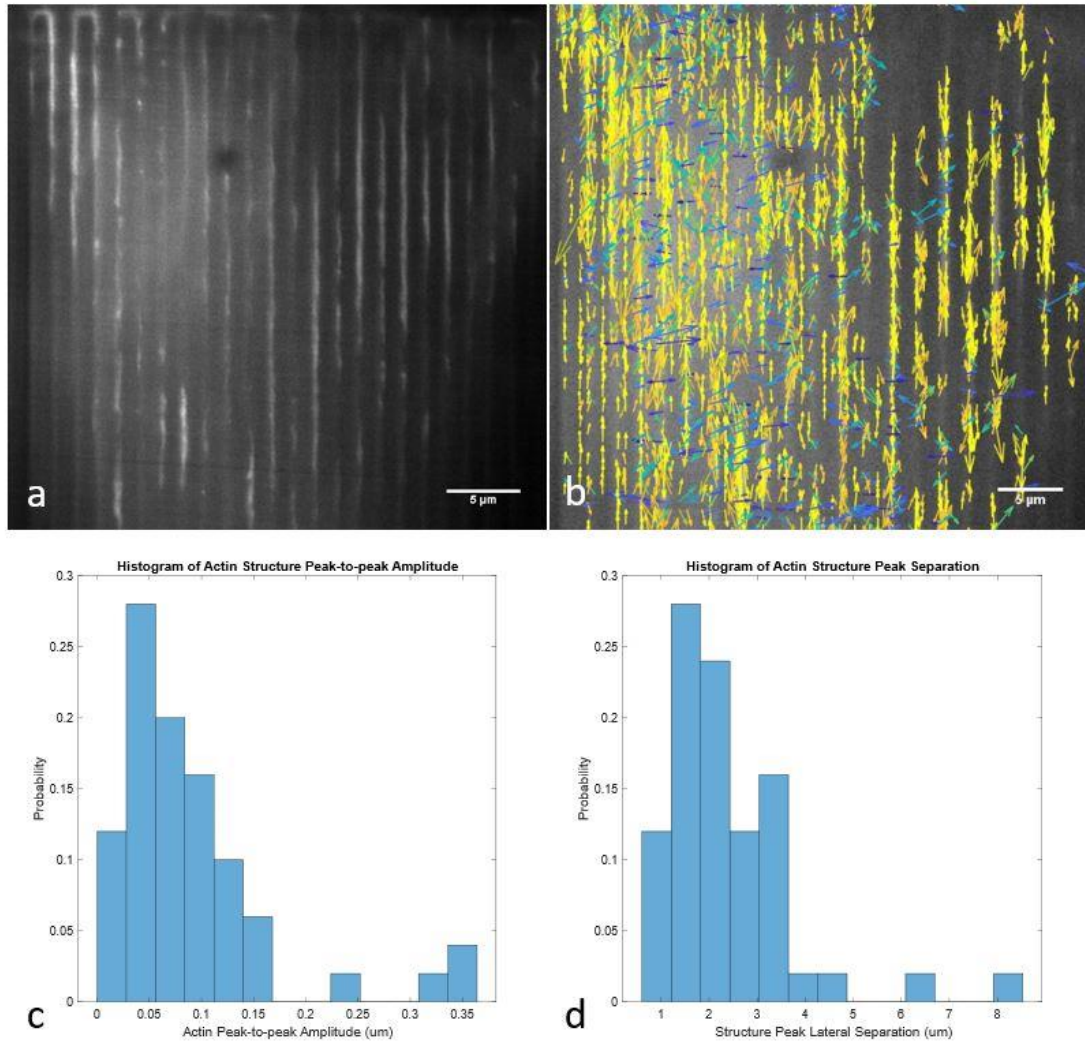


Figure 3.5 2D Actin structures and dynamics in live cells

Figure 3.5: a) LifeAct Emerald in U2OS Cell on nanogrooved pattern. b) Image flow vectors calculated between two images in a timelapse series, spaced by 20 sec. Vectors are colored such that motion parallel to grooves is yellow and perpendicular is blue. Distribution of peak amplitude and separation are shown in c) and d), respectively.

By using 2D optical flow analysis, we can examine the motion of actin between consecutive frames in a timelapse. The two frames analyzed in Figure 3.5b were taken at a Z plane approximately halfway down the depth of the groove (~0.5 μm above the coverslip). As can be seen in Figure 3.5b, motion at this plane is primarily parallel to the axis of the grooves.

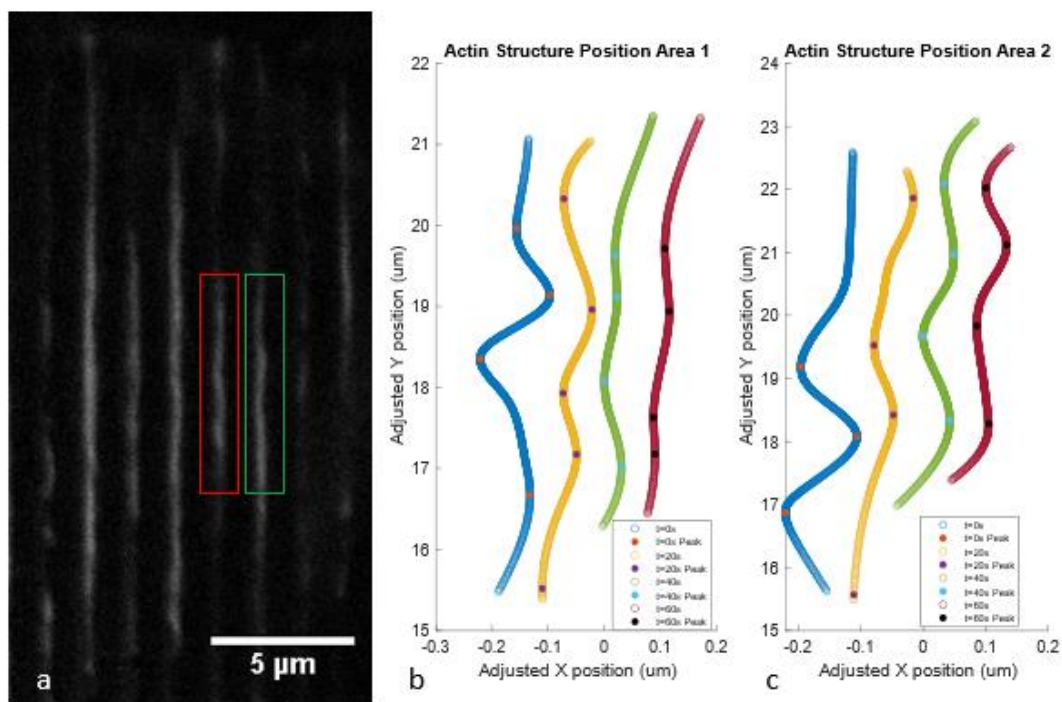
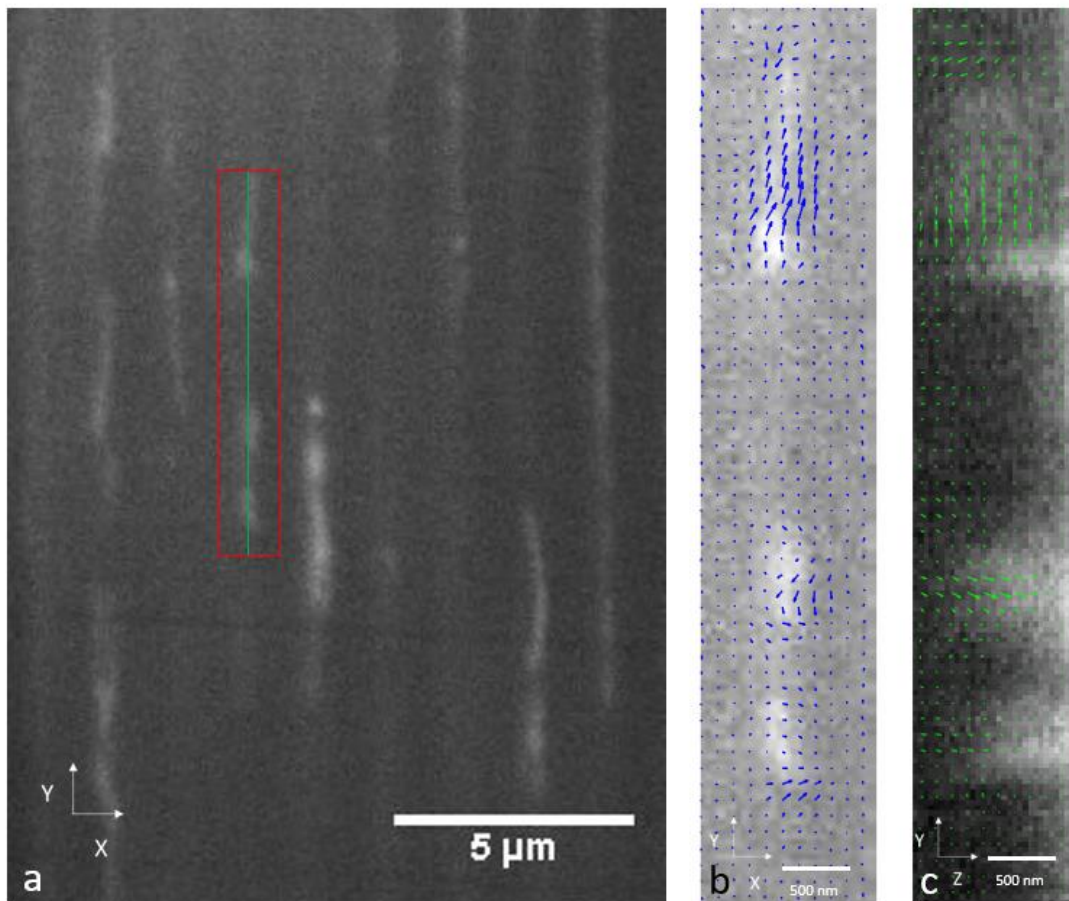


Figure 3.6 2D Timelapse imaging of actin structures in live cells

Figure 3.6: LifeAct Emerald in U2OS Cell on nanogrooved pattern. Cells were imaged every 20 seconds to study the evolution of actin structures over time. a) shows a sample frame from timelapse fluorescence imaging, while b) and c) show actin in two separate areas, representing the red and green rectangles, respectively. Successive timepoints in b) and c) were shifted by 0.1  $\mu\text{m}$  each for clarity. Cells were imaged approximately in the center of the groove depth. Fluorescence localization error is assumed to be less than a detector pixel, or approximately 55 nm, not shown above.

Using the same curve fitting process described above, it is possible to examine the evolution of actin structures over time. U2OS cells on nanogrooved patterns were imaged every 20 seconds, and the resulting actin fluorescence was analyzed for curve position. When consecutive time points are shown on the same plot, as is done in Figure 3.6, it is possible to gain insight into the evolution of actin structures over time. Figure 3.6 shows that the peaks and valleys of actin structures move in both x and y dimensions over time, but motion over the observed period (60 seconds) was generally constrained to within 1  $\mu\text{m}$ .

2D Lucas-Kanade optical flow analysis can be extended to examine image flow in 3D [104]. As in the 2D case, 3D Lucas Kanade optical flow assumes a constant velocity for the 3D neighborhood of voxels around the target voxel, and again uses a weighted least-squares fit to find the image flow vector. 3D timelapse imaging of actin can be analyzed using 3D optical flow to gain insight into actin movement along the depth of the groove.



*Figure 3.7 3D Actin dynamics in live cells*

Figure 3.7: a) LifeAct Emerald in U2OS Cell on nanogrooved pattern. b) Shows XY optical flow vectors for actin in a groove, area shown in red rectangle in a). c) Shows a YZ reslice along green line in a), along with associated optical flow vectors. Optical flow vectors are sampled every third pixel and scaled for ease of viewing. Source image collected from 3D timelapse of LifeAct Emerald in U2OS cell.

Figure 3.7 shows 3D optical flow analysis of actin in live cells. Figure 3.7a depicts a single slice from a stack of images, with the stack representing one timepoint. The single slice is taken approximately halfway down the groove, showing many actin structures formed within grooved patterns. Z-stacks of images from two consecutive timepoints are compared to examine local motion. As is observed in Figure 3.6b, Figure 3.7b shows actin moving primarily along the y-axis of the grooves, with less motion along the x-axis. Figure 3.7c shows both movement parallel to the y axis of the grooves (as seen in in Figure 3.7b), as well as motion parallel to the z axis of the grooves.

Latrunculin A associates with actin monomers and prevents them from polymerizing, so it can be used to disrupt F-actin structure in cells. I examined the response of actin structures, visualized by LifeAct, to two different concentrations of Latrunculin A. Cells plated on grooved structures were incubated at 37°C for 4 hours after exposure to 2  $\mu$ L DMSO control, 2  $\mu$ L DMSO with 250 nM Latrunculin, and 2  $\mu$ L DMSO with 500 nM Latrunculin. 2  $\mu$ L DMSO control trials had cell viability and transfection efficiency issues and were inconclusive. Still, trials for both concentrations of Latrunculin appear to disrupt cell shape and elongation along the grooves, consistent with expected results. In the cells observed, 500 nM Latrunculin disrupted nearly all measurable actin filaments, while 250 nM Latrunculin disrupted stress fibers throughout the cell but left actin filament structure in the grooves.

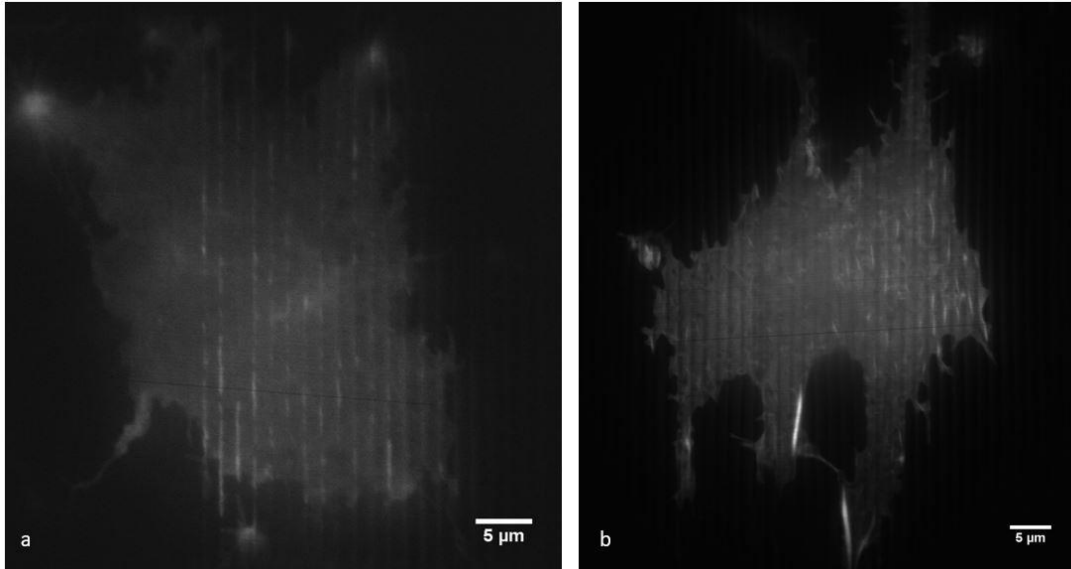


*Figure 3.8 Effects of latrunculin on actin structures in live cells*

Figure 3.8: LifeAct Emerald in U2OS Cell on nanogrooved pattern. a) Incubated for 4 hours at 37°C with 250 nM Latrunculin. b) Incubated for 4 hours at 37°C with 500 nM Latrunculin.

### 3.4 Discussion

A variety of 3D, 2D timelapse, and 3D timelapse images were collected to observe live cells expressing LifeAct Emerald. Actin structures visualized by fluorescence showed actin forming stress fibers and filopodia, but also forming structures near the base of the cell. Grooved patterns 500 nm wide by 1 µm deep, spaced by 1.5 µm (See Figure 3.1a), were used to examine the actin structure response to external structures. While the grooved patterns may impact the resolution of fluorescence imaging or introduce imaging artifacts, refractive index matching to the glass coverslip should minimize these effects. Images collected on planes inside the grooves show that actin fills the groove with patterned structures. Some areas of these structures resemble transverse waves along the length of the of the grooves (y-

axis), with substructures in some areas showing features with high curvature. While the structures also show structure parallel to the depth of the grooves (z-axis), this structure does not appear to show a consistent or well-defined pattern.

Optical flow analysis was used to examine the movement of fluorescently tagged actin structures in timelapse images series of live cells. 2D optical flow analysis provides further evidence that actin migrates preferentially along the axis of the grooves (y-axis). 3D optical flow analysis has not been repeated over enough cells and replicated experiments to be considered well-established, so the above results are preliminary. Future work repeating these studies will enable more general characterizations about actin dynamics to be made. Still, 3D optical flow analysis suggests that in addition to propagating preferentially along the ridges, actin also explores the depth of the grooved patterns. While optical flow analysis is useful for extracting velocity information from cellular processes like these, it is limited to slowly moving signals that do not change significantly. As such, it is sensitive to fluorescence timelapse imaging with significant photobleaching which causes a decrease in overall signal level. Also, actin depolymerization can lead to the disappearance of structures and the violation of optical flow assumptions.

To study the evolution of actin structures over time, timelapse fluorescence imaging was performed. By fitting curves to the actin structures and studying how these curves change over time, insight can be gained into the nature of the actin structures and their dynamics. Figure 3.6 shows that in addition to the leading edge of actin, which had been the focus of prior work on propagating actin waves [88], these actin structures in live cells are themselves dynamic. The peaks and valleys of the

actin structures move in both lateral dimensions, suggesting that the actin structures are either freely moving or being moved by another cellular process, such as myosin motors. The actin structures are thin, typically observed to be ~500 nm, and move quickly on a small spatial scale, so these measurements are enabled by fast super-resolution microscopy. The shapes and dynamics of these structures can help determine their structural components.

The fact that the structures appear to change their shape significantly over 60 seconds suggest they are either soft and pliable or being actively moved. This motion could be partially attributed to fitting and localization artifacts, but the motion is on a greater scale than could be attributed to solely fluorescence localization error (less than 55 nm). Because the actin structures appear to demonstrate some minimum stiffness, as well as a significant fluorescence signal level (more than would be expected from a single filament), the data suggest that the observed actin structures are comprised of groups of actin filaments. While this analysis was only performed on timelapse data from one experiment, a larger data set from further investigation will help describe the actin dynamics with more confidence. Also, the time step of 20 seconds is large to effectively freeze the observed motion, so future repetitions will image more rapidly.

Cells treated with high doses (~500 nM) of Latrunculin to disrupt F-actin do not show measurable actin filaments in the form of stress fibers or any actin structures. Latrunculin at lower doses (~250 nM) disrupts stress fibers but not necessarily actin structures within grooves. In addition to repeating the discussed experiments, future work would involve examining the effects of a variety of

different latrunculin concentrations, studying the direct effect of latrunculin treatments on dynamics as it is applied, as well as looking at recovery from latrunculin treatments. A variety of groove dimensions would also provide additional insight to the resulting actin structures.

Actin plays an important role in driving cell motility. In addition to generating force for cell motion, it forms the structure for cellular protrusions that interact with the surrounding environment. Cell migration plays an important role in many physiological processes, including cancer metastasis, so studying actin's role in the process has important implications. Dynamic actin structures in live cells help generate force for cell motility, so characterizing the form and function of these structures will hopefully shed light on the cellular processes involved. Studying the actin structures that form in response to external stimuli will help illuminate how cells interact with their environments and achieve motility. By looking at the evolution of these actin structures over time with timelapse fluorescence imaging, valuable insights into the makeup and dynamics of these structures can be gained. This characterization is enabled by high spatiotemporal resolution imaging made possible by many recent advances to fluorescence microscopy techniques.

## Chapter 4 Anticipating, Measuring, and Minimizing MEMS Mirror Scan Error to Improve Laser Scanning Microscopy's Speed and Accuracy

The following chapter is adapted from Giannini, York, and Shroff (2017) [108]. Andrew York and John Giannini conceived idea and implemented optimization software. John Giannini built the optical systems and acquired data. Supplementary Figures can be found in Appendix A1.

### 4.1 Introduction

Many applications in biomedical microscopy require imaging with high spatiotemporal resolution. Imaging techniques now provide spatial resolution at or surpassing the diffraction limit, and temporal resolution down to the sub-millisecond level. The ability to perform accurate, controllable, high speed scanning is fundamental to most of these methods. For example, imaging at frame rates of tens to hundreds of Hz is necessary to capture functional dynamics in neural tissue [109], [110]. In rescan confocal microscopy [71], a super-resolution imaging technique, accurate synchronization of excitation and emission scanning is essential in order to extract sub-diffractive spatial information from the sample. Similarly, in light sheet microscopy, strict synchronization of the illumination beam with the camera's rolling shutter enables real-time rejection of out-of-focus light [78]. Regardless of the particular application, temporal resolution is often limited by choice of scanning hardware and scanning mechanism.

Many modern laser scanning microscopy techniques use galvanometer-controlled mirrors to move the illumination beam relative to the sample [79]. Larger (~5mm) non-resonant galvanometers, traditionally used for slow scanning and step-stop operation, are very accurate and feature low settling times (100-300  $\mu$ s) for small

motions. Galvanometer-controlled mirrors are fundamentally speed limited by their size, inertia, and the requirement to slow down and reverse direction. For most moderate fields of view (FOVs), these mirror scanning systems have traditionally limited imaging frame rates to several Hz [111]. Resonant galvanometer-controlled mirrors are capable of much higher speeds than conventional galvanometric scanners, on the order of  $\sim 10^4$  lines per second, enabling video rate or faster frame rates [112]. However, the fixed-frequency sinusoidal motion of resonant scanners impedes imaging at variable rates or random-access scanning (where only discrete portions of the field of view are scanned [113]). Also, resonant scanning is not performed at constant velocity, so illumination dwell time is not constant, resulting in non-uniform detection sensitivity across the region of interest.

To a lesser extent, rotating polygonal mirrors and acousto-optic deflectors (AODs) are also used in laser scanning applications, and they present their own advantages and drawbacks [79]. Polygonal mirrors enable rapid scanning (1-4 kHz line rates) with adjustable speed. In contrast to resonant mirrors, the angular range is limited by the number of facets, effectively fixing the field of view. Another disadvantage of polygonal mirrors is that the rotation axis is distant from the mirror face, meaning over the scan period of each mirror face, the axial path length varies during a scan. AODs use radio frequency sound waves to create a tunable diffraction grating that is used to control laser beam output angle. The absence of moving mechanical parts allows AODs to scan at very rapid speeds (approaching line rates of 1 MHz), and they allow random-access scanning, which enables frame rates of  $> 1$  kHz [113]. Drawbacks of AODs include their relatively small scan range ( $< 4$

degrees) and high dispersion. Such dispersion leads to transmission losses and wavefront distortions that can be compensated to some degree with additional hardware [113], [114]. Because AODs do not transmit emitted light from the sample efficiently, they are not typically used for rescanning applications.

Improvements in microelectromechanical systems (MEMS) scanner technologies have permitted their increasing use in high speed beam steering. MEMS mirror scanners are available in a range of sizes (~0.5-5 mm) and can access moderate angles ( $> \pm 10$  degrees optical) at high speeds (300 Hz to 6 kHz line rates). MEMS scanners have proven useful for applications in optical coherence tomography [115], [116], confocal reflectance microscopy [117], two-photon microscopy [82], microendoscopy [118], and light-sheet microscopy [119].

MEMS mirrors, galvanometer-controlled mirrors, and polygonal mirrors are all typically driven by either an open-loop or closed-loop control system. In an open-loop system, the output of the system does not inform or improve the control action at all. Many galvanometers and polygonal mirrors provide a built-in means for sensing the position of the mirror either electronically or optically. This allows for closed-loop control, where the position sensing corrects and improves the control action. An example of a closed-loop feedback mechanism is proportional, integral, and derivative (PID) control [120], which incorporates and predicts past, present, and future sources of error to improve performance. Until recently [121], MEMS mirrors have been typically controlled with an open-loop system.

Here we present a method to “close the loop” for a MEMS device without built-in position sensing, using a feedback mechanism comparable to PID control.

Our improved control algorithm enables faster, more precise scanning than previously possible. First, we examine the performance of a MEMS scanner with traditional control methods. Second, we account for the device's impulse response in the control algorithm and demonstrate improved scan accuracy and performance. Third, we show the accuracy of the algorithm can be further improved by iteratively measuring and correcting for the observed behavior of the MEMS mirror. Finally, we demonstrate applications of our control algorithm by using it to optimize fast raster patterns and perform point scanning microscopy on biological test specimens.

## 4.2 Materials and Methods

### 4.2.1 Laser Scanning Test Rig

We began our investigation using a 1.2 mm MEMS mirror (Mirrorcle, A1B2.5-1200AL-DIP24-A/TP), with an angular range of  $\pm 9.2$  degrees optical, which allowed for a large field of view, and a resonant frequency of 3.25 kHz, which facilitated rapid scanning. In order to characterize mirror performance we built a test rig (Figure 4.1), which scanned a laser beam across a camera chip.

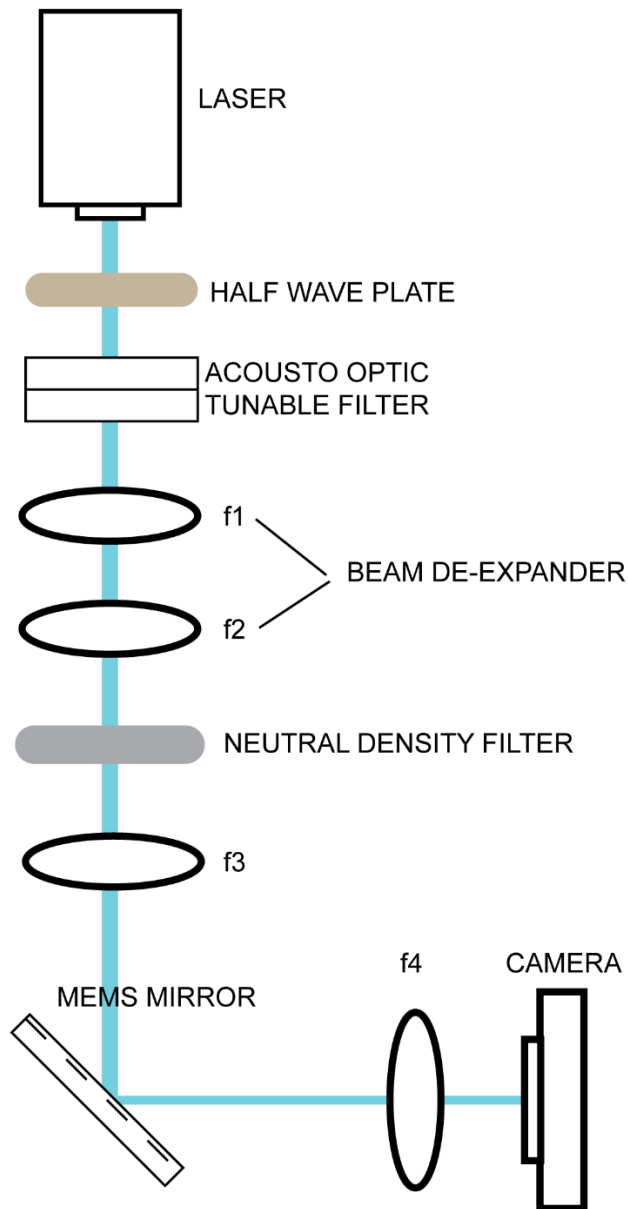


*Figure 4.1 Laser scanning test rig*

Figure 4.1: Test rig for characterizing mirror performance.

A 200 mW, 488-nm laser was used for illumination. The laser was passed through an acousto-optic tunable filter (AOTF) for fast shuttering and dynamic intensity control. The intensity of the laser through the AOTF was maximized by

tuning the rotation of a half-wave plate placed in front of the AOTF. After the AOTF, the beam was contracted by  $7/8$  with a telescope. The lenses in this telescope,  $f_1$  and  $f_2$ , were separated by the sum of their focal lengths to preserve beam collimation. Post-telescope, the collimated beam was then passed through a reflective neutral density (ND) filter to further attenuate intensity. The attenuated beam was focused onto the pivot point of a 1.2 mm diameter MEMS mirror (placed in a DIP24 package and mount) by placing lens  $f_3$  one focal length away from the MEMS mirror. Because lens  $f_4$  is also placed one focal length away from both the MEMS mirror and the scientific-grade complementary metal-oxide semiconductor camera, scanning the angle of the mirror changes the position of the beam on the camera. This allows us to measure the mirror's approximate angle vs. time in response to an input voltage vs. time by taking a series of images and observing the resulting laser positions on the camera. Voltages were issued from a PC via an analog out card, and a bias differential quad-channel (BDQ) amplifier was used to amplify voltage signals provided to the MEMS mirror. A complete components list can be found in A1.1.

#### 4.2.2 Point Scanning Microscope Test Rig

To demonstrate the value of our waveform optimization method for imaging, we also built a simple point scanning fluorescence microscope (Figure 4.2).

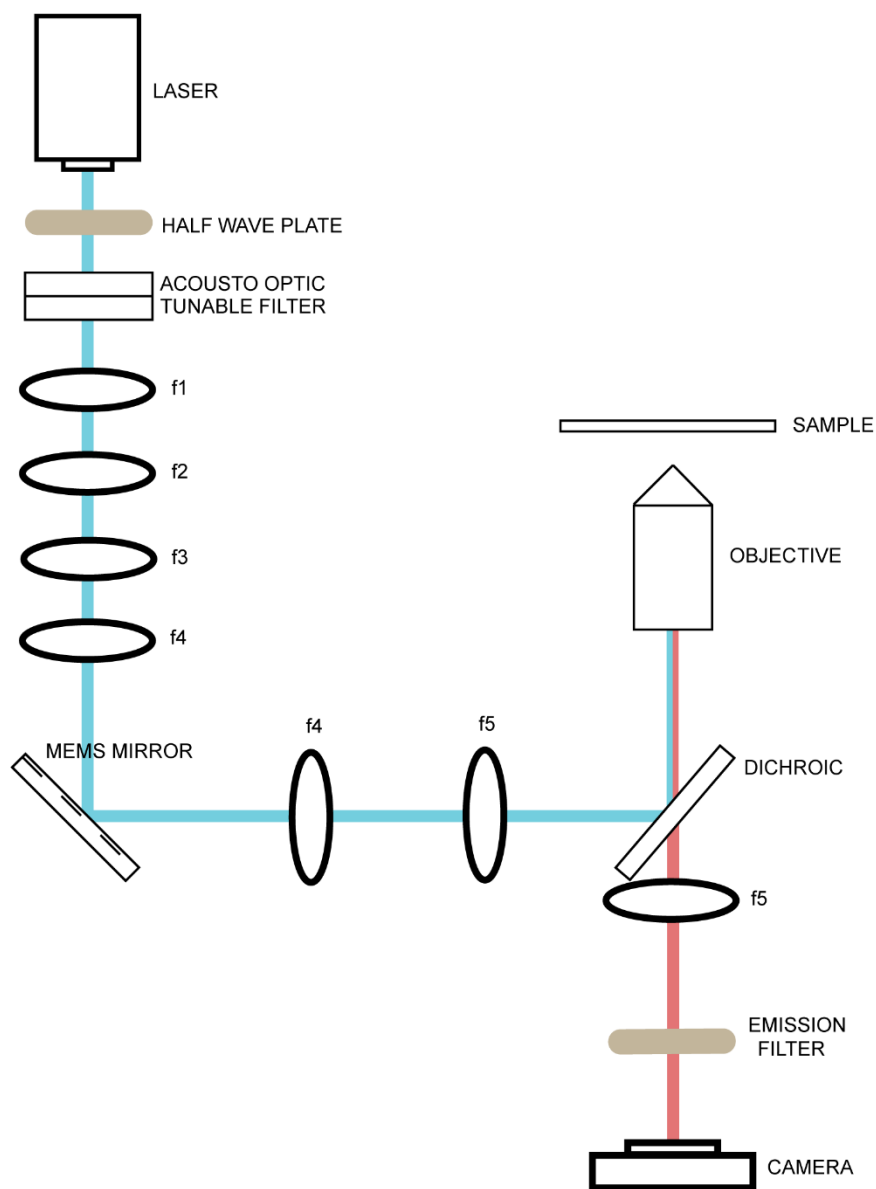


Figure 4.2 Point scanning microscope test rig

Figure 4.2: Test rig for point scanning fluorescence microscopy.

As before, a 200 mW, 488-nm laser was used for illumination and fast shuttering and dynamic intensity control used achieved with an AOTF. After the AOTF, the beam was contracted by two consecutive telescopes. The first telescope contracted the beam by  $7/8$ , and the second by  $8/25$ . The beam was then scanned by a

1.2 mm diameter MEMS mirror placed in a DIP24 package. The MEMS was imaged to the back focal plane (BFP) of the objective with a telescope and a dichroic beamsplitter. Fluorescence from the sample was collected with the same objective, transmitted through the dichroic beamsplitter, and passed through an identical tube lens onto a scientific-grade complementary metal-oxide semiconductor camera. Excitation light was removed by an emission filter placed before the camera. Voltages were issued from a PC via an analog out card, and a bias differential quad-channel (BDQ) amplifier was used to amplify voltage signals provided to the MEMS mirror. A complete components list can be found in A1.2.

## 4.3 Results

### 4.3.1 MEMS Mirror Characterization

In order to successfully gauge the mirror's capabilities, we needed the ability to accurately measure the mirror's angle vs. time in response to an input voltage vs. time. To enable this measurement, we built the test rig shown in Figure 4.1. Because this rig enables us convert position on the camera to mirror angle, if we strobe the laser light, we can use the position of the laser on the camera to determine the mirror angle at the time of the strobe. To completely measure the angle vs. time response of an extended input voltage, it is necessary to collect many of these measurements. This was accomplished by repeating the input voltage while strobing the laser once per input, varying the delay of the illumination strobe to map out the mirror's response. Between successive strobos, we allowed for a cooldown period (~0.5 seconds) to ensure that each measurement was independent of the last.

To characterize the mirror response at different speeds, we devised several similar simple scan patterns, consisting of four constant-velocity sweeps (two cycles over  $\sim 0.85$  degrees), that differed only in relative speed (Figure 4.3). At slow scan speeds (3-8 ms/sweep, Figure 4.3a and b), an approximation of the mirror impulse response as a delta function produced fairly accurate results, because the settling speed of the mirror was fast compared to the desired scan frequency; the angular error (difference between desired and actual response of the MEMS mirror) was  $< 10\%$ . The mirror could thus be controlled by a “naïve” waveform, directly proportional to the desired scan pattern (A1 Supplementary Figure 1). However, as the speed and complexity of the desired scan pattern increased (0.6 ms/sweep, Figure 4.3c), the accuracy of this method degraded to  $\sim 25\%$  peak error. Fast, high-accuracy operation was not possible without accounting for the mirror’s impulse response.

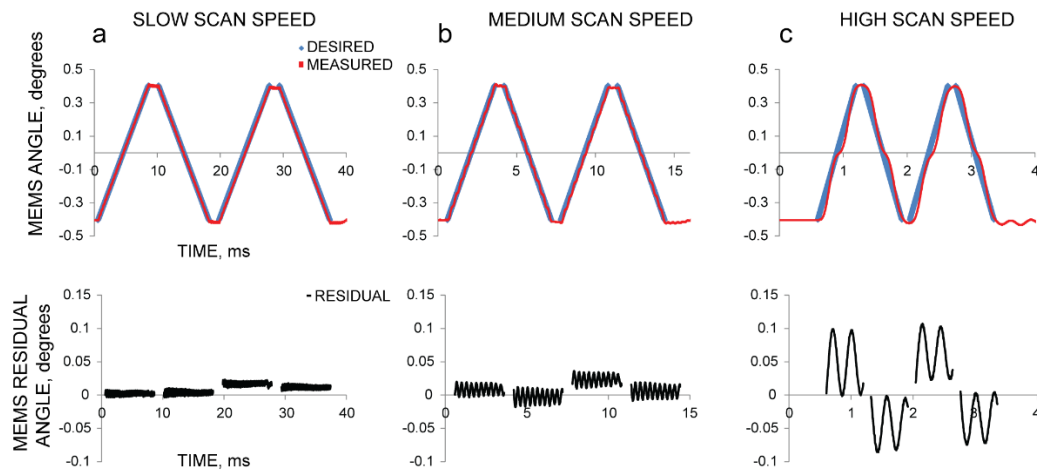


Figure 4.3 Naïve input voltages become inaccurate for high-speed MEMS operation

Figure 4.3: At slow scan speeds (left column (a), 8 ms/sweep, 1.6 ms/turnaround between forward and backward sweeps), using an input directly proportional to the desired result produces a reasonably accurate output. However, as the speed of the scan increases (middle Column (b), 3 ms/sweep, 0.6 ms/turnaround; right Column (c), 0.6 ms/sweep, 0.12 ms/turnaround), residual error between the desired and achieved patterns also increase. At speeds desirable for many scanning applications (right column (c)), the scan pattern is unusable. The top row compares the desired scan pattern

with the measured result. The bottom row shows the residual error (between the desired and achieved pattern).

#### 4.3.2 Mirror Control Optimization Algorithm

We used our strobe-based measurement system to characterize the mirror's impulse response, finding that it was modeled well by an exponentially-decaying sinusoid. With the desired scan pattern and a model of the mirror impulse response, we used a modified Landweber deconvolution [122] to solve the inverse problem of what voltage waveform needed to be sent to the mirror to produce the desired output scan pattern more accurately:

$$V(n+1) = V(n) + \lambda H^T (H(V(n)) - D) \quad (1)$$

In Equation (1),  $V(n)$  represents the current input voltage waveform at iteration  $n$ ,  $\lambda$  represents the relaxation factor,  $\mathbf{H}^T$  represents the transpose operator,  $\mathbf{H}$  represents the forward operator, and  $D$  represents the desired (known) output.

The iteration has two major components: a forward operator,  $\mathbf{H}$ , and a transpose operator,  $\mathbf{H}^T$ . The forward operator consists of a blurring step, where the input is convolved with the mirror impulse response to produce an expected result, and a cropping step, where the expected result is cropped to only account for important scan regions. After cropping and blurring the input voltage to produce the expected output, we compare the result to the desired (and similarly cropped) result to produce a residual. The transpose operator,  $\mathbf{H}^T$ , consists of a crop transpose step, where the residual is zero padded to restore the length of the original input voltages, and a blur transpose step, where the residual is convolved with the time-reversed impulse response. The transpose operator assigns blame to the input for disagreements between the expected response and the desired response, producing a correction voltage. This correction voltage is added to the original input to produce an

improved input voltage (A1 Supplementary Figure 1b). For our waveforms, we found that the algorithm usually converged with  $n \approx 5000$  iterations using  $\lambda = 0.004$  (30 – 60s on our acquisition computer). Setting higher values for  $\lambda$  can speed convergence but also occasionally causes divergence.

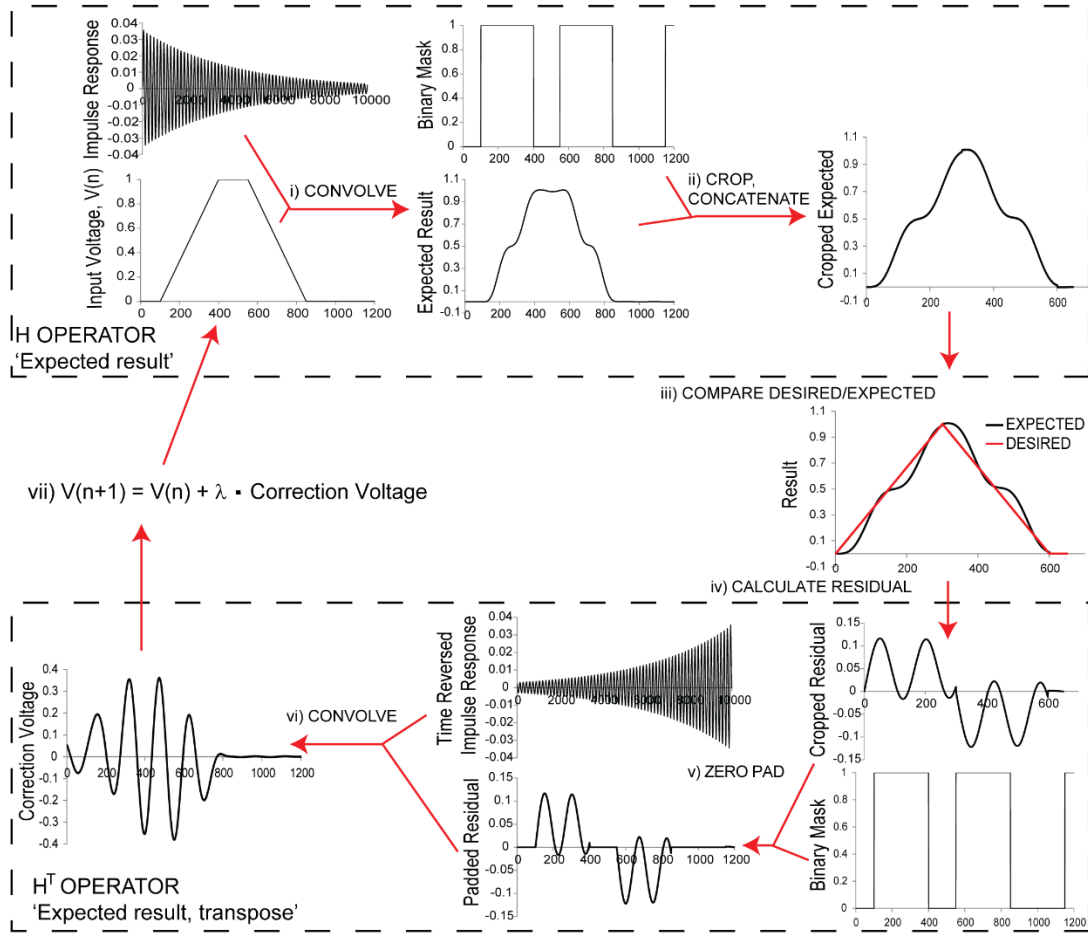


Figure 4.4 Landweber-based deconvolution optimization

Figure 4.4: After measuring each MEMS mirror’s response to an impulse, iterative deconvolution can be used to determine a set of input voltages that will more closely produce the desired output scan pattern. We use a Landweber iteration to solve this inverse problem. The iteration has two major components: A forward operator ( $H$ ), which takes a desired input and produces the expected result after convolution with the MEMS mirror impulse response, and a transpose operator ( $H^T$ ), which assigns blame to the input for disagreements between the expected response and the desired response. The forward operator consists of: **i)** a blurring step, in which the current set of input voltages  $V(n)$  is convolved with the impulse response, and **ii)** a cropping step, in which only the results in the scan regions are considered. Cropping is performed because

constraining the procedure to defined scan regions allows for higher accuracy in these regions (see A1 Supplementary Figure 2), and because it is difficult to define exactly what the "desired" result is in undefined regions. Practically we carry out the cropping operation by comparing the blurred voltages with a binary mask (defining the constrained scan regions) and concatenating the resulting masked regions. In addition to the constrained scan regions, there is a small constrained region at the end of each waveform to ensure that the mirror settles quickly to its original position. After producing the cropped, blurred voltages, we compare **iii**) the result to the desired (and similarly cropped) result to produce a residual **iv**). The transpose operator consists of a 'crop transpose' step **v**), where the residual is again compared to the binary mask and zero padded to restore the length of the original input voltages; and a 'blur transpose' step **vi**), where the padded residual is convolved with the time-reversed impulse response. This produces a 'correction voltage' which is multiplied by a relaxation factor  $\lambda$  and added to the original input voltage  $V(n)$  to produce a corrected input voltage  $V(n + 1)$ , **vii**). Empirically, we find that  $\lambda = 0.004$  and  $n = 5,000$  iterations produce good results. For clarity, we have omitted units on the vertical (proportional to voltage) and horizontal (time or index) axes in all graphs.

Because many scanning applications have regions where accuracy is unimportant (e.g. flyback regions), we modified the Landweber iteration (Figure 4.4) to use only important regions for optimization. This modification makes it possible to achieve higher accuracy in important areas of the scan pattern by neglecting unimportant areas (A1 Supplementary Figure 2).

The computational burden associated with repeated convolution operations makes it necessary to optimize large waveforms piecewise. The long tail of the mirror's impulse response means that changes at the beginning of a large waveform influence later portions of the waveform, so waveforms were all optimized piecewise from beginning to end. Also, for all of our optimized waveforms, we added a short constrained region at the end of each waveform to ensure that the mirror settled properly to its original position.

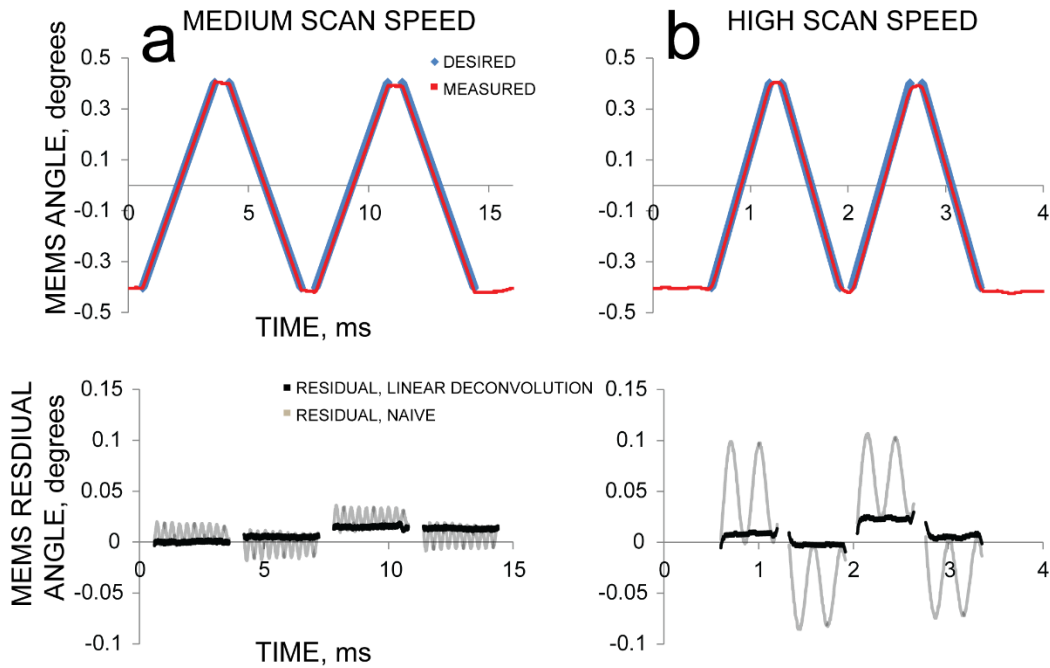


Figure 4.5 Using linear deconvolution to determine input voltage improves scan accuracy compared to naïve voltages

Figure 4.5: The response of the mirror at high speed can be greatly improved by using Landweber deconvolution to determine the input voltage. However, nonlinearities in the mirror response still produce a non-trivial residual. As in Figure 4.3, the top row shows the desired scan pattern and measured result, and the bottom row shows the residual. Compare left (a) and right (b) columns to Figure 4.3b, c middle and right columns, respectively; residual data from Figure 4.3b, c is shown here in gray.

Our modified Landweber iteration greatly improved the accuracy of the achieved scan pattern (Figure 4.5). Using the optimization algorithm reduced the maximum residual between desired and achieved pattern two-fold for the medium scan speed (3 ms/sweep, Figure 4.5a) and four-fold for the high scan speed (0.6 ms/sweep, Figure 4.5b). While this improvement is significant, the residual was worse for patterns at higher speeds. We suspected that the residual differences were due to nonlinearities in the mirror’s impulse response that were not accounted for by our linear deconvolution method. To address this issue, we developed another iterative process to reduce this residual by further improving the input voltage. We

started with the same Landweber-based algorithm to produce an input voltage,  $V(n)$ , that we expected to produce the desired scan pattern,  $D$ . Next, we measured the mirror's actual response, and calculated the residual between desired and measured scan pattern. Then we set  $D$  to the measured residual, re-ran our Landweber algorithm to calculate a correction voltage optimized to produce the residual, and subtracted this voltage from the previous input voltage, producing an improved voltage waveform with lower residuals.

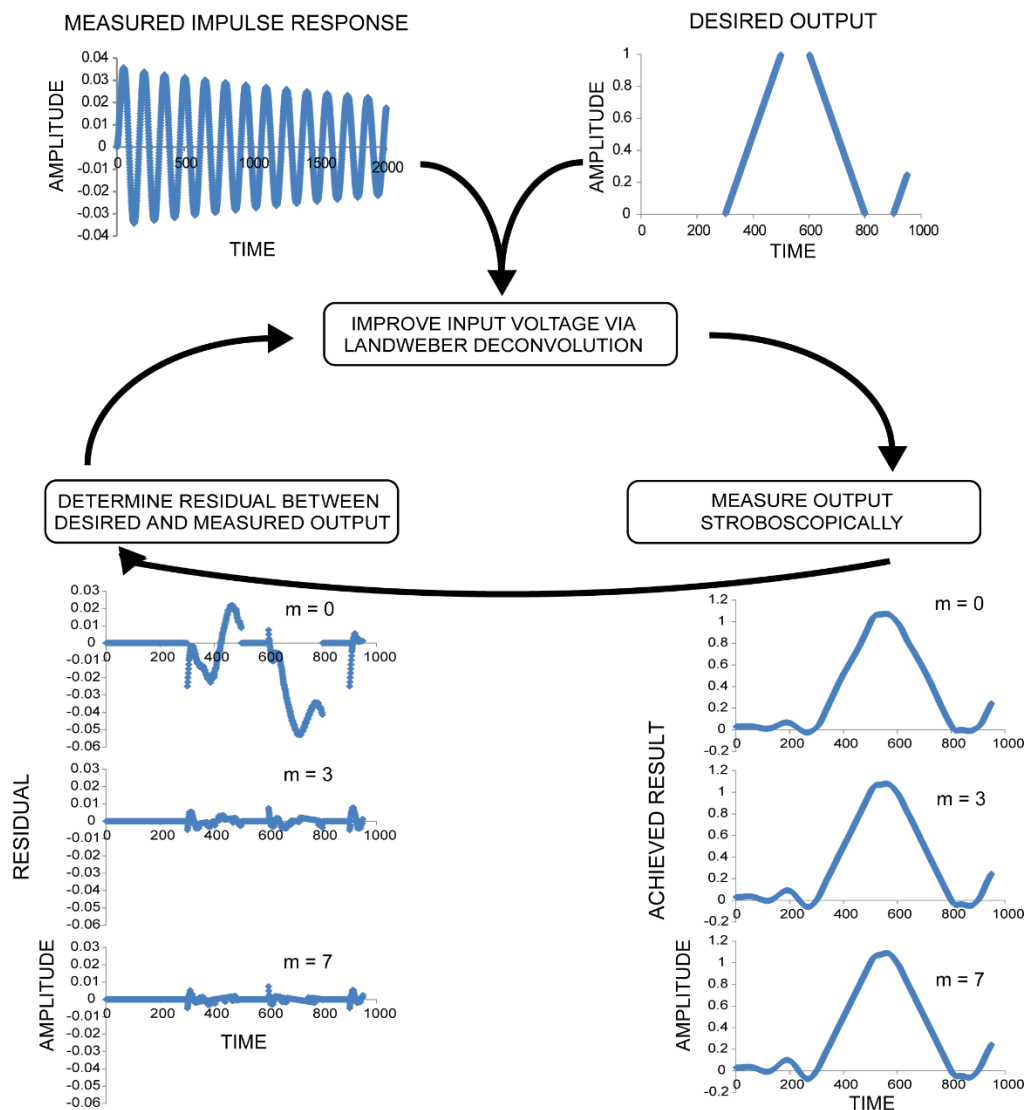


Figure 4.6 Overview of iterative, measurement-based deconvolution method for precise MEMS mirror control

Figure 4.6: Given the measured impulse response (top left) and desired output (top right), deconvolution (middle) provides an input that produces a measured output that approximates the desired output (right,  $m = 0$ ). Nonlinearities in the mirror's response lead to a difference (residual, left,  $m = 0$ ) between expected and measured responses, especially at high speeds. However, the deconvolution algorithm can incorporate the measured residual, computing a modified input that reduces the residual error. Repeating this procedure over a few measurement cycles (examples shown after 3, 7 iterations) dramatically lowers the residual, producing the desired result with high accuracy.

By repeating this outer iteration based on measured residuals (Figure 4.6), we obtained a nearly optimal set of input voltages for a desired scan pattern (A1 Supplementary Figure 1c). We found that after one iteration of the optimization algorithm ( $m=0$ ), the error was usually within  $\pm 5\%$  of the desired result. After a few iterations ( $m=3$ ), the error was within  $\pm 1\%$  of the desired result, and after more iterations ( $m=5$ ), the results were only marginally improved (Figure 4.7). Including measurement and computation time, optimization of these test waveforms ( $m = 5$  iterations) was achieved in  $\sim 1$  hour.

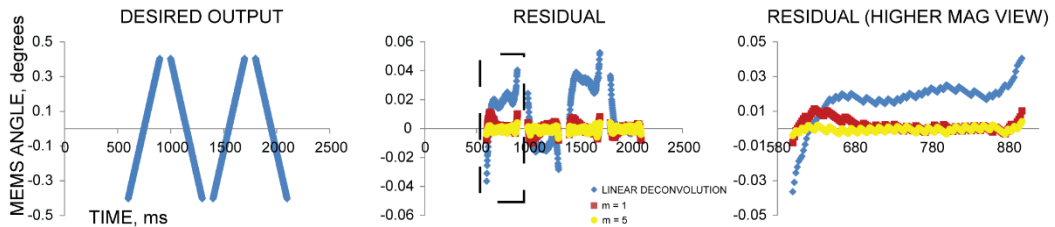


Figure 4.7 Response of the MEMS mirror after using iterative, measurement-based deconvolution

Figure 4.7: The response of the mirror converges to the desired scan pattern (left) by iteratively measuring and incorporating the residual (difference between the desired and achieved pattern) into the deconvolution method. The residual in constrained scan regions is used to compute a set of correction voltages that will cancel out the remaining residual. These correction voltages, produced by deconvolution after each measurement cycle, eventually lower the residual (middle, right) to within 1% of the desired result. Shown is a scan pattern with  $300 \mu\text{s}$  /sweep and  $100 \mu\text{s}$  /turnaround, with linear deconvolution (blue diamond),  $m = 1$  iteration (red square) and  $m = 5$  iterations (yellow circle).

### 4.3.3 Point-scanning Microscopy Application

To demonstrate the value of our waveform optimization method for point scanning fluorescence imaging, we used the test rig described in Figure 4.2. We performed raster scanning using both a naïve waveform and a waveform optimized using our measurement-based deconvolution method (Figure 4.8). In both cases, the raster pattern was made up of 111 lines scanned at a speed of 600  $\mu\text{s}$  per line with 300  $\mu\text{s}$  turnaround. During the turnaround time, the slow axis line shift of the raster pattern is performed. For the optimized waveform, the optimization was performed by constraining both dimensions during the scan and leaving both unconstrained during the turnaround. This pattern enabled image collection at just under 10 Hz. We collected images of several test samples, including a plastic fluorescent slide (Figure 4.8, left column), mixed pollen grains (Figure 4.8, middle column, Carolina 30-4264), and submandibular gland (Figure 4.8, right column, Carolina 31-4932), to compare the image quality obtained with each waveform. The naïve results in the top row show intensity variation across the scan, especially in the center and along the vertical edges. Because the naïve waveform does not incorporate the impulse response of the MEMS mirror, the MEMS mirror does not scan the illumination at a uniform speed. We thus attribute the high intensity vertical line areas in the top row images to higher illumination dwell times arising from the inconsistent scan speed. Additional artifacts produced by the naïve waveform include “lininess” at the image edges and warping of the edges. The optimized waveform removes these artifacts, restoring image quality across the whole field of view for each sample. Note that scan errors only affect the uniformity of illumination for our simple point-scanning microscope, but

for a confocal microscope (especially rescan confocal [71]), the scan errors shown in the top row would cause substantial distortion in both the apparent brightness and apparent position of fluorophores in the sample.

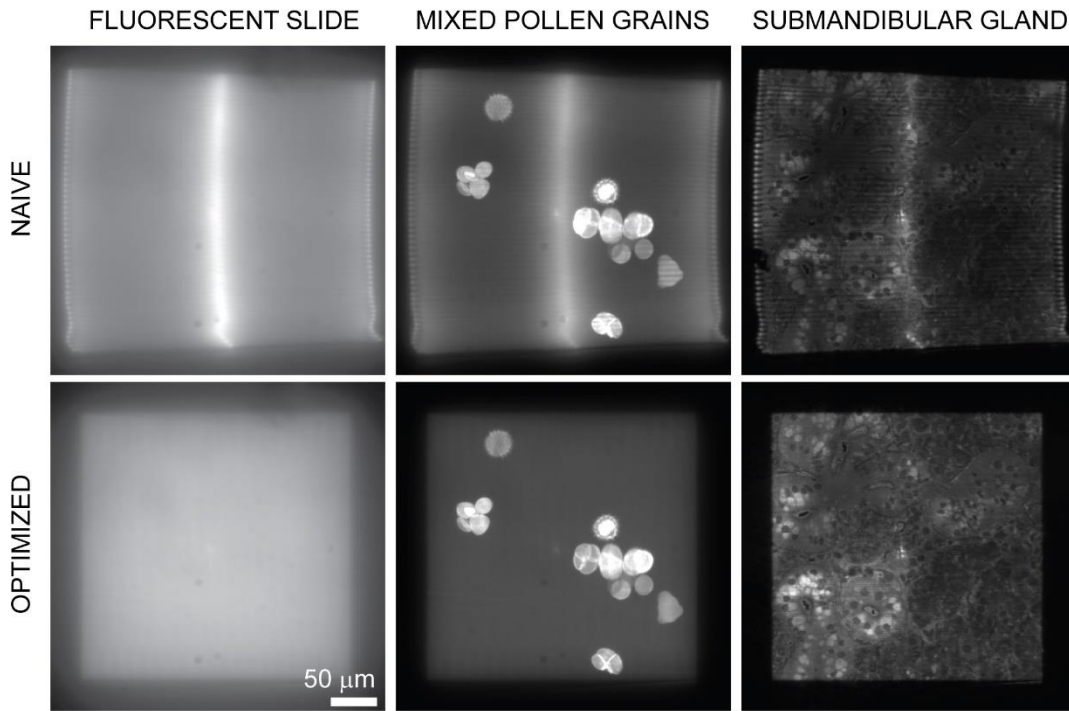


Figure 4.8 Optimized illumination scanning improves fluorescence image quality

Figure 4.8: Images of a plastic fluorescence slide (left column), mixed pollen grains (middle column), and submandibular gland (right column) were acquired by scanning the excitation focus across the field of view in a raster pattern and recording the fluorescence on a camera. Results obtained with a naïve raster waveform (top row) are compared to the optimized waveform (bottom row). The naïve results show pronounced intensity variation across the scan (especially obvious when comparing the middle of each scan to the periphery), warping of the overall raster pattern, and obvious “lininess” within each imaging field. These artifacts are corrected when using the optimized waveform.

#### 4.4 Discussion and Conclusions

We present a novel waveform optimization algorithm for improved MEMS mirror control. While at slow scan speeds, (8 ms/sweep, 1.6 ms/turnaround, Figure 4.3a), approximating the mirror’s impulse response with a delta function produced

fairly accurate results (<4% peak error), a different control method is necessary for faster and more accurate scanning. Our algorithm incorporates the mirror's impulse response and uses Landweber-based deconvolution to generate input voltages waveforms that correctly produce the desired output. By iteratively applying the algorithm and incorporating measurements of the resulting scan pattern, residual errors for much faster scan speeds of 300  $\mu\text{s}/\text{sweep}$  and 100  $\mu\text{s}/\text{turnaround}$  (Figure 4.7) can be corrected to less than 1% of the desired result. This represents a 24x speed improvement while also improving peak error from <4% to <1%. Although the optimization process is currently time-consuming, it only has to be performed once, unless the hardware changes. The optimized waveforms generated have been observed to be stable and accurate over many months, so they are ideal for use in a biological microscope. As we demonstrate, the algorithm enables accurate image formation at high speed, avoiding serious artifacts that would result if input voltages were applied without the algorithm (Figure 4.8).

We envision many applications of our approach beyond the MEMS based raster image scanning we demonstrate. In future work, we hope to show its applicability in rescan microscopy [71] to increase speed while maintaining high accuracy. Our iterative control feedback algorithm can also be applied to non-MEMS hardware, essentially any repeatable, nearly-linear system with a measurable impulse response. We have, for example, explored using the algorithm to increase the scan capabilities of a piezoelectric actuator plate. Future improvements could improve the algorithm's speed and accuracy. Measuring the mirror's response to input voltage waveforms currently accounts for approximately 83% of the total optimization time,

while computation accounts for the remaining 17%. Computation time could be marginally improved with more computing power, but the strobe-based characterization system we use, while accurate and comprehensive, is currently rate limiting. While it is possible to use strobe-based characterization more sparsely and interpolate missing results, this lowers the accuracy of the measurements. A more efficient scheme, such as one that strobos multiple times per measurement or incorporates illumination intensity variation, would enable an accurate system characterization with fewer measurements. Fast, reliable position sensing for MEMS mirrors could be combined with our algorithm to effectively eliminate the rate-limiting measurement of the system's response. In this scenario, our algorithm would function as an alternative to PID control.

## Chapter 5 Single-shot Super-resolution Total Internal Reflection Fluorescence Microscopy

The following chapter is adapted from Guo et al. (2018) [123]. John Giannini designed and built the optical systems with help from Min Guo and Hari Shroff. Min Guo and others acquired and analyzed data. Min Guo and Hari Shroff composed manuscript. Supplementary Figures can be found in Appendix A2. Additional supplementary materials (videos, tables, notes) can be found online at: <https://www.nature.com/articles/s41592-018-0004-4#ref-CR4>.

### 5.1 Introduction

Total internal reflection fluorescence microscopy (TIRFM) [124] provides unparalleled optical sectioning, exploiting an evanescent field induced at the boundary between high and low refractive index media to selectively excite fluorophores within one wavelength of the coverslip surface. The superb background rejection, low phototoxicity, high speed, and sensitivity of TIRFM has been used to study diverse biological phenomena at the plasma membrane, including endocytosis, exocytosis, and focal adhesion dynamics. TIRFM has also been combined with super-resolution methods, particularly SIM [73], [125]–[127] to enable subdiffraction imaging in living cells [73], [128]. Unfortunately, all previous methods sacrifice temporal resolution to improve spatial resolution, limiting their effectiveness in studying dynamic phenomena.

We and others have developed SIM implementations that improve spatial resolution without compromising speed [70], [71], [129]. These microscopes sharpen the image ‘instantly’ (i.e. during image formation) by optically combining information from excitation- and emission- point-spread functions (PSFs), eliminating the need to acquire and process extra diffraction-limited images that

slows classic SIM. Our previous iSIM design [70], [130] modified a swept field confocal geometry, scanning an array of sharp excitation foci to elicit fluorescence, de-scanning the fluorescence, rejecting out-of-focus fluorescence with a pinhole array, and locally contracting each focus before rescanning to produce a super-resolution image.

## 5.2 Results

TIRFM requires highly inclined illumination impinging upon the boundary between media with different refractive indices. We reasoned that placing an annular mask at a Fourier image plane (optically conjugate to the objective back focal plane) would block all subcritical rays, enabling TIRFM without otherwise perturbing the speed and functionality of our original iSIM. Annular illumination has been used to generate a single spot in diffraction-limited [131] and stimulated emission depletion TIRFM [132], yet for parallelized iSIM an array of spots is needed.

We created such a pattern by carefully positioning an annulus one focal length away from the foci produced by our excitation microlens array, simultaneously filtering out low angle rays in each excitation focus. The resulting beams were relayed to the sample by iSIM optical components, including a 1.7 numerical aperture (NA) objective lens used for the large range of critical angles, facilitating TIRFM. Emission optics were nearly identical to the original iSIM setup (Methods, A2 Supplementary Fig. 1).

Since annular excitation produces a focused spot with pronounced sidelobes, we were concerned that interference between neighboring foci and transfer of energy from the central intensity maxima to the sidelobes would significantly diminish

illumination contrast in the focal plane (Supplementary Note 1). When imaging fluorescent dye in TIRFM, we did observe substantial background fluorescence between excitation foci. However, individual foci were sharply defined and the extraneous background could be readily removed with the pinhole array intrinsic to our setup (A2 Supplementary Fig. 2). We confirmed that TIRF was maintained during the imaging process by measuring the depth of the evanescent field with silica beads (A2 Supplementary Fig. 3), finding this value to be 123 nm  $\pm$  6 nm (95% confidence interval). Imaging fixed microtubule samples also demonstrated the improved sectioning characteristic of TIRFM, as microtubules that were otherwise visible disappeared under TIRFM illumination (A2 Supplementary Fig. 4-7).

We estimated system resolution on 100 nm fluorescent beads (A2 Supplementary Fig. 8). In diffraction-limited TIRFM (removing the pinholes and emission microlenses from our setup) beads were resolved to 249  $\pm$  11 nm (N = 20 beads, mean  $\pm$  standard deviation). Descanning, pinholing, locally contracting, and rescanning reduced the apparent bead diameter to 194  $\pm$  20 nm, and resolution was further improved after deconvolution (10 iterations, Richardson-Lucy deconvolution) to 115  $\pm$  13 nm. We observed similar results in iSIM using the same objective lens (Supplementary Table 1), implying that spatial resolution did not degrade with TIRF. Images of fixed cells confirmed this progressive resolution improvement (Figure 5.1a-c), as individual microtubules had an apparent width of  $\sim$ 125 nm in instant TIRF-SIM (Figure 5.1a, 5.1d), and we were able to distinguish microtubules spaced 134 nm apart, otherwise unresolved in TIRFM (Figure 5.1c, e). We further verified our enhanced spatial resolution by resolving fluorophores spaced 120 nm apart in

DNA nanorulers (Figure 5.1f) and in live cells observing individual GFP-labeled myosin IIA bipolar filaments [133] and void areas within GFP-FCHO2 puncta [134] (A2 Supplementary Fig. 9), subdiffractive structural features that have previously been resolved with TIRF-SIM.

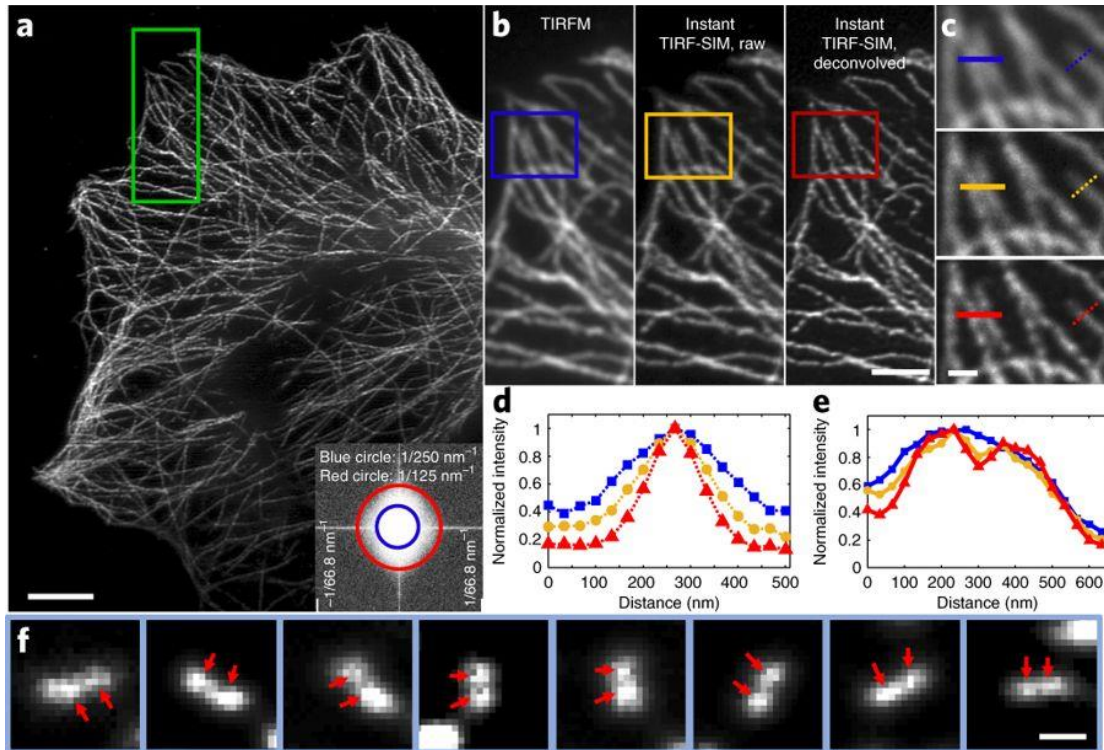


Figure 5.1 Resolution enhancement via instant TIRF-SIM

Figure 5.1: a) Deconvolved instant TIRF-SIM image of immunolabeled microtubules in a fixed U2OS cell. Inset shows power spectrum of data, on a logarithmic intensity scale. Circles indicating the diffraction limit (blue) and 125 nm spatial resolution (red) are also shown. b) Higher magnification views of the green rectangular region in a) showing diffraction-limited TIRFM (obtained using only the excitation microlenses, left), instant TIRF-SIM (raw data after employing pinholes and emission microlenses, middle), and deconvolved instant TIRF-SIM (right). c) Higher magnification views of diffraction-limited TIRFM (top), raw instant TIRF-SIM (middle) and deconvolved instant TIRF-SIM images, corresponding to blue, yellow, and red rectangular regions in b). Comparative line profiles (d, dashed lines in c; e, solid lines in c) are also shown. f) Examples of 120 nm DNA nanoruler resolution targets, imaged in instant TIRF-SIM. Red arrows indicate lobes on each dumbbell. All data are delined (A2 Supplementary Fig. 5) except left and middle columns in b) and top and middle rows in c). Scale bars:

5  $\mu\text{m}$  in a, 2  $\mu\text{m}$  in b, 0.5  $\mu\text{m}$  in c, 250 nm in f. Experiments were repeated at least 4 times with similar results; representative data are shown.

We next used instant TIRF-SIM to examine the dynamics of protein distributions in living cells (Figure 5.2). First, we recorded microtubule dynamics over 500 time-points by imaging the fluorescence microtubule binding probe, EMTB-3xEGFP [135], [136], in Jurkat T cells after they settled on anti-CD3 coated coverslips (Figure 5.2a, Supplementary Video 1). Our imaging rate of 20 Hz was sufficient to easily follow buckling, shortening, and sliding of microtubule bundles at the base of the cell within the evanescent field (Figure 5.2b). As a second example, we recorded the dynamics of the small GTPase HRas, which is lipidated and then targeted to the plasma membrane [137]. Images were acquired every 0.75 s over 60 timepoints in U2OS cells (Figure 5.2c, Supplementary Video 2). Intriguingly, GFP-HRas localized in highly dynamic microdomains at the plasma membrane (Figure 5.2c, d, Supplementary Video 3). The high spatiotemporal resolution of our technique revealed rich dynamics of this reticulated pattern, as we observed reorganization of domains on the second timescale, including transient ‘filling in’ of the void areas between microdomains (Figure 5.2d), and coordinated, ‘wave-like’ motion between microdomains (Supplementary Video 3). To our knowledge, neither the distribution nor the dynamics of Ras has been reported at this length scale in living cells, perhaps due to the lack of spatial resolution or optical sectioning (we found that in diffraction-limited TIRFM, microdomains were poorly resolved, A2 Supplementary Fig. 10a ,b).

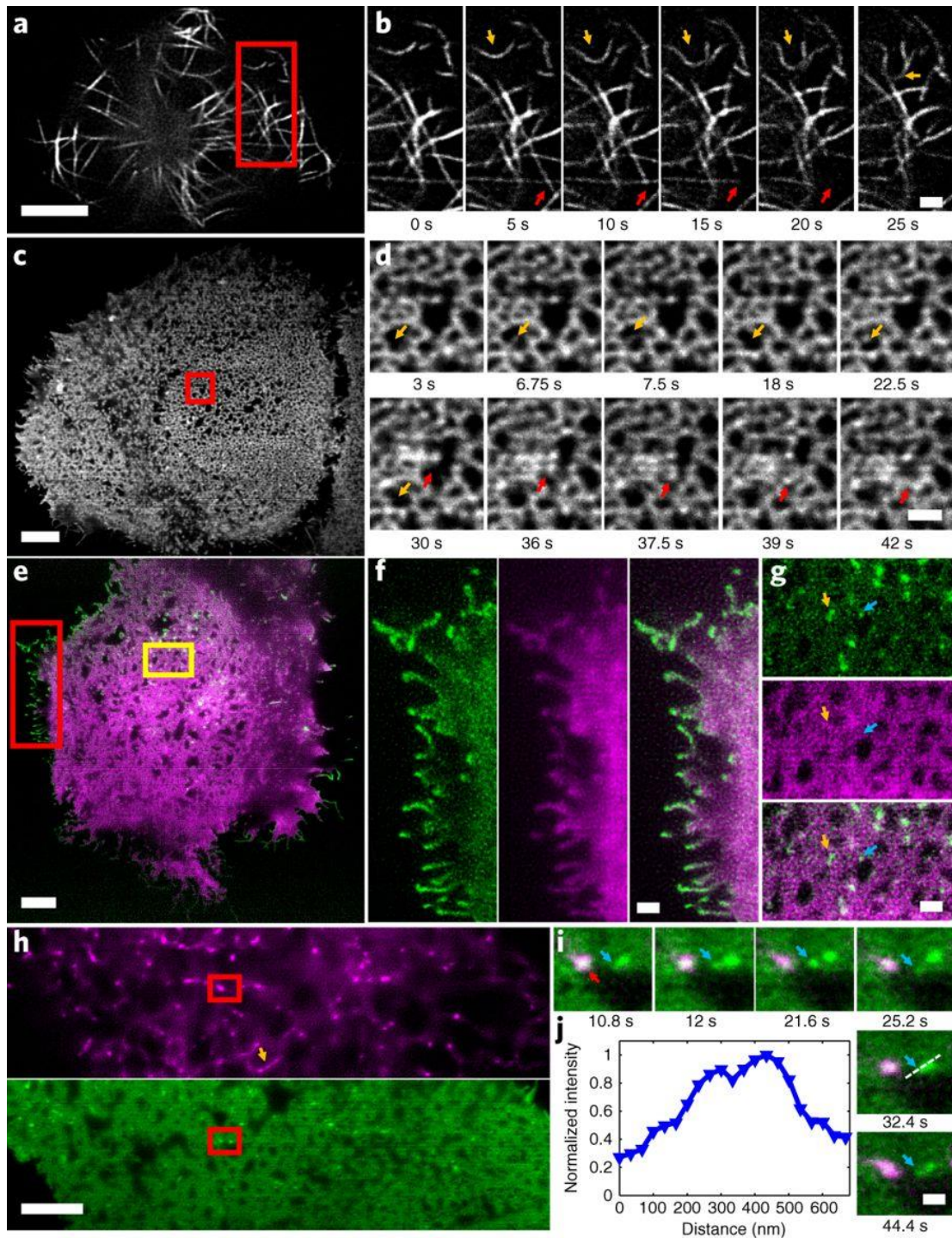


Figure 5.2 Instant TIRF-SIM enables high speed super-resolution imaging at the plasma membrane over hundreds of time points

Figure 5.2: a) Image of EMTB-3xEGFP expressed in Jurkat T cells, taken from 500 frame series (images recorded every 50 ms). Higher magnification series b) of red rectangular region in a highlights microtubule buckling (orange arrows) and movement (red arrows mark microtubule bundle that moves left and up during image series). See

also Supplementary Video 1. c) Image of EGFP-HRAS expressed in U2OS cell, taken from series spanning 60 time points, images recorded every 0.75 s. d) Higher magnification view of red rectangular region in c) emphasizing dynamics, including transient filling in (orange arrows) and reorganization (red arrows) of microdomains. See also Supplementary Videos 2, 3. e) Two-color image showing EGFP-VSVG (green) and Halotag-Ras (labeled with Janelia Fluor 546, magenta), derived from series spanning 100 time points, dual-color images recorded every 2.3 s. f) Higher magnification view of red rectangular region in e), showing EGFP-VSVG (left), Halotag-Ras (middle) and merged (right) distributions, highlighting concentrated VSVG at cell periphery. g) Higher magnification view of orange rectangular region in e), showing EGFP-VSVG (top), Halotag-Ras (middle) and merge (bottom). Arrows mark VSVG puncta located near Ras microdomains. See also Supplementary Video 4. h) Two-color image showing pDsRed2 ER (magenta, top) and EGFP-HRas (green, bottom), derived from image series spanning 100 time points, images recorded every 1.2 s. Orange arrow highlights ER tubule. i) Higher magnification series of red rectangular region in h, highlighting dynamics of Ras puncta (blue arrow) in vicinity of ER contact site (red arrow). j) profile of dashed line in i indicating peak-to-peak separation of 134 nm in HRas channel. See also Supplementary Video 5, 6. Scale bars: 5  $\mu\text{m}$  in a, c, e, h; 1  $\mu\text{m}$  in b, d, f, g; 500 nm in i. Experiments were repeated at least 4 times with similar results; representative data are shown.

We also imaged Halotag-HRas (labeled with Janelia Fluor 549 [138]) with GFP-tagged vesicular stomatitis virus G protein (VSVG [139], Figure 5.2e, Supplementary Video 4), highlighting the ability of instant TIRF-SIM for dual-color imaging. Despite similar targeting to the plasma membrane [140], GFP-VSVG and Halotag-HRas displayed distinct localization within living cells (Figure 5.2g). VSVG showed some localization around Ras microdomains within the cell interior (Figure 5.2g) and preferential enrichment at the cell boundary, particularly at cell filopodia and filamentous structures. In another example, we imaged GFP-HRas with pDsRed2-ER (Figure 5.2h), which marks endoplasmic reticulum (ER). The ER mostly appeared as a set of bright punctate spots and occasional tubules near the plasma membrane, while the rest of the ER appeared as a network structure presumably further from the coverslip. Although punctate ER structures occasionally colocalized with Ras, the protein distributions were mostly distinct and exhibited

different dynamics (Supplementary Video 5), consistent with their differential localization and function within the cell. The spatial resolution of our technique proved key in resolving apparent fission and fusion of Ras microclusters adjacent to more stable ER contacts (Figure 5.2i), a phenomenon otherwise obscured by diffraction (Figure 5.2j, A2 Supplementary Fig. 10c, d, 11, Supplementary Video 6). Additional recordings of intracellular calcium flux, actin, and myosin IIB dynamics (Supplementary Videos 7-10) underscored our ability to perform super-resolution imaging well matched to the dynamics of interest, either matching or surpassing the image acquisition rate offered by more traditional TIRF-SIM systems (Supplementary Table 2).

A key advantage in iSIM is the ability to image at much faster frame rates. To illustrate this capability, we imaged GFP tagged Rab11, a recycling-endosome specific GTPase that drives constant turnover of endosomes from the plasma membrane to the cytosol and modulates extracellular release of vesicles [141], in U2OS cells at 37°C at 100 Hz (Supplementary Video 11). This imaging rate was sufficient to visualize and track [142] the rapid motion of 1713 Rab11-decorated particles (Figure 5.3a). An analysis of track motion revealed that most particles underwent  $< 1 \mu\text{m}$  displacement over our 6 s imaging period, yet we also observed tens of particles that showed greater displacements, with mean speed greater than  $1 \mu\text{m/s}$  (Figure 5.3b, c, A2 Supplementary Fig. 12) and with instantaneous speed in some cases exceeding  $10 \mu\text{m/s}$  (Figure 5.3d, f). A closer analysis at the single particle level (Figure 5.3b, c) also revealed qualitative differences in particle motion, with some particles undergoing diffusive motion, as revealed by a linear mean square

displacement (MSD) vs. time and others showing supralinear MSD vs. time (Figure 5.3e) with bouts of directed motion (Figure 5.3d, Supplementary Video 12, 13).

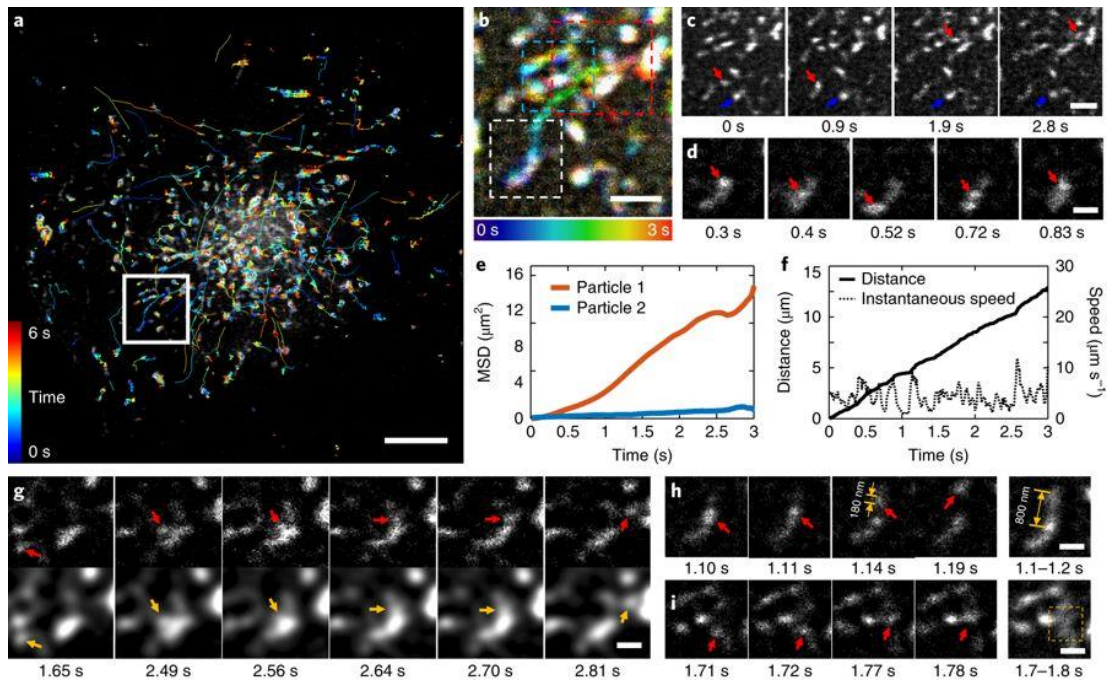


Figure 5.3 Rapid dynamics of Rab11 are resolved at 100 Hz with instant TIRF-SIM. EGFP-Rab11 was transfected into U2OS cells and imaged at 37°C at 100 Hz

Figure 5.3: a) First frame from image series, with overlaid tracks (lines colored to indicate time, color bar indicated at left). b) Higher magnification view of white rectangular region in a), over the first 3 seconds of acquisition. Time evolution indicated in color bar at bottom. c) Selected images corresponding to region in b), emphasizing motile (red arrow) and more stationary (blue arrow) particle. d) Magnified view of more motile particle indicated with red arrow in c) (white dashed rectangular region in b) highlighting bidirectional motion. Mean square displacements of both particles (e) and distance and instantaneous speed (f) of the motile particle are also quantified. g) Selected images corresponding to red dashed rectangular region in b). Particle, highlighted by arrows, is resolved in instant TIRF-SIM (top row) but poorly or not (yellow arrows) resolved in spatially blurred images (bottom row) that simulate diffraction-limited TIRFM. h) Selected images corresponding to white dashed rectangular region in b), demonstrating that recording at fast 5 ms exposures resolves particles (red arrows), but combining frames into 100 ms bins does not (particle of size ~180 nm is blurred into extended structure of length ~800 nm) i) Same analysis as in h) (compare particle indicated by red arrows in left images to yellow dashed region in right-hand image), but particle and region correspond to cyan dashed region in b). Scale bars: 5  $\mu\text{m}$  in a; 1  $\mu\text{m}$  in b, c; 0.5  $\mu\text{m}$  in d, g, h, i. See also A2 Supplementary Fig. 12, 13 and Supplementary Videos 11-14. Experiments were repeated at least 4 times with similar results; representative data are shown.

Imaging at slower frame rates (as with previous implementations of TIRF-SIM) distorts track lengths because long tracks are broken into shorter tracks, short tracks are discarded, and multiple independent short tracks may be classified falsely as longer tracks (A2 Supplementary Fig. 13a, b). Imaging at lower spatial resolution (as in diffraction-limited TIRFM) failed to resolve particles in densely packed regions of the cell (Figure 5.3g, Supplementary Video 14) or missed hundreds of tracks (A2 Supplementary Fig. 13c, d).

If the sample moves on a length-scale comparable to or greater than the resolution limit in a single exposure, motion blur degrades spatial resolution and introduces artifacts (A2 Supplementary Fig. 14, Supplementary Videos 15,16). For example, when binning frames together to simulate the slower exposures afforded by traditional TIRF-SIM, Rab11 particles that were otherwise resolved formed artificial structures larger than the diffraction limit (Figure 5.3h, i). To further illustrate this point, we imaged Rab11 on a state-of-the-art TIRF-SIM. While this instrument could not match the 100 Hz frame rate of our system, we were able to acquire raw images at an exposure time identical to our instrument (5 ms), resulting in a frame rate of 12.9 Hz. Rab11 particles were sharply defined in raw diffraction-limited images, but the time delay introduced by the need to acquire nine such images for a single reconstructed frame resulted in obvious artifacts (Supplementary Videos 17, 18, A2 Supplementary Fig. 15), worsening spatial resolution to the extent that images were no longer even diffraction-limited.

### 5.3 Discussion

Such artifacts were absent in instant TIRF-SIM, which is fundamentally faster than traditional TIRF-SIM, as only one image needs to be acquired, instead of the standard nine [73]. Related advantages of our method over previous approaches include less read noise and less computational processing. Although our ~115 nm spatial resolution is worse than claimed in state-of-the-art linear TIRF-SIM [128, p.] (84 nm), our existing implementation of instant TIRF-SIM is ~50 fold faster.

Room for technical improvement remains. The excitation efficiency of our setup is low, as ~60% of the illumination is blocked by the annular mask. Using a spatial light modulator (SLM) to generate the pattern might direct the illumination through the annular mask more effectively, facilitating lower power illumination. Controlling the phase of the illumination might also reduce the sidelobes in each focus, improving contrast in the focal plane and perhaps even removing the need for pinholes (although pinholes are still useful in reducing scattered light that continues to contaminate objective-based TIRF [143]). Using optics that allow rapid adjustment of the annulus dimensions (such as an SLM or a digital micromirror device) could facilitate adjustment of the evanescent field depth, providing additional axial information within the TIRF zone [144]. Finally, we did not exploit the narrower central maximum in each excitation focus for (marginally) higher spatial resolution, due to the coupling between inter-focus distance and focus size (Supplementary Note 1). Combining TIRFM with single-point rescanning SIM [71], [145] would address this issue, albeit at the cost of temporal resolution.

## 5.4 Methods

### 5.4.1 Instant TIRF-SIM

The instant TIRF-SIM is built directly upon our previously reported instant SIM system [70], but with two important modifications in the excitation path. First, we used a 1.7 NA objective (Olympus, APON100XHOTIRF) for excitation and detection. When imaging into aqueous samples with refractive index 1.33,  $1 - (1.33/1.7) = 0.22$  of the objective back focal plane diameter ( $d_{\text{BFP}}$ ) is available for TIRF, implying that sub-critical illumination rays within a diameter  $0.78 * d_{\text{BFP}} = 0.78 * 2 * \text{NA}_{\text{OBJ}} * f_{\text{OBJ}} = 0.78 * 2 * 1.7 * 1.8 \text{ mm} = 4.77 \text{ mm}$  must be blocked. Second, we inserted a relay system into the excitation arm of the instant SIM to block these rays. Excitation from 488 nm and 561 nm lasers was combined and beam expanded as before, and directed to a microlens array (Amus,  $f = 6 \text{ mm}$ ,  $222 \mu\text{m}$  spacing between microlenses, 1 mm thick, 25 mm diameter, antireflection coated over 400–650 nm, APO-Q-P222-F6(633)+CHR) to produce an array of excitation foci. We used a matched pair of scan lenses (Scan lens 1 and 2,  $f=190 \text{ mm}$ , Special Optics, 55-S190-60-VIS) placed in  $4f$  configuration to relay these excitation foci to the rest of the optical system, inserting an opaque circular mask (Photosciences, 2.68 mm diameter chrome circle with optical density 5 on 4" x 4" x 0.090" quartz wafer) at the focal point between scan lenses (and the Fourier plane of the excitation foci produced by the microlens array) to filter subcritical rays. Given the  $350 \text{ mm} / 190 \text{ mm} = 1.84x$  magnification between the mask and the back focal plane of the objective, we designed the mask to block the central  $2.68 \text{ mm} * 1.84 = 4.93 \text{ mm}$  diameter of the illumination. An iris placed just after the mask ensured that the outer diameter of the

beam was  $\sim 3.33$  mm, a diameter that magnified to  $3.33 * 1.84 = 6.13$  mm, or  $\sim d_{\text{BFP}}$ , thereby reducing stray light that would otherwise fall outside the objective back focal plane. Alignment of the opaque mask and microlens array, which is critical, was greatly aided by placing the former on a 3-axis translation stage (Thorlabs, LT3, used for correct positioning of the mask image at the back focal plane) and the latter on a uniaxial translation stage (Thorlabs, LNR50M, used to position excitation foci precisely at the focal plane of the objective lens). We also used an alignment reticle (Leica) that screwed into our objective turret to further check that the annular illumination pattern was properly positioned (concentric with the optical axis of the objective) and focused at the back focal plane of our objective. In the emission path, optics were identical to our previous design, except that we used a pinhole array with larger pinholes (Photosciences, Chrome on 0.090" thick quartz, 222  $\mu\text{m}$  pinhole spacing, 50  $\mu\text{m}$  pinhole diameter) and an emission-side microlens array with longer focal length ( $f = 1.86$  mm, Amus, APO-Q- P222-F1.86(633)). The total magnification between sample and our scientific grade complementary metal-oxide semiconductor camera (PCO-TECH, pco.edge 4.2) detector was  $350 \text{ mm} / 1.8 \text{ mm} = 194.4$ , resulting in an image pixel size of 33.4 nm. These elements are shown in A2 Supplementary Fig. 1.

The excitation laser power was measured immediately prior to the objective. Depending on the sample, the average power ranged from 0.2 - 2 mW, implying an intensity range from  $\sim 7 - 70 \text{ W/cm}^2$  (given our  $58 \mu\text{m} \times 52 \mu\text{m}$  field of view).

Samples were deposited on 20 mm diameter high index coverslips (Olympus, 9-U992) designed for use with the 1.7 NA lens. Coverslips were mounted in a

magnetic chamber (Live Cell Instrument, CM-B20-1) that attached to the microscope stage. For temperature maintenance at 37 °C, the magnetic chamber was mounted within an incubation chamber (Okolab, H301-MINI).

#### 5.4.2 Estimating the evanescent field depth

We used two methods to estimate evanescent field depth. First, we used an analytical method [146]. For excitation of wavelength  $\lambda$  impinging at angle  $\theta_1$  upon an interface with indices  $n_1$  and  $n_2$ ,  $n_1 > n_2$ , the intensity  $I$  of an evanescent field decays along the optical axis with decay constant  $d$  according to  $I(z) = I_0 \exp(-z/d)$ , with  $d = \lambda / (4\pi) (n_1^2 \sin^2(\theta_1) - n_2^2)^{-0.5}$ . The term  $n_1^2 \sin^2(\theta_1)$  is equivalent to the square of an “effective” NA, in our case  $\leq 1.7$ . If considering the smallest angles in our annular excitation (corresponding to the inner radius used in the mask, producing evanescent waves with the longest decay length), this effective NA is  $4.93/6.12 * NA_{OBJ} = 1.37$ . Assuming  $n_2 = 1.33$  and  $\lambda = 488$  nm leads to  $d = 118$  nm. If considering the largest angles (corresponding to the outer annulus radius, producing evanescent waves with the shortest decay length), the effective NA is  $NA_{OBJ} = 1.7$ , leading to  $d = 37$  nm. By these simple calculations, the “average” decay thus lies between 37 nm – 118 nm, weighted by the distribution of intensity in the annular excitation.

Since such an intensity distribution is difficult to measure accurately, we instead opted to measure the average evanescent decay length more directly using silica beads (diameter 7.27  $\mu\text{m}$ , refractive index, 1.42, Bangs Laboratories) placed in a solution of fluorescein dye (Fluka, Cat #32615) (A2 Supplementary Fig. 3a). In this method, the known diameter of the bead is used to convert the apparent radii observed with TIRF to an axial depth [146],  $z$  (A2 Supplementary Fig. 3b). Following

previous work [147], we integrate the intensity  $I(z)$  from the coverslip surface to some depth  $z$ , as this corresponds to the observed signal  $F(z)$  at each depth. First, we assume the fluorescence is well modeled by a sum of two exponentials. The first term corresponds to signal derived from “pure” TIRF (with decay  $d$ ) and the second term models scattering that is known to contaminate objective-type TIRF (with decay  $D$ ):

$$I(z) = A\exp(-z/d) + B\exp(-z/D),$$

where  $A$  and  $B$  are constants that account for incident beam intensity, concentration, and the relative weight of the scattering term. Integrating this expression yields

$$F(z) = Ad(1-\exp(-z/d)) + BD(1-\exp(-z/D)).$$

Fitting the measured fluorescence intensity at each depth (derived at each bead radius) to this expression (A2 Supplementary Fig. 3c) with the MATLAB curve fitting toolbox gave  $d = 123$  nm with 95% confidence interval (117nm, 129 nm). The scattering amplitude  $B$  represented ~24 % of the signal.

#### 5.4.3 Diffraction-limited TIRF comparisons

For some comparisons (Figure 5.1b, c, A2 Supplementary Fig. 8, 10a, b, 13c, d), the sample was imaged with instant TIRF-SIM and then again after removing pinholes and emission microlenses, yielding a diffraction-limited image. In other cases (Figure 5.3g, A2 Supplementary Fig. 10c, d, 14), we simulated this effect (A2 Supplementary Fig. 11) by blurring the deconvolved instant-SIM data with a 2D Gaussian function of  $\sigma = (\sigma_{\text{DIFFRACTION-LIMITED}}^2 - \sigma_{\text{INSTANT TIRF-SIM}}^2)^{0.5}$  where  $\sigma_{\text{INSTANT TIRF-SIM}}$  is derived from the apparent width of beads measured in the instant TIRF-SIM after deconvolution (=115 nm/2.355) and  $\sigma_{\text{DIFFRACTION-LIMITED}}$  is the corresponding diffraction-limited value (=249 nm/2.355).

#### 5.4.4 Comparisons with commercial TIRF-SIM

Data were collected using a DeltaVision OMX SR microscope (GE Healthcare Life Sciences) equipped with a 60x NA1.42 objective (Olympus). Samples were maintained at 37C with the environmental chamber housed within the microscope. The exposure time for each raw diffraction-limited frame was set to 5 ms, resulting in a total acquisition time of 77.8 ms for each 9-frame grouping. Data were processed with OMX software to yield SIM reconstructions.

#### 5.4.5 Flat Fielding

Due to the spatially nonuniform profile of the excitation laser beam, the excitation intensity is not distributed uniformly even when the excitation is scanned. The scanned excitation distribution has highest intensity in the center of the field of view and diminishes at increasing distances perpendicular to the scanning direction. To normalize for this variation in excitation intensity ('flat fielding'), we averaged 100 images of a thin fluorescein layer, smoothed the average perpendicular to the scan direction, and divided the raw data by this smoothed average prior to deconvolution. All datasets shown in the paper were flat-fielded before display (Supplementary Software).

#### 5.4.6 Deconvolution

Unless otherwise indicated, data presented in this paper were deconvolved to further enhance spatial resolution. Before deconvolution, background was subtracted from the raw images. Background was estimated by averaging 100 "dark" images

acquired without illumination. For deconvolution, we used the Richardson-Lucy algorithm [148], [149], blurring with a 2D PSF:

For  $k = 1, 2, \dots, N$

$$Estimate_{k+1} = Estimate_k \times \left( \frac{Image_{Measured}}{Estimate_k \otimes PSF} \otimes \widetilde{PSF} \right)$$

where  $\otimes$  denotes convolution operation,  $Image_{Measured}$  is the measured image (after background subtraction) and  $\widetilde{PSF}$  is the flipped PSF:

$$\widetilde{PSF}(i, j) = PSF(m - i, n - j), 0 \leq i < m, 0 \leq j < n$$

with  $m, n$  the PSF dimensions.

The PSF was experimentally derived by registering and then averaging the images of 20 100 nm yellow-green beads. Deconvolution was implemented in MATLAB 2017a with the number of iterations  $N$  set to 10 (Supplementary Software).

#### 5.4.7 Bleach Correction

For several time-lapse datasets (Figure 5.2c-i, 5.3, A2 Supplementary Fig. 10c, d, 12-15, Supplementary Video 1-6, 11-18, we performed standard bleaching correction using an ImageJ Plugin (Bleach Correction [150], [https://imagej.net/Bleach\\_Correction](https://imagej.net/Bleach_Correction)) with the “simple ratio” method.

#### 5.4.8 Delining Data

Close inspection of the data acquired in our instant TIRF-SIM revealed a horizontal line artifact that arises because the instant SIM performs a 1D scan of a 2D space with a 2D grid of illumination points [70]. This problem is slightly exacerbated under TIRF illumination due to the smaller foci size (Supplementary Note 1, Supplementary Software). However, we found that the lines showed repeatable

signatures in Fourier space and that by applying notch filters at these locations we could suppress line artifacts in our images (A2 Supplementary Fig. 5-7, Methods).

More specifically, Fourier transforming the image data and displaying the power spectrum revealed high intensity puncta along the vertical axis. These puncta correspond to horizontal line artifacts in our data, as discussed in the main text. Replacing these high-intensity pixels with zero valued pixels and taking the inverse Fourier transform suppressed the lines without compromising spatial resolution (A2 Supplementary Fig. 5). As 10 rectangular regions, each 20x20 pixels, were zeroed in each 2048x2048 Fourier transform, delining affected less than  $< 0.1\%$  of the total power spectrum in each image.

A similar strategy was proposed to reduce artifacts that continue to plague more traditional SIM implementations [151]. All data shown in this paper, unless otherwise noted, was ‘delined’ using this procedure.

#### 5.4.9 Drift Correction

Some datasets (Supplementary Video 1, 3) were corrected for drift using the ‘StackReg’ plugin in ImageJ [152] (<https://imagej.net/StackReg>), using the ‘Rigid Body’ condition.

#### 5.4.10 Image Display

All images are displayed in grayscale, except images in Figure 5.2 e-i, displayed in green and/or magenta colormaps from ImageJ, and A2 Supplementary Fig. 14, displayed using the ‘hot’ colormap in ImageJ.

#### 5.4.11 Tracking

For the Rab11 dataset (Figure 5.3), we performed semi-automated tracking using the TrackMate ImageJ Plugin [153] (<https://imagej.net/TrackMate>). For particle detection, the Difference of Gaussian (DoG) detector was used with estimated spot diameter of 0.25  $\mu\text{m}$ , and an initial quality threshold of 150. The particles were further filtered with a quality threshold of 200 and linked with a simple Linear Assignment Problem (LAP) linker. Linking maximum distance, the gap-closing maximum distance, and the maximum frame gap were set to 0.3  $\mu\text{m}$ , 0.4  $\mu\text{m}$  and 8, respectively. Manual inspection of the data revealed that the vast majority of tracks < 10 frames were spurious, so these were excluded from further analysis. For tracking on the whole image (Figure 5.3), the linking filters were manually adjusted to filter out obviously spurious tracks. Then manual editing was performed within the plugin interface to improve tracking results. Within the cropped region used for downsampling analysis (A2 Supplemental Fig. 13a, b, Supplemental Video 12), images were downsampled 5- and 10 times in the time domain. Then, automated tracking was performed independently for the cropped images (100Hz) and the downsampled images (20 Hz and 10 Hz) without manually adjusting either linking filters or links. Automated tracking parameters were also used in additional Rab11 datasets (A2 Supplemental Fig. 13c, d) except that the initial quality threshold and filtered quality threshold for the spots detection were replaced by 100 and 120, respectively, due to the slightly weaker image intensity.

From the particle tracks (i.e., the sequences of coordinates denoting the position of each tracked particle at each time point), we computed several quantitative

metrics including displacement, distance, instantaneous speed, mean speed and mean squared displacement (MSD).

Given a trajectory consisting of  $N$  time points and the particle coordinates at  $i$ th time point  $\mathbf{p}_i = (x_i, y_i)$ , we define the distance between any two points  $\mathbf{p}_i$  and  $\mathbf{p}_j$  as the Euclidean norm

$$d(\mathbf{p}_i, \mathbf{p}_j) = \|\mathbf{p}_i - \mathbf{p}_j\|$$

The total distance traversed at the  $j$ th time point is calculated from the starting point (the 1st time point) and defined as

$$D_j = \sum_{i=1}^{j-1} d(\mathbf{p}_i, \mathbf{p}_{i+1})$$

and the displacement (magnitude), also known as net distance

$$F_j = d(\mathbf{p}_1, \mathbf{p}_j)$$

Then the total distance for the whole trajectory is  $D_N$  and the total displacement for the whole trajectory is  $F_N$ .

The instantaneous speed is defined as

$$v_i = \frac{d(\mathbf{p}_i, \mathbf{p}_{i+1})}{\Delta t}$$

where  $\Delta t$  is the time interval between two successive time points. The instantaneous speed is also the derivative of the traveled distance  $D_j$ .

Then the mean speed is calculated as the average of the instantaneous speed:

$$\bar{v} = \frac{1}{N-1} \sum_{i=1}^{N-1} v_i$$

The mean squared displacement is calculated as

$$MSD(n) = \frac{1}{N-n} \sum_{i=1}^{N-n} d^2(\mathbf{p}_i, \mathbf{p}_{i+n})$$

#### 5.4.12 Bead Samples

High index coverslips were cleaned with 100% ethanol and coated with 0.1% Poly-L-Lysine (PLL, Sigma-Aldrich) for 10 min. Then 100 nm yellow-green beads (Thermo Fisher Scientific, F8803) were diluted  $\sim 10^5$ -fold and 20  $\mu$ L added to the coverslip. After 10 min, the coverslip was washed four times with clean water before imaging (A2 Supplementary Fig. 8).

#### 5.4.13 DNA Nanorules

High index coverslips were incubated with BSA-biotin solution (1 mg/ml in PBS) for 5 min, washed three times with PBS, incubated with neutravidin solution (1 mg/ml) for 5 min in PBS, and washed three times with PBS containing 10 mM magnesium chloride (IB buffer). 1-2  $\mu$ L 120 nm DNA nanorulers labeled with Alexa Fluor 488 (GATTAquant DNA Nanotechnologies, GATTA-SIM 120B) diluted into 200  $\mu$ L IB were incubated with the coverslip for 5 minutes immediately prior to imaging (Figure 5.1f).

#### 5.4.14 Fixed Samples

For imaging microtubules within fixed samples (Figure 5.1a-c, A2 Supplementary Fig. 4, 5a), high index coverslips were first immersed in 70% ethanol for  $\sim 1$  min and allowed to air dry in a sterile cell culture hood. U2OS cells were grown on uncoated high index coverslips until  $\sim 50\%$  confluency. The entire coverslip was submerged for 3 minutes in methanol pre-chilled to  $-20$   $^{\circ}$ C to fix the cells.

Coverslips were then washed in PBS at room temperature extensively before blocking in antibody dilution buffer (Abdil; 1% BSA, 0.3% Triton-X 100 in PBS) for 1 hour at room temperature. The primary antibody stain was performed overnight at 4 °C using 1/500 mg/ml of mouse anti  $\alpha$ -Tubulin (Thermo Fisher Scientific #62204) in Abdil. The secondary antibody stain was performed for 1-2 hours at room temperature using 1/200 mg/ml of goat anti-mouse Alexa 488 (Invitrogen A11001) in Abdil.

#### 5.4.15 Live Jurkat T Cells

High index coverslips were rinsed with 70% ethanol and dried with filtered air. The coverslips were then incubated in Poly-L-Lysine (PLL) at 0.01% W/V (Sigma Aldrich, St. Louis, MO) for 10 min. PLL solution was aspirated and the coverslip was left to dry for 1 hour at 37 °C. Coverslips were next incubated with streptavidin (Invitrogen) at 2  $\mu$ g/ml for 1 hour at 37 °C and excess streptavidin was washed with PBS. Antibody coating for T cell activation was performed by incubating the coverslips in a 10  $\mu$ g/ml solution of biotin labeled anti-CD3 antibody (OKt3, eBiosciences, San Diego, CA) for 2 hours at 37 °C. Excess antibody was removed by washing with L-15 imaging media immediately prior to the experiment. E6-1 Jurkat T-cells were transiently transfected with EMTB-3xEGFP (Figure 5.2a, b, Supplementary Video 1) or F-tractin EGFP (Supplementary Video 8) plasmid using the Neon (Thermo Fisher Scientific) electroporation system two days before the experiment. Transfected cells were centrifuged and resuspended in L-15 imaging media prior to pipetting them onto the coverslip. Imaging was performed 10 minutes after the cells settled on the substrate. EMTB-3xEGFP was a gift from William

Bement (Addgene plasmid # 26741) and pEGFP-C1 F-tractin EGFP was a gift from Dyche Mullins (Addgene plasmid # 58473).

#### 5.4.16 Live U2OS Cells

Human osteosarcoma U2OS cells were routinely passaged in DMEM (Life technologies) plus 10% FBS (Hyclone) at 37 °C, with 5% CO<sub>2</sub>. For cleaning prior to live cell imaging, high index coverslips were boiled for 5 minutes with distilled water, thoroughly rinsed with distilled water and stored in 90% ethanol for at least 2 hours. To facilitate cell adherence, the coverslips were coated with FBS for 2 hours at 37°C. 24 - 48 hours prior to transfection, cells were plated on cleaned coverslips, at a density of ~60%. Cells were transfected with the appropriate plasmid using Turbofect (Life Technologies) at a ratio of 3:1 (Liposomes:DNA). The next day, the medium was replaced with fresh DMEM plus 10% FBS without phenol red, which was also used as the imaging medium. To monitor wild type Ras dynamics, we used EGFP-HRas (Figure 5.2c, d, A2 Supplementary Fig. 5b, 10a, b, Supplementary Video 2, 3), or if imaged with VSVG-GFP (Addgene #11912) (Figure 5.2e-g, Supplementary Video 4), we used a HaloTag chimera of HRas (gift of Dominic Esposito, NCI). Halotag proteins were labeled using Janelia Fluor549 (gift of Luke Lavis, Janelia Research Campus) at a final concentration of 100 nM for 15 minutes. Following labelling, the cells were rinsed twice with plain DMEM, incubated with fresh medium plus 10% FBS for 20 minutes, and finally the medium replaced with fresh, phenol red free DMEM plus 10% FBS. The dynamics of Rab GTPase were followed for GFP tagged Rab11 [154] (Addgene #12674)(Figure 5.3, A2 Supplementary Fig. 12-13, Supplementary Video 11-13). For dual labelling of Ras and the endoplasmic

reticulum, we co-transfected the EGFP-HRas construct with pDsRed2-ER (Clontech, cat #632409) (Figure 5.2h, i, A2 Supplementary Fig. 10c, d, Supplementary Video 5, 6), which carries a KDEL ER retention signal.

For OMX SR imaging of GFP-tagged Rab11 (A2 Supplementary Fig. 15, Supplementary Video 17, 18), U2OS cells were seeded onto 35 mm glass bottom MatTek dishes, immersed in DMEM supplemented with 10% FBS and penicillin/streptomycin, and maintained at 37 °C, with 5% CO<sub>2</sub>. Cells were transfected with GFP-Rab11 plasmid using X-tremeGENE™ (Sigma Aldrich) at a ratio of 2:1 (transfection agent:DNA). 24 hours post transfection, cells were transferred to the microscope for imaging.

#### 5.4.17 Membrane Imaging

U2OS were plated on high index coverslips as described above. CellTracker CM-DiI (Thermo Fisher Scientific) was diluted to 1 mg/mL in DMSO and diluted 1:1000 in PBS. The cells were incubated with this solution for 5 minutes at 37 °C, 15 minutes at 4 °C, and the solution replaced with media. Cells were then incubated at 37 °C, 5% CO<sub>2</sub> for 48 hours and imaged (A2 Supplementary Fig. 14, Supplementary Video 15, 16).

#### 5.4.18 Myosin Imaging

For imaging myosin IIA bipolar filaments (A2 Supplementary Fig. 9a, Supplementary Video 10), high index coverslips were plasma cleaned (PDC-001, Harrick Plasma) for 5 minutes, and then coated with 10 µg/ml human plasma fibronectin (Millipore, cat. # FC010) in PBS (Thermo Fisher Scientific). U2OS cells

were cultured in McCoys media (Invitrogen) supplemented with 10% fetal calf serum (Thermo Fisher Scientific), at 37 °C in 5% CO<sub>2</sub>. Cells were transfected with GFP-myosin IIA expression and mApple-F-tractin plasmids as previously described [155] and cultured for 12 hours prior to plating on fibronectin coated coverslips.

#### 5.4.19 Actin Imaging

For actin imaging (Supplementary Video 9), U2OS cells were cultured at 37 °C in the presence of 5% CO<sub>2</sub> in high glucose DMEM medium (Thermo Fisher Scientific) with 10% fetal bovine serum, 1% Pen/Strep and GlutaMAX™ (Thermo Fisher Scientific). Cells were seeded on high index coverslips and transfected with F-tractin EGFP by X-tremeGENE HP (Sigma-Aldrich) 24 hours prior to imaging.

#### 5.4.20 Live INS-1 Cells

For calcium imaging (Supplementary Video 7), INS-1 cells were cultured at 37°C with 5% CO<sub>2</sub> in modified RPMI media (10% fetal bovine serum, 1% pen/strep, 11.1 mM glucose, 10 mM 4-(2-hydroxyethyl)-1-piperazineethanesulfonic acid [HEPES], 2 mM glutamine, 1 mM pyruvate, and 50 µM β-mercaptoethanol). Cells were seeded on high index coverslips that were cleaned by successive washing in detergent and bleach and then thoroughly rinsed with PBS. After PBS rinsing, coverslips were dipped in ethanol to sterilize and allowed to dry. Coverslips were treated with 0.1% poly-L-lysine (Sigma-Aldrich) for (5 to 10 minutes) followed by thorough rinsing with media. Cells were transfected with Lipofectamine 2000 (Thermo Fisher Scientific) using 1 µg of DNA per coverslip. For calcium imaging, cells were transfected with GCamp6S-CAAX and imaged one day after transfection.

#### 5.4.21 Live SK-MEL Cells

For FCHO (A2 Supplementary Fig. 9b) imaging, SK-MEL cells were cultured in standard DMEM without phenol red (10% fetal bovine serum, 1% pen/strep, 1% GlutaMAX) at 37°C with 5% CO<sub>2</sub>. Cells were seeded and transfected (with FCHO2-GFP in this case) as described above for calcium imaging.

## Chapter 6 Discussion

In Chapter 3, I described the use of fluorescence microscopy to examine actin structures and dynamics in U2OS cells. In both live and fixed cells, actin structures form in response to structures external to the cell. As has been previously reported, for cells plated on nanopattern substrates with consecutive parallel grooves, actin structures form within the confines of each groove [88]. Using super-resolution techniques such as structured illumination and STED microscopy, I examined the shape and features of actin structures at the nanoscale. Visualized actin displays repeatable features that resemble transverse waves in the plane parallel to the coverslip. These actin structures are found across both fixed and live cells, and I quantified the physical dimensions of the observed structures. The wave-like actin features have average length scales suggesting they can fill the full width of the grooves, and they oscillate between the groove borders with a distinct distribution of peak separations. Since the grooves confine the actin, it is difficult to make direct measurements of persistence length, but estimates suggest the actin structures have a longer persistence length than single actin filaments [156].

These actin structures are dynamic in live cells [91], as they are observed to move primarily along the axis of the grooves. In addition to super-resolution imaging, I took advantage of the fast 3D imaging capabilities of iSIM [70] to examine actin shapes and motion in all dimensions, in live cells. I found the transverse wave-like features were also observed in live cells, although with lower amplitude and larger separation between peaks. This can be attributed in part to the resolving power of the microscopes used, as the STED achieves higher spatial resolution and is better able to

resolve fine structure. Also, as the structures are transient in live cells, I believe that this could also contribute to difference in structure characteristics. Timelapse imaging shows that peaks and valley in actin structures are persistent, but they move slightly in both lateral dimensions. Because the actin structures appear to demonstrate some minimum stiffness, as well as the propensity to change shape over time, the data suggest that the observed actin structures are comprised of groups of actin filaments.

I adapted optical flow analysis to 3D to track the local motion of actin in 3D and found that while motion of actin appears to be primarily parallel to the coverslip surface, actin also appears to explore the depth of the grooves. Because each observed actin structure is formed in a cell protrusion that extends into the grooves, 3D information may provide valuable information about the role actin plays in forming, maintaining, and shifting these cell protrusions. While my results suggest actin motion is both parallel to the coverslip, and to a lesser extent perpendicular, future experiments could follow up my initial observations more rigorously. The 3D optical flow analysis described is useful for characterizing motion in actin in live cells, but it is more generally applicable to any 3D fluorescence microscopy data with intensity distributions varying over time.

Because of objective lens orientation, many optical microscopes have worse axial resolution than lateral resolution. Some techniques, such the STED microscope utilized in Chapter 3, allow for improved axial resolution, but these techniques often induce too much photobleaching and phototoxicity for live cell imaging. While fast live cell 3D imaging with instruments such as the iSIM already provide valuable information, the relatively poor axial resolution makes it difficult to resolve fine

features in that dimension. For the application of observing actin around patterned substrates, improved axial resolution would help better characterize actin structures in 3D. Improved techniques like the TIRF iSIM described in Chapter 5 will help improve axial resolution and optical sectioning to enable this variety of 3D measurements. TIRF techniques do not intrinsically provide increased axial resolution, their primary advantage is increased optical sectioning, but some techniques have provided increased axial resolution [157]. TIRF iSIM is not immediately compatible with imaging cells on patterned substrates because of interference between the illumination pattern and substrate structures. Also, TIRF imaging is limited to a few hundred nanometers, so the dimensions of the patterns would limit the imaging area occupied by cells. Hopefully this type of improvement in axial resolution, when combined with a fast, super-resolution instrument like the iSIM, will enable even more accurate characterization of actin structures in 3D.

The experiments described in Chapter 3 motivate several avenues of future study. First, while the patterned substrates used showed interesting results, one can imagine changing the dimensions of the patterns to provide further insights. A variety of groove separations could help illuminate the conditions under which actin structures form in the grooves, and a range of groove depths could help show how far cellular protrusions extend into cavities. Imaging different proteins, such as myosin, could help further clarify the role structural proteins play in forming protrusions. Myosin can connect parallel actin filaments, and contractive forces myosin generates will slide the filaments in opposite directions [6]. If myosin is colocalized to actin structures in grooves, this suggests that myosin and the force it generates may play a

role in generating the cellular protrusion. Imaging elements of the cell membrane could help provide additional information about how far cellular protrusions extend into cavities. As described in Chapter 3, applying drugs like Latrunculin and Blebbistatin will help examine changes when actin and myosin fibers are disrupted.

In Chapter 4, I describe a method for providing fast, accurate control of MEMS mirrors for laser beam steering applications. Using a deconvolution-based algorithm, I can increase the speed of MEMS mirror scanning by a factor of 20 while also improving scan accuracy. The motivation for this work was to improve the imaging speed capabilities of existing point-scanning and line-scanning microscopes. Using this algorithm, I developed a raster pattern for use in a simple point-scanning microscope, but the applications for the algorithm are wide-ranging. Light sheet microscopes often use MEMS mirrors for laser beam scanning to create illumination light sheets, but the speed of this scanning is still a limiting factor in imaging speed. I explored designing and building a light sheet microscope to utilize this algorithm and was able to achieve some success in enabling high speed 3D imaging. Technical limitations for this type of high-speed imaging technique still exist, such as optical refocusing speed [158] and camera exposure rate, which leaves room for further development. In addition to mirror scanning, my control algorithm can be applied to different hardware devices. For example, I successfully applied this algorithm to control a piezoelectric objective positioner, enabling higher speed operation for optical refocusing.

The microscopy technique described in Chapter 5 helps improve the optical sectioning of an existing fast, super-resolution fluorescence microscope (iSIM) by

adding TIRF capability. To do this, I designed and implemented an alternate illumination path that blocked non-TIRF illumination light while maintaining the existing structured illumination pattern. To demonstrate the usefulness of this technique, we examined the dynamics of protein distributions in live cells, including fast dynamics of the GTPase Rab11 and the GTPases HRas near the plasma membrane. As described above, additional axial resolution and optical sectioning allows for more accurate characterization of structures in 3D. To this end, a technical improvement that could be made to this device would be to enable finer control of the evanescent wave depth in the sample. By adding a device to control the range of illumination angles that make it to the sample, finer control of the illumination depth could be achieved. The photobleaching characteristics of fluorophores could also be leveraged to provide additional control over the optical sectioning capabilities of this device [147].

## Chapter 7 Appendices

### A1

#### A1.1 Laser Scanning Test Rig Components List

- Coherent Sapphire 200 mW, 488 nm laser
- AA Optoelectronic Acousto-optical tunable filter (AOTF, Quanta Tech, AOTFnC-400.650-TN)
- Thorlabs, half-wave plate, WPH10M-488
- Thorlabs, f1 = 40 mm achromatic doublet, AC254-040-A-ML
- Thorlabs, f2 = 35 mm achromatic doublet, AC254-035-A-ML
- Edmund Optics, 1.0 OD, 30935
- Thorlabs, f3 = 75 mm achromatic doublet, AC254-075-A-ML
- Mirrorcle Technologies, Gimbal-less Two Axis MEMS Mirrors, angular range +/- 4.6 degrees mechanical, A1B2.5-1200AL-DIP24-A/TP
- Mirrorcle Technologies, DIP24 Packaging MINI-DIP24-5.x-MNT
- Thorlabs, f4 = 40 mm triplet, TRH254-040-A-ML
- PCO-TECH, pco.edge 5.5
- Mirrorcle Technologies, BDQ amplifier MEMS Driver DR-11-033-01 @XI Custom Workstation
- National Instruments, Analog out card, PXI-6733sample

#### A1.2 Point Scanning Microscope Test Rig Components List

- Coherent Sapphire 200 mW, 488 nm laser
- AA Optoelectronic Acousto-optical tunable filter (AOTF, Quanta Tech, AOTFnC-400.650-TN)
- Thorlabs, half-wave plate, WPH10M-488
- Thorlabs, f1 = 40 mm achromatic doublet, AC254-040-A-ML
- Thorlabs, f2 = 35 mm achromatic doublet, AC254-035-A-ML
- Thorlabs, f3 = 125 mm achromatic doublet, AC254-125-A-ML
- Thorlabs f4 = 40 mm triplet, TRH254-040-A-ML
- Mirrorcle Technologies, Gimbal-less Two Axis MEMS Mirrors, angular range +/- 4.6 degrees mechanical, A1B2.5-1200AL-DIP24-A/TP
- Mirrorcle Technologies, DIP24 Packaging MINI-DIP24-5.x-MNT
- Thorlabs, f4 = 40 mm triplet, TRH254-040-A-ML
- Thorlabs, f5 = 400 mm achromatic doublet, AC254-400-A-ML
- Olympus UPlanFl 10X Air Objective
- Semrock dichroic beamsplitter Di03-R488/561-t3-25x36
- Thorlabs, f5 = 400 mm achromatic doublet, AC254-400-A-ML
- Semrock 488 nm RazorEdge ultrasteep long-pass edge filter LP02-488RU-25
- PCO-TECH, pco.edge 5.5
- Mirrorcle Technologies, BDQ amplifier MEMS Driver DR-11-033-01

- @XI Custom Workstation
- National Instruments, Analog out card, PXI-6733

### Supplementary Figure 1

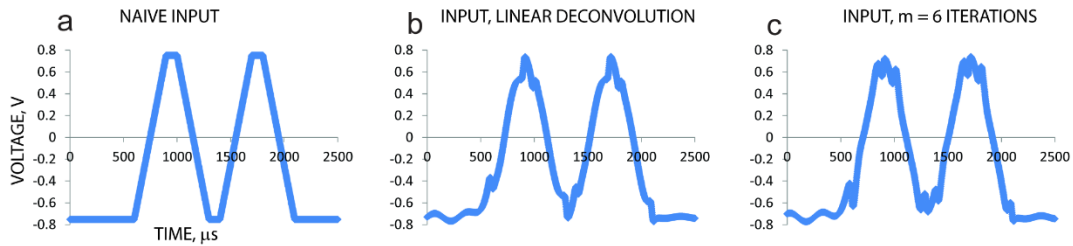


Figure 7.1 Input voltage comparison

Supplementary Figure 1: Example input voltages to MEMS mirror, comparing naïve input (i.e. proportional to desired scan pattern, a), the input predicted by linear deconvolution (b), and the input calculated by 6 iterations of our iterative, measurement-based deconvolution algorithm (c). The desired scan pattern has 300  $\mu\text{s}$  /sweep and 100  $\mu\text{s}$  /turnaround.

### Supplementary Figure 2

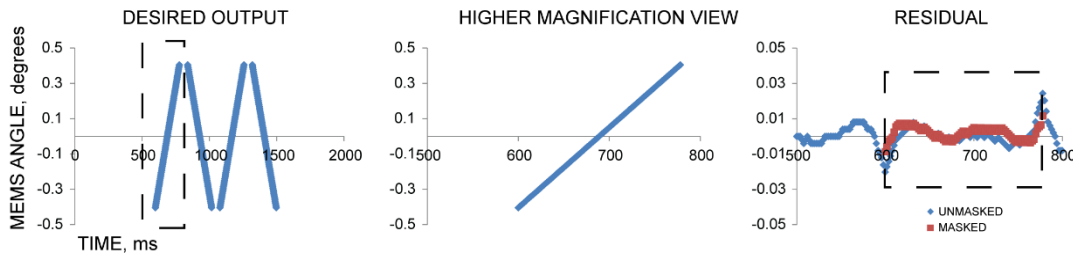


Figure 7.2 Masking the residual in unimportant areas

Supplementary Figure 2: Most scan patterns contain regions in which accuracy is irrelevant. For instance, the turnaround or flyback regions in a raster pattern need not be accurate, as no data will be collected during this time. Furthermore, it is often difficult to define exactly what the "desired" result is in undefined regions. For the sake of this demonstration, we assume the turnaround regions, not depicted in the desired output, are stationary pauses. It is possible to achieve higher accuracy in important areas of the scan pattern if unimportant areas are neglected. This is achieved by masking (setting equal to zero) the residual in these unimportant areas, and only incorporating the residual in important areas (unimportant regions are not plotted) when performing the iterative deconvolution algorithm. In this example the desired scan pattern (left), a higher magnification view (middle, corresponding to dashed box at left) and residual (right) are shown, for a pattern with 180  $\mu\text{s}$ /sweep and 60  $\mu\text{s}$ /turnaround. In the residual plot, two results are shown: the red line is the residual result when only the scan region (indicated by the dashed box) is unmasked,

the blue line is the residual without masking (i.e. the entire pattern is optimized). Within and especially towards the edges of the important region, the masked optimization is more accurate.

A2

Supplementary Figure 1

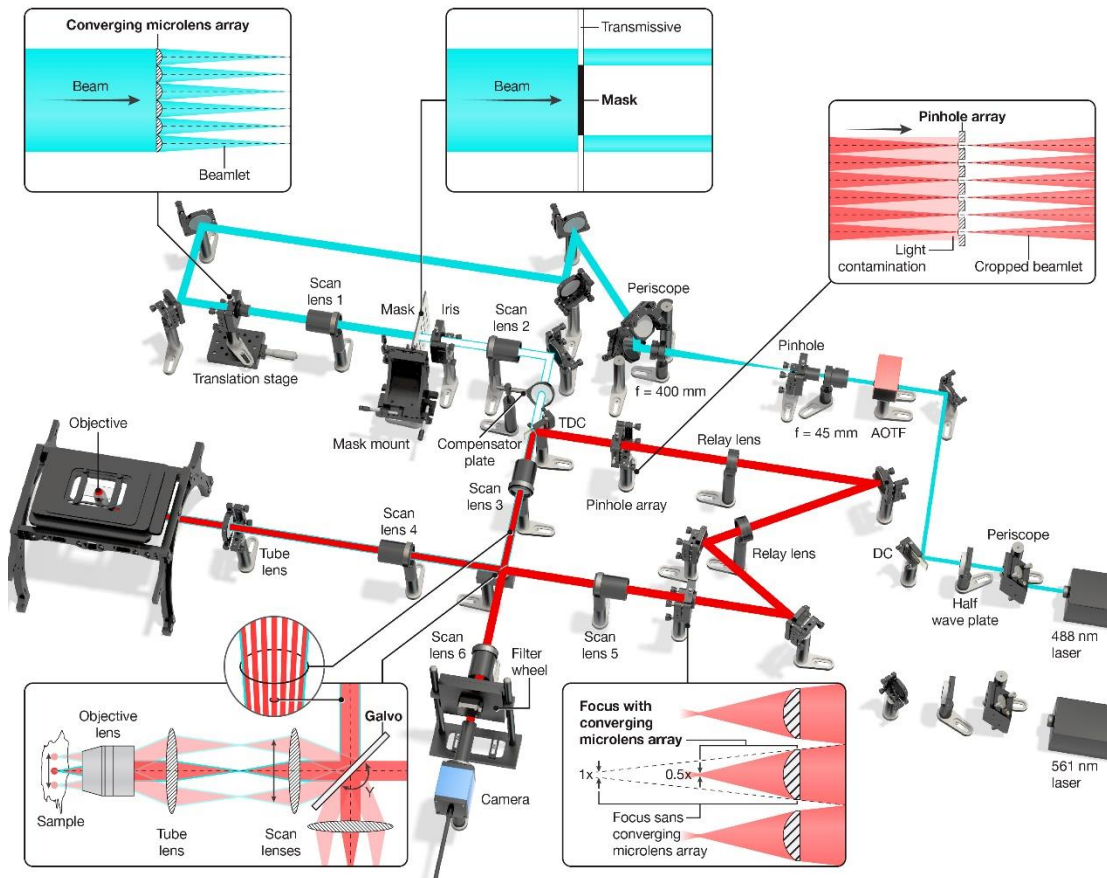


Figure 7.3 Instant TIRF- SIM instrument schematic

Supplementary Figure 1: 488 nm and 561 nm lasers are combined and passed through an acousto-optical tunable filter (AOTF) for shuttering, beam expanded and spatially filtered ( $f = 45$  mm and  $f = 400$  mm achromats with  $100 \mu\text{m}$  pinhole placed at the co-focal point between these lenses), and directed to an excitation microlens array. An opaque circular mask placed at the co-focal point between Scan lens 1 and Scan lens 2 (one focal length from the excitation foci produced by the microlens array) serves to block subcritical excitation (blue), producing annular illumination. For clarity, only a single on-axis beamlet produced by the central microlens is shown impinging on the

mask. Scan lens 2 and 3 relay the mask to a 2 sided galvanometric mirror, with a Compensator plate reducing astigmatism that would otherwise result as the beam is transmitted through a thick dichroic mirror (TDC). A tube lens and Scan lens 4 further magnify and relay the mask to the back focal plane of a high NA (1.7) objective. Scanning the galvo translates the TIRF excitation pattern at the sample. Fluorescence is collected along the same optical path, descanned from the galvo and reflected from TDC. Emission-side optics are nearly identical to those used in our previous work (see Methods for further description). Note that distances, angles, and ray diagrams are only approximate.

Supplementary Figure 2

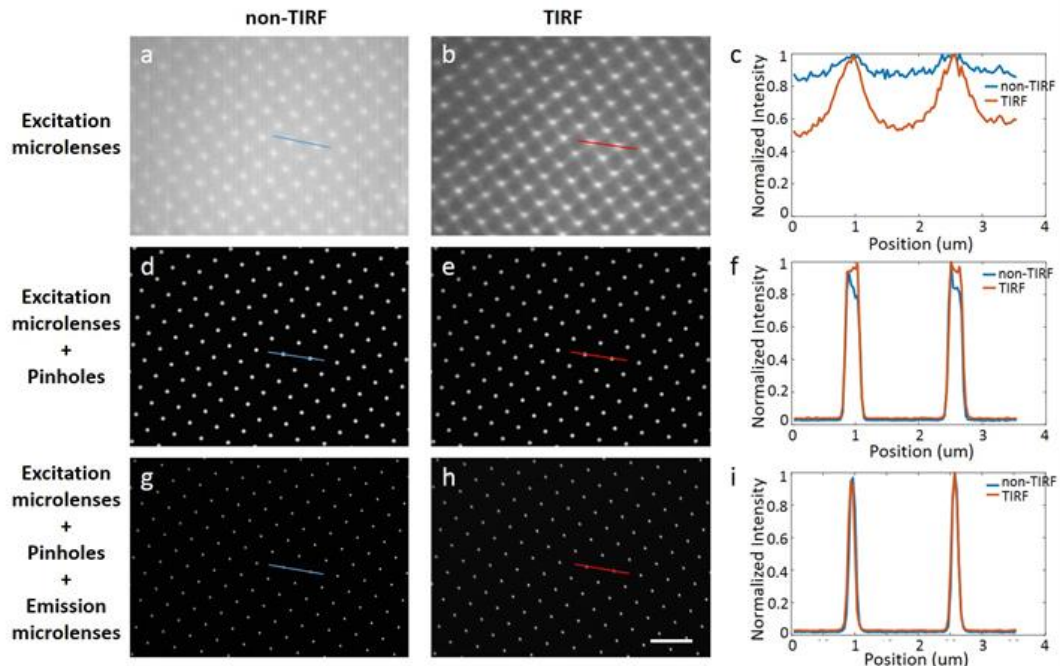


Figure 7.4 Comparative (non-TIRF/TIRF) excitation and emission patterns after micro-optics

Supplementary Figure 2: The response of each micro-optic as measured with fluorescence dye solution is shown for non-TIRF (entire objective back aperture illuminated, left column) and TIRF (annular illumination, middle column) excitation. Line scans corresponding to red lines in each image are shown in right column (blue: non-TIRF imaging; red: TIRF imaging). Although contrast using excitation microlenses is much better in TIRF than in non-TIRF imaging, there is still residual background between excitation foci. This background is removed after adding pinholes; performance after pinholes (second row) and with emission microlenses (third row) is virtually identical whether exciting in TIRF or not. Note that these images were acquired with the galvanometric mirror held stationary, to visualize the emission around individual excitation foci. Scale bar: 2  $\mu\text{m}$ . Experiments were repeated at least 3 times with similar results; representative data are shown.

Supplementary Figure 3

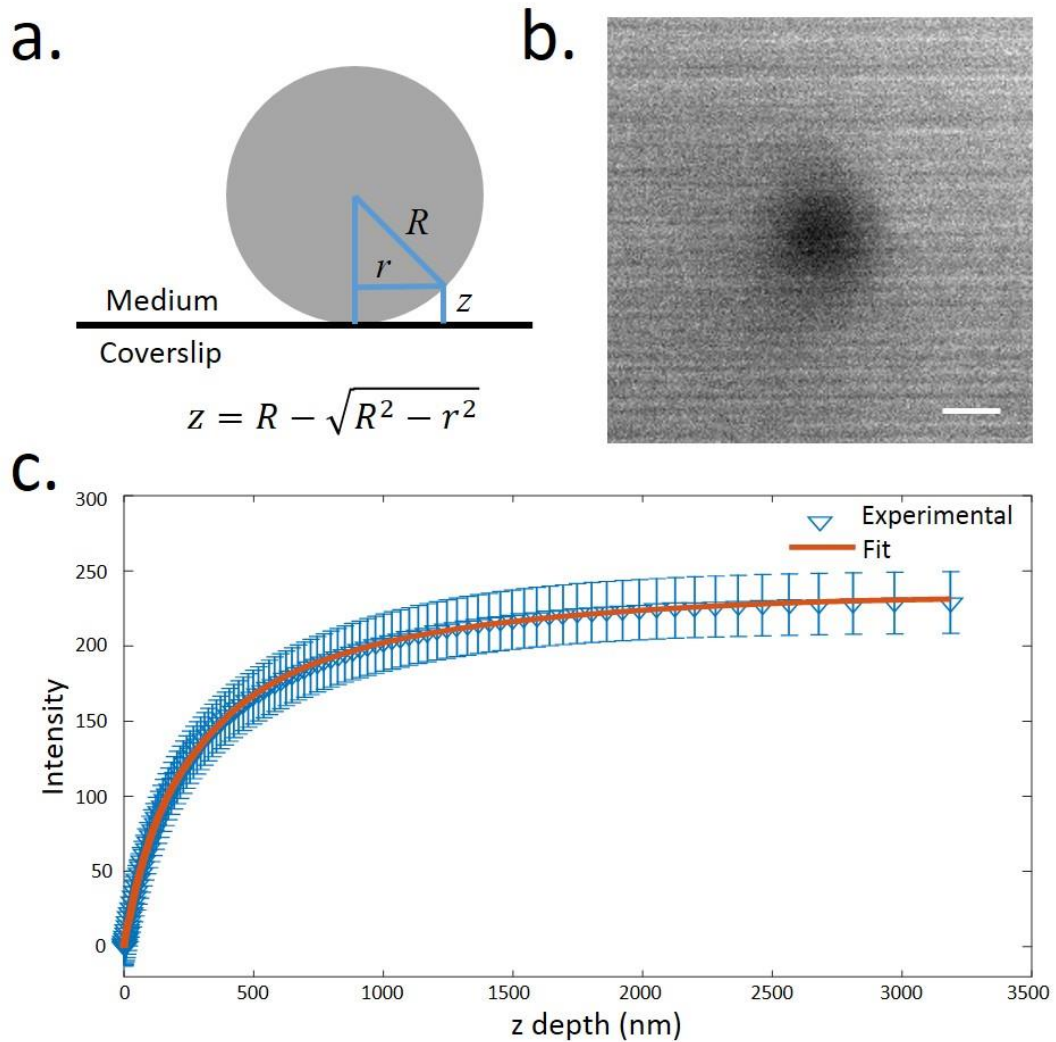


Figure 7.5 Estimating evanescent field decay length with silica beads placed in fluorescent dye

Supplementary Figure 3: a) Experimental geometry. Given the known radius of the silica bead  $R$ , the apparent radius  $r$  recorded from the measurement can be converted to an axial coordinate  $z$  using geometry. b) Representative bead image showing dark central region corresponding to excluded dye region, surrounded by fluorescence signal corresponding to dye. Images were inverted and the centroid computed. Based on the centroid, a ring with 1 pixel width and radius of  $r$  was drawn, and the intensity of all pixels within the ring averaged. By varying  $r$ , the averaged intensity profile versus  $r$ ,  $F(r)$  was obtained. The signal at  $r = 0$  was regarded as background and subtracted from the profile. Then,  $F(r)$  was transformed to  $F(z)$ , by computing  $z$  as  $R - (R^2 - r^2)^{0.5}$ . Data from  $n = 7$  independent beads were averaged (c), central value represents mean and error bars indicates standard deviation) fitted to a sum of two exponentials as described in Methods, and fit parameters extracted to determine the

decay length. Scale bar: 1  $\mu\text{m}$ . Experiments were performed at least 4 times with similar results; representative data are shown.

Supplementary Figure 4

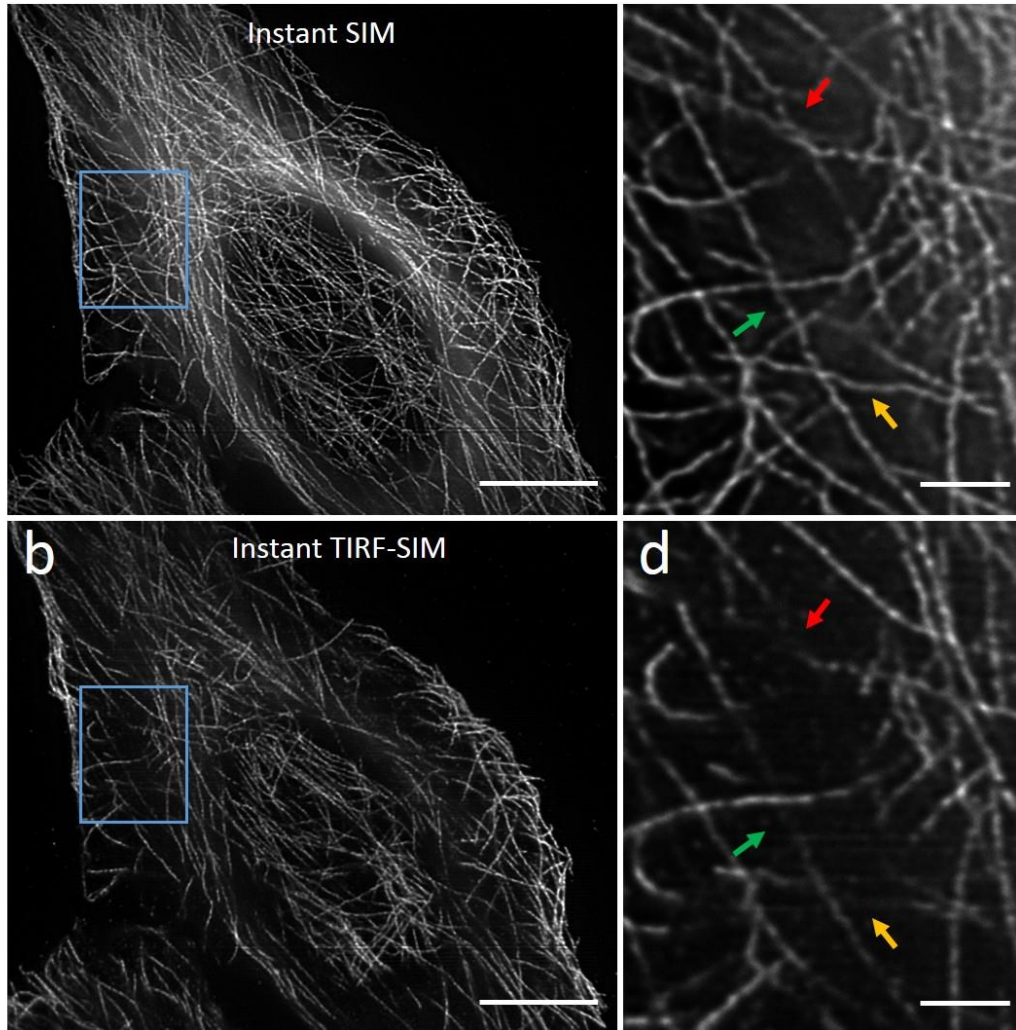


Figure 7.6 Qualitative instant SIM comparisons highlight the effect of TIRF.

Supplementary Figure 4: U2OS cells were fixed, microtubules immunostained with Alexa Fluor 488, and the same field imaged in instant SIM (non-TIRF illumination) (a) and instant TIRF-SIM (b). Arrows in higher magnification views (c, d) highlight features evident in instant SIM imaging but absent or attenuated in instant TIRF-SIM. Images have been delined as described in Supplementary Fig. 5-7. Scale bars: 10  $\mu\text{m}$  in a, b; 2  $\mu\text{m}$  in c, d. Experiments were repeated at least 4 times with similar results; representative data are shown.

Supplementary Figure 5

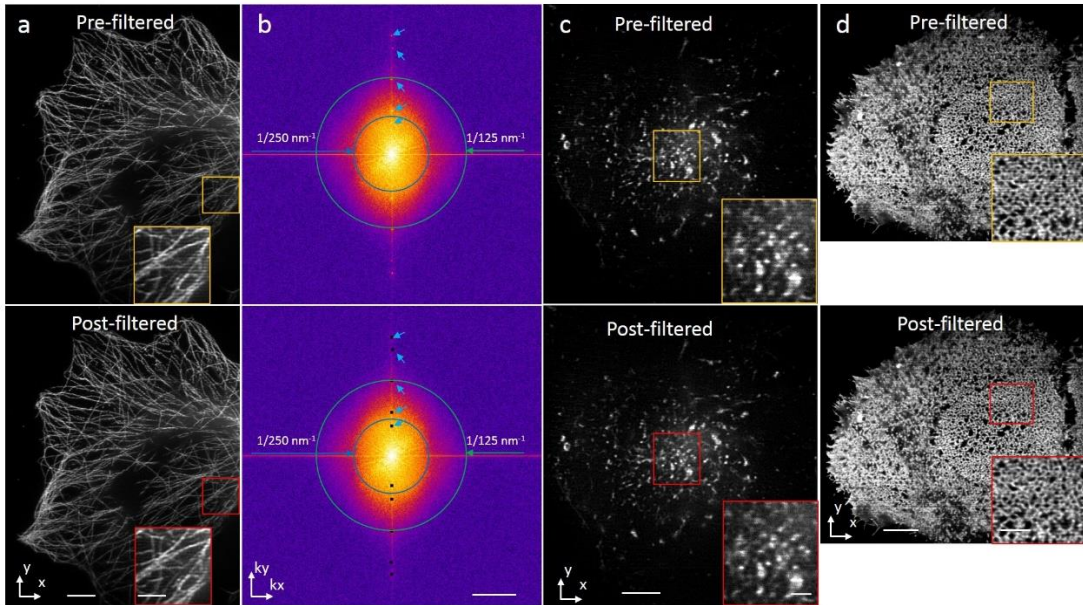


Figure 7.7 Delining instant-TIRF SIM data.

Supplementary Figure 5: a) Example of data from Fig. 1a. Top: before delining, bottom: after delining. b) corresponding power spectra of images in a). Top: power spectrum corresponding to the image before delining. Blue arrows highlight locations in Fourier space that correspond to horizontal line artifacts in the image. Bottom: power spectrum corresponding to the image after delining. Notch filters (black rectangular regions of zero intensity) are selectively applied, resulting in suppression of line artifacts. c), d) Additional examples from data presented in Fig. 2c and Fig. 3a, highlighting delining. Insets show higher magnification views of yellow and red rectangular regions. Scale bars: a), c) and d) 5  $\mu\text{m}$ , insets 2  $\mu\text{m}$ , b) 1/200  $\text{nm}^{-1}$ . Experiments were repeated at least 4 times with similar results; representative data are shown.

Supplementary Figure 6

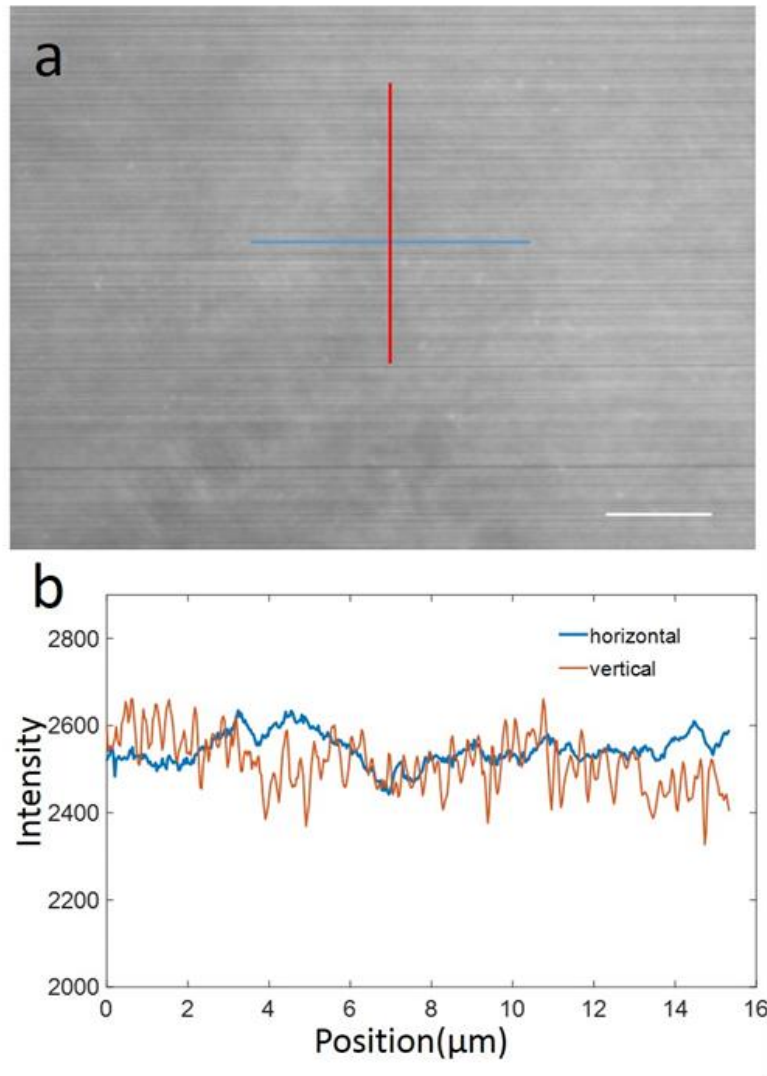


Figure 7.8 Residual intensity variations after delining procedure

Supplementary Figure 6: a) Fluorescent dye, imaged in instant TIRF-SIM, flat-fielded and delined according to procedure in Supplementary Fig. 5. Red and blue lines indicate profiles in vertical (perpendicular to line artifact) and horizontal (parallel) directions. b) Variation in intensity along line profiles in a). Although vertical variations are larger than horizontal, they are still only  $\sim 2.4\%$  of the mean intensity of the sample. Scale bar:  $5 \mu\text{m}$ . Experiments were repeated 3 times with similar results; representative data are shown.

Supplementary Figure 7

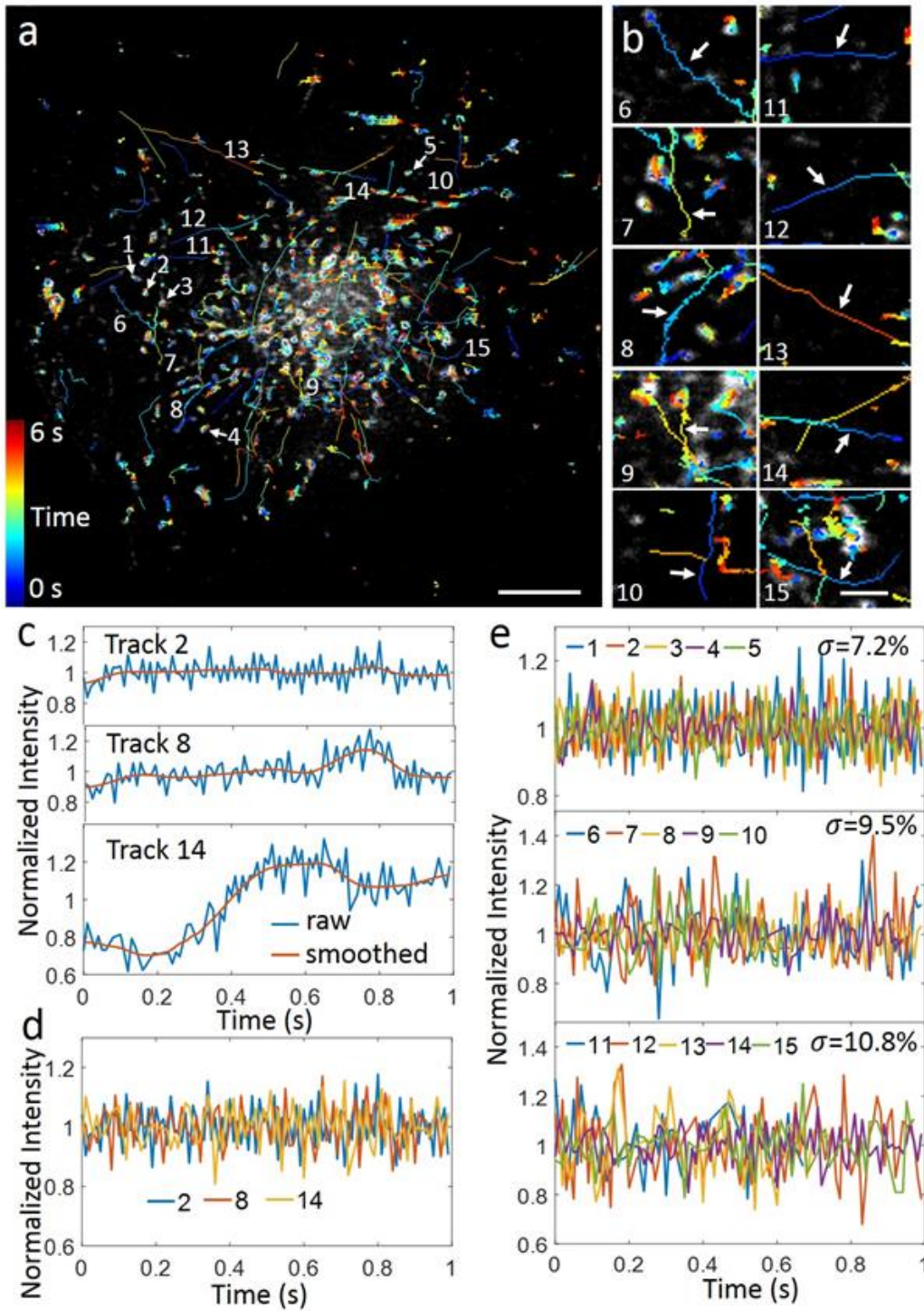


Figure 7.9 Intensity fluctuations in delineated EGFP-Rab11 data along the vertical direction are no greater than along the horizontal direction

Supplementary Figure 7: a) Data shown in Fig. 3a, with 15 selected tracks (#1-5 highlighted with white arrows, relatively stationary tracks with displacement  $< 0.3 \mu\text{m}$ ; #6-10, tracks with motion primarily along vertical direction, perpendicular to the line artifact; #11-15, tracks with motion primarily along horizontal direction, parallel

to line artifact). b) Higher magnification views of tracks 6-15, highlighted with white arrows. c) Example intensities from tracks 2, 8, 14. Intensities have been normalized to the mean (=1) and then smoothed with the 'smoothdata' function in Matlab, with a Gaussian kernel of window size 20. Both raw (blue) and smoothed (red) traces are shown. d) Examples in c after subtracting smoothed traces, emphasizing high frequency intensity variations. e) As in d), but now showing high frequency intensity variations for all tracks in relatively stationary (top), primarily vertical (middle) and primarily horizontal (bottom) tracks. Also shown are the mean standard deviations  $\langle \sigma \rangle$  as a percentage of the mean intensity in each panel. Although  $\langle \sigma \rangle$ s derived from vertical and horizontal tracks are both slightly greater than stationary tracks, they are within 1% of each other. Scale bars: 5  $\mu\text{m}$  in a, 1  $\mu\text{m}$  in b. Experiments were repeated 4 times with similar results; representative data are shown.

Supplementary Figure 8

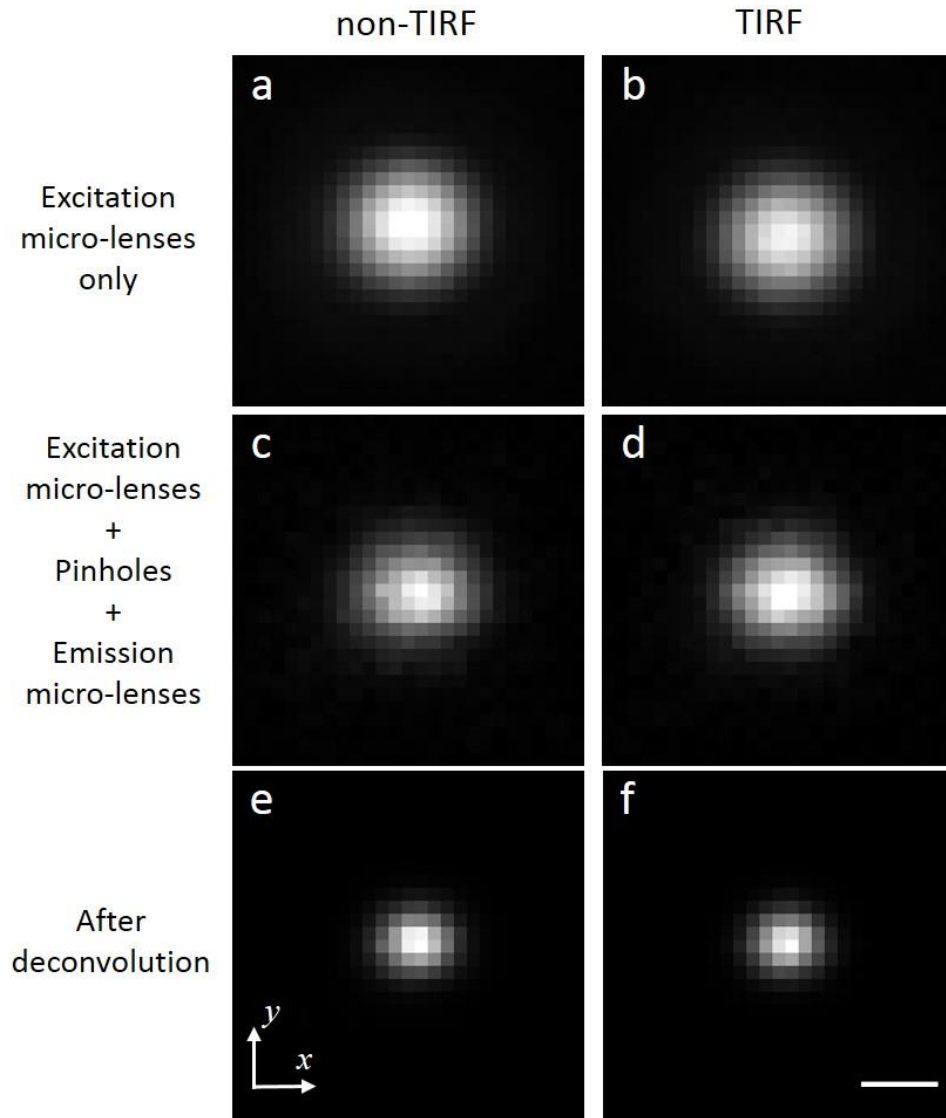
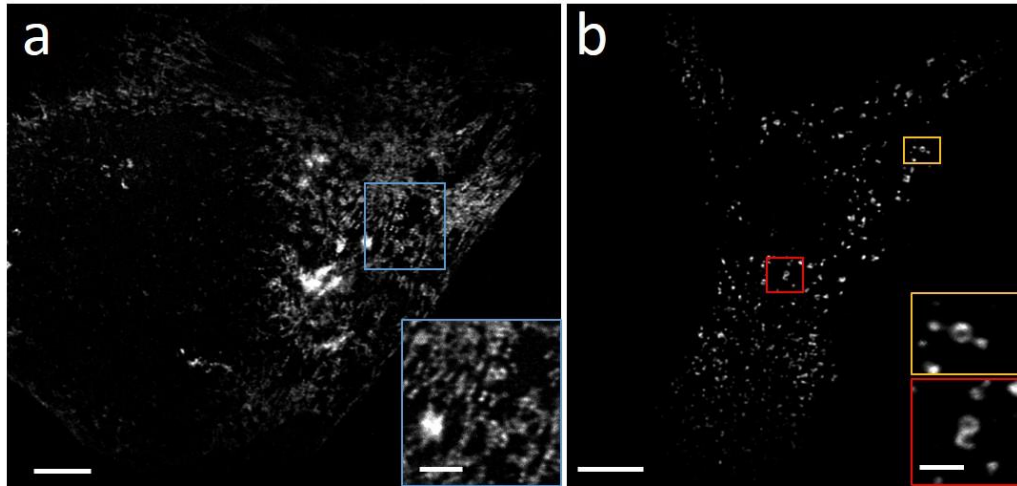


Figure 7.10 Representative bead images

Supplementary Figure 8: Beads were imaged using non-TIRF illumination (a, c and e) and in TIRF (b, d and f). Bead appearance is similar regardless of imaging modality. Scale bars: 200 nm.

Supplementary Figure 9



*Figure 7.11 Biological resolution standards in instant TIRF-SIM*

Supplementary Figure 9: a) GFP-Myosin IIA in live U2OS cells. Inset highlights myosin IIA bipolar filaments. b) GFP-FCHO2 in live SK-MEL cells. Inset highlights substructure within individual FCHO2 puncta. Scale bars: a) 5  $\mu\text{m}$ , inset 2  $\mu\text{m}$ ; b) 5  $\mu\text{m}$ , insets 1  $\mu\text{m}$ . Experiments were performed at least 3 times with similar results; representative data are shown.

Supplementary Figure 10

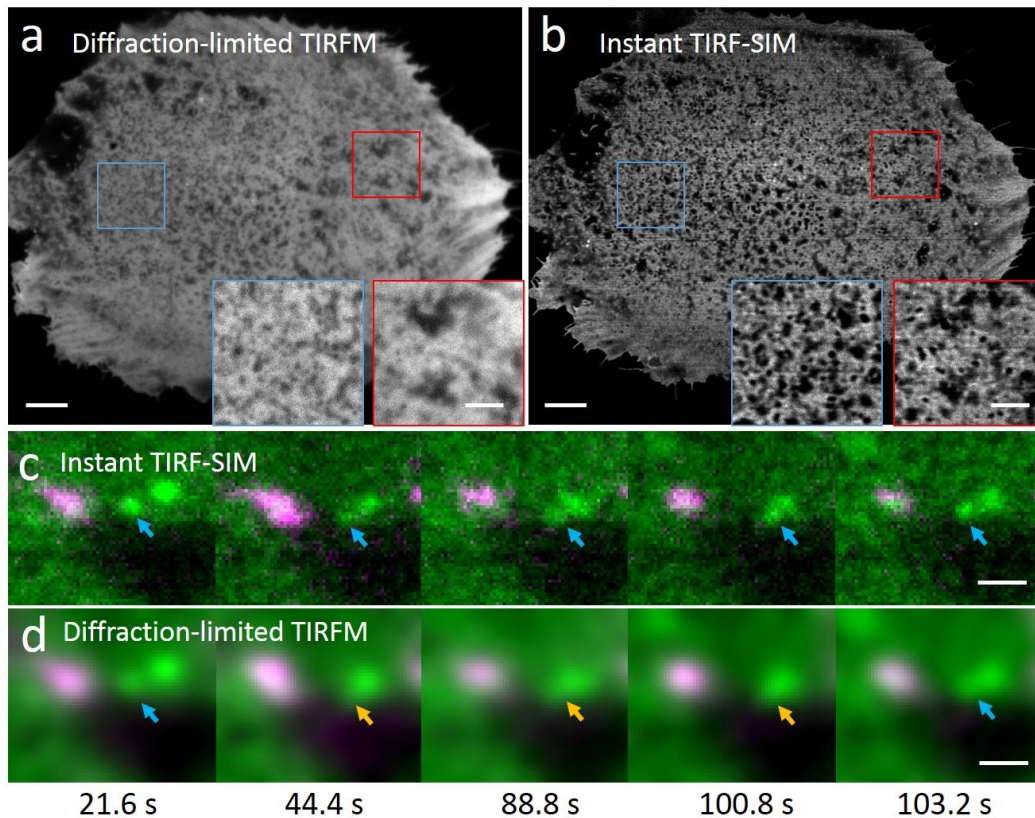


Figure 7.12 Instant TIRF-SIM better resolves Ras microdomains than diffraction-limited TIRF

Supplementary Figure 10: a) Image taken of GFP-HRas in U2OS cell in diffraction-limited TIRF, i.e. with pinholes and emission microlenses removed. Insets correspond to higher magnification views of blue and red rectangular regions. b) Image taken in the same cell as in (a) but with instant TIRF-SIM. c) Selected image frames taken of GFP-HRas (green) and pDsRed2-ER (magenta) in U2OS cells from instant TIRF-SIM acquisition. d) The same images as (c) but blurred to simulate diffraction-limited images. Arrows highlight two microclusters resolved in instant TIRF-SIM but not in TIRF. See also Fig. 2i, Supplementary Video 6. Scale bars: a) and b): 5  $\mu\text{m}$ ; insets, 1  $\mu\text{m}$ ; c) and d): 500 nm. Experiments were performed at least 4 times with similar results; representative data are shown.

Supplementary Figure 11

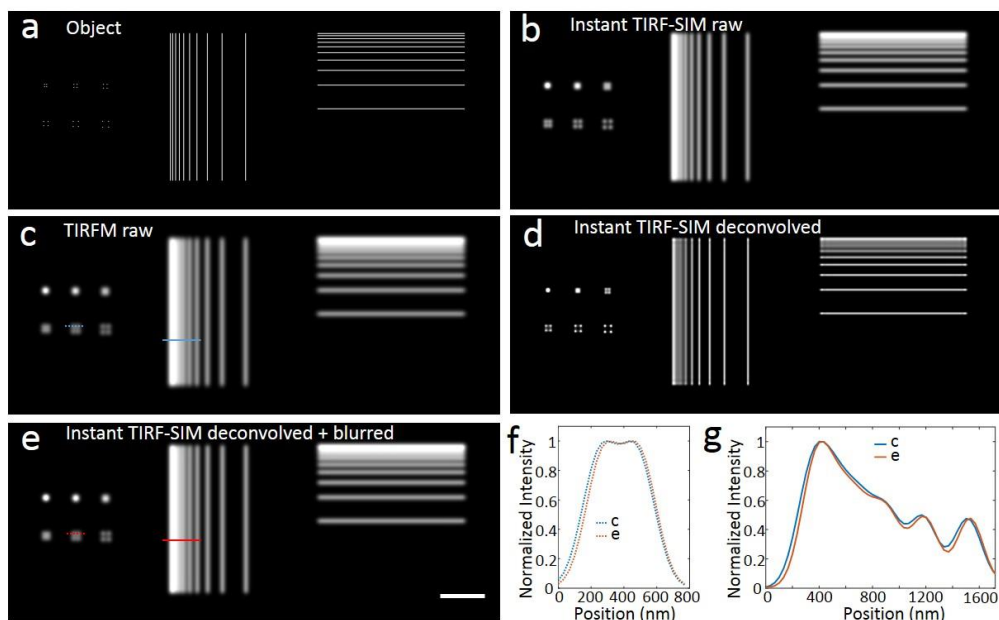


Figure 7.13 Simulating diffraction-limited TIRF data from instant TIRF-SIM data

Supplementary Figure 11: a) Synthetic object. b) The object blurred with the raw instant TIRF-SIM PSF, derived from beads (e.g. Supplementary Fig. 8d). This image represents what is captured on the camera. c) The object blurred with the diffraction-limited TIRF PSF (e.g. Supplementary Fig. 8b). This is what the camera would measure with emission micro-optics removed. d) The deconvolved instant TIRF-SIM image. e) The image that results after blurring d) with a PSF with kernel  $\sigma = (\sigma^2_{\text{DIFFRACTION-LIMITED}} - \sigma^2_{\text{INSTANT TIRF-SIM}})^{0.5}$  where  $\sigma_{\text{INSTANT TIRF-SIM}}$  is derived from the deconvolved instant TIRF-SIM PSF (e.g. Supplementary Fig. 8f). Compare c) to e) – they are near identical as line plots in f) and g) (corresponding to blue and red lines in c, e) confirm.

Supplementary Figure 12

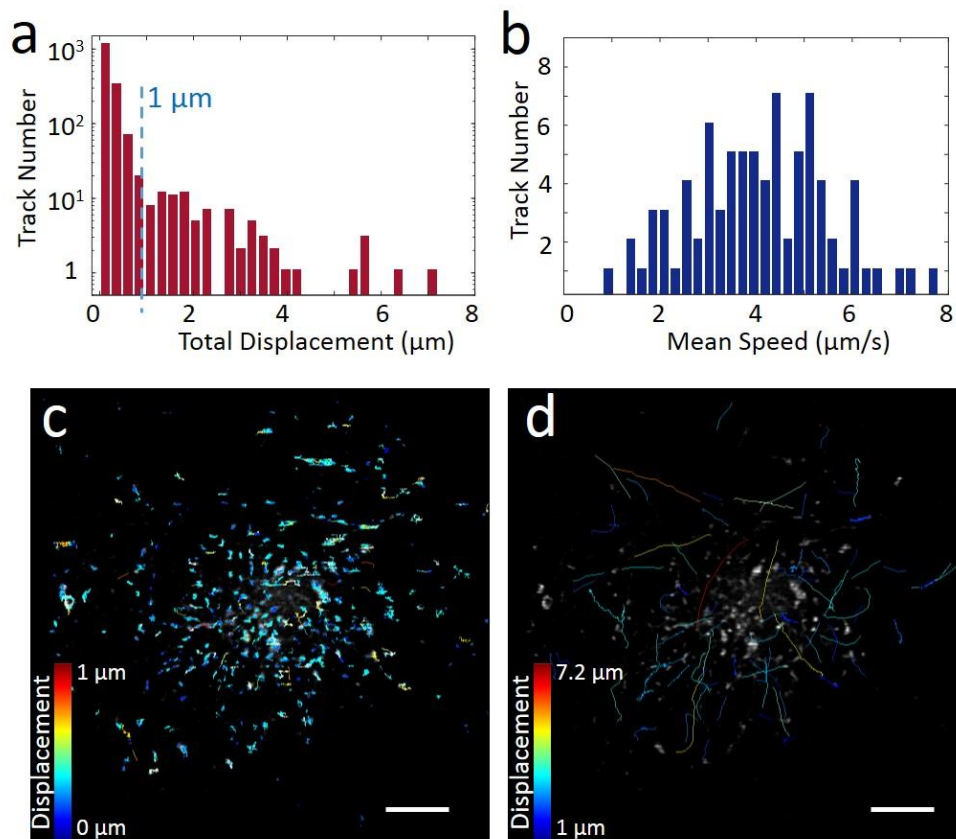


Figure 7.14 Displacement and mean speed of tracked EGFP-Rab11 particles.

Histograms of total displacement for all tracks (a) and mean speed of the tracks with displacement greater than  $1\ \mu\text{m}$  (b), in addition to visual display of particle tracks with displacement less than (c) and greater than (d)  $1\ \mu\text{m}$  overlaid on first frame of image series. Scale bars:  $5\ \mu\text{m}$ . See also Fig. 3. Experiments were performed at least 4 times with similar results; representative data are shown.

Supplementary Figure 13

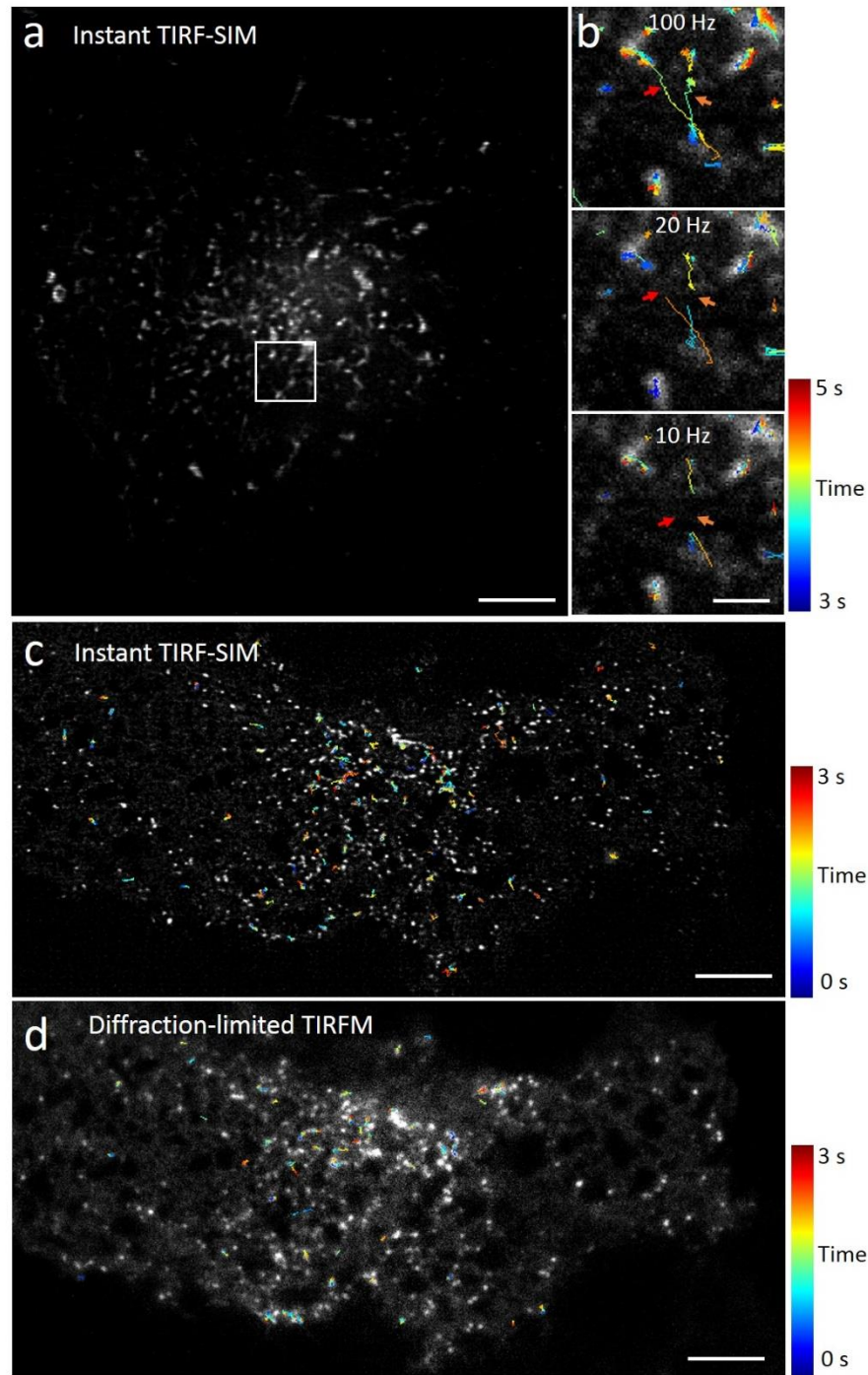
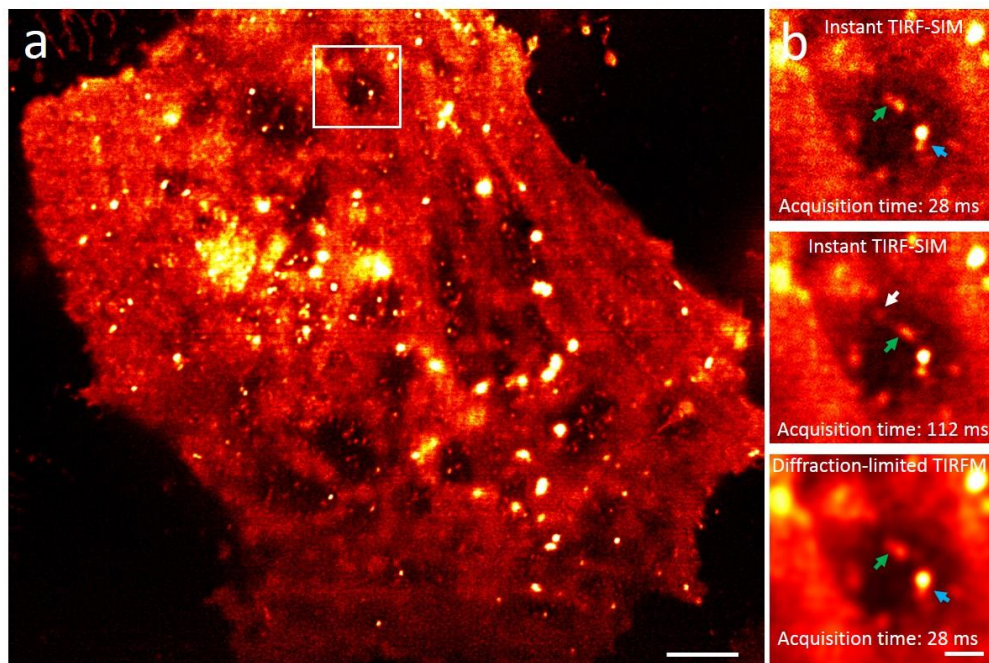


Figure 7.15 Effect of temporal undersampling and spatial blurring on automated tracking on EGFP-Rab11 particles

Supplementary Figure 13: a) First frame of image series corresponding to Fig. 3. b) Effect of sampling at 100 Hz (i.e. native recording rate, top), digitally downsampling to 20 Hz (middle) and digitally downsampling to 10 Hz (bottom). Temporal evolution of each track is indicated with color bar at right, red and orange arrows highlight

examples of automatically detected tracks (top) that are artificially shortened (middle) and eventually lost (bottom) due to undersampling. Particle tracking was performed on a different cell imaged in instant TIRF-SIM (c, first frame in 300 frame series) and subsequently pinholes and emission microlenses were removed so that the same sample was imaged (for another 300 frames) in diffraction-limited TIRFM (d). 1477 trajectories were detected in instant TIRF-SIM whereas only 1031 were detected in TIRFM. For clarity, only those tracks that were automatically detected and that cover a displacement  $> 0.3 \mu\text{m}$ , are shown in the figure (121 in c, 76 in d). We observed a similar increase in detected particle trajectories in an additional cell (1317 total trajectories in instant TIRF-SIM vs. 1107 in TIRF). Scale bars:  $5 \mu\text{m}$  in a, c and d,  $1 \mu\text{m}$  in b. See also Supplementary Videos 12-13. Experiments were repeated at least 3 times with similar results; representative data are shown.

#### Supplementary Figure 14



*Figure 7.16 Diffractive or motion blur obscures vesicle motion at the plasma membrane*

Supplementary Figure 14: a) Still image from 100-frame instant TIRF-SIM series, acquired at  $37^\circ\text{C}$ . Plasma membrane and vesicles are stained with CellTracker CM-DiI in a live U2OS cell. The 'hot' colormap in ImageJ was used for image display due to the large dynamic intensity range in the sample. b) Higher magnification view of white rectangular region in a) comparing instant TIRF-SIM (top), 4 successive frames binned in time (middle) to simulate motion blur, and the same region blurred to simulate diffraction-limited acquisition (bottom). Blue arrows highlight vesicle pair resolved in instant TIRF-SIM but not in diffraction-limited image. Green arrow

highlights vesicle pair resolved in instant TIRF-SIM but blurred due to motion or diffractive blur. White arrow highlights artifact - an apparent vesicle - due to motion blur. Scale bars: 5  $\mu\text{m}$  in a), 1  $\mu\text{m}$  in b). See also Supplementary Video 15, 16. Experiments were repeated 3 times with similar results; representative data are shown.

### Supplementary Figure 15

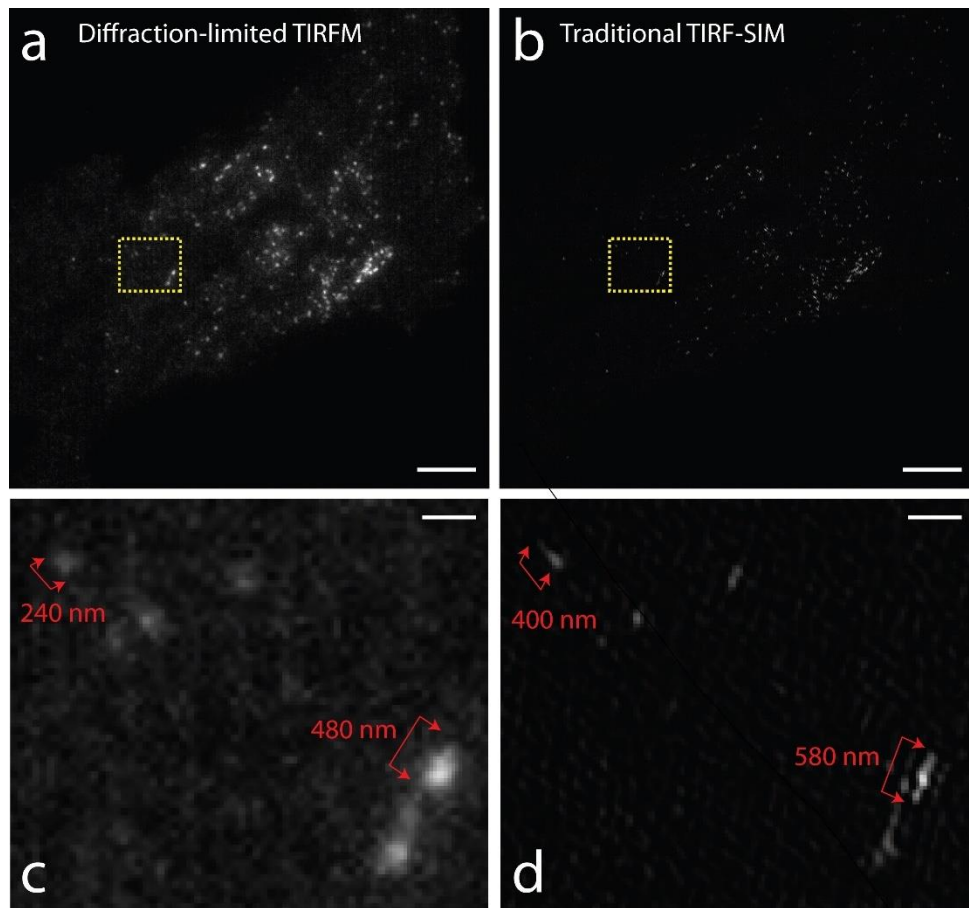


Figure 7.17 Motion blur in Traditional TIRF-SIM

Supplementary Figure 15: EGFP-Rab11 particles in U2OS cells were imaged at 37°C on a commercial TIRF SIM system (9 diffraction-limited images acquired and processed to reconstruct a single super-resolution image) at a frame rate of 12.9 Hz. a) Single raw frame from diffraction-limited series (time point 62 of 200). b) Corresponding TIRF SIM reconstruction. c, d) Higher magnification images of the yellow dashed rectangular regions in a, b. See also Supplementary Video 17. Motion blur broadens particle extent significantly (compare particles highlighted with red arrows, apparent particle width given in red text), presumably due to particle motion during the 9-frame raw image acquisition period (Supplementary Video 18). Scale

bars in a, b 5  $\mu\text{m}$ ; in c, d 500 nm. Experiments were repeated at least 3 times with similar results; representative data are shown.

## Bibliography

- [1] A. J. Ridley *et al.*, “Cell Migration: Integrating Signals from Front to Back,” *Science*, vol. 302, no. 5651, pp. 1704–1709, Dec. 2003.
- [2] P. Martin, “Wound Healing--Aiming for Perfect Skin Regeneration,” *Science*, vol. 276, no. 5309, pp. 75–81, Apr. 1997.
- [3] R. Farooqui and G. Fenteany, “Multiple rows of cells behind an epithelial wound edge extend cryptic lamellipodia to collectively drive cell-sheet movement,” *J Cell Sci*, vol. 118, no. 1, pp. 51–63, Jan. 2005.
- [4] J. Condeelis, R. H. Singer, and J. E. Segall, “THE GREAT ESCAPE: When Cancer Cells Hijack the Genes for Chemotaxis and Motility,” *Annu. Rev. Cell Dev. Biol.*, vol. 21, no. 1, pp. 695–718, Oct. 2005.
- [5] H. Lodish, A. Berk, S. L. Zipursky, P. Matsudaira, D. Baltimore, and J. Darnell, “The Actin Cytoskeleton,” *Mol. Cell Biol. 4th Ed.*, 2000.
- [6] G. M. Cooper, “Actin, Myosin, and Cell Movement,” *Cell Mol. Approach 2nd Ed.*, 2000.
- [7] T. D. Pollard and G. G. Borisy, “Cellular Motility Driven by Assembly and Disassembly of Actin Filaments,” *Cell*, vol. 112, no. 4, pp. 453–465, Feb. 2003.
- [8] J. A. Theriot, “The Polymerization Motor,” *Traffic*, vol. 1, no. 1, pp. 19–28, Jan. 2000.
- [9] P. K. Mattila and P. Lappalainen, “Filopodia: molecular architecture and cellular functions,” *Nat. Rev. Mol. Cell Biol.*, vol. 9, no. 6, pp. 446–454, Jun. 2008.
- [10] N. Leijnse, L. B. Oddershede, and P. M. Bendix, “Helical buckling of actin inside filopodia generates traction,” *Proc. Natl. Acad. Sci.*, vol. 112, no. 1, pp. 136–141, Jan. 2015.
- [11] H. Yamaguchi and J. Condeelis, “Regulation of the actin cytoskeleton in cancer cell migration and invasion,” *Biochim. Biophys. Acta BBA - Mol. Cell Res.*, vol. 1773, no. 5, pp. 642–652, May 2007.
- [12] M. D. Welch and R. D. Mullins, “Cellular Control of Actin Nucleation,” *Annu. Rev. Cell Dev. Biol.*, vol. 18, no. 1, pp. 247–288, Nov. 2002.
- [13] A. Hall, “Rho GTPases and the Actin Cytoskeleton,” *Science*, vol. 279, no. 5350, pp. 509–514, Jan. 1998.
- [14] P. Friedl and D. Gilmour, “Collective cell migration in morphogenesis, regeneration and cancer,” *Nat. Rev. Mol. Cell Biol.*, vol. 10, no. 7, pp. 445–457, Jul. 2009.
- [15] S. Dramsi and P. Cossart, “Intracellular Pathogens and the Actin Cytoskeleton,” *Annu. Rev. Cell Dev. Biol.*, vol. 14, no. 1, pp. 137–166, 1998.
- [16] J. R. Robbins and J. A. Theriot, “*Listeria monocytogenes* rotates around its long axis during actin-based motility,” *Curr. Biol.*, vol. 13, no. 19, pp. R754–R756, Sep. 2003.
- [17] F. Frischknecht *et al.*, “Actin-based motility of vaccinia virus mimics receptor tyrosine kinase signalling,” *Nature*, vol. 401, no. 6756, pp. 926–929, Oct. 1999.
- [18] L. Blanchoin, R. Boujemaa-Paterski, C. Sykes, and J. Plastino, “Actin Dynamics, Architecture, and Mechanics in Cell Motility,” *Physiol. Rev.*, vol. 94, no. 1, pp. 235–263, Jan. 2014.

- [19] C. E. Chan and D. J. Odde, "Traction Dynamics of Filopodia on Compliant Substrates," *Science*, vol. 322, no. 5908, pp. 1687–1691, Dec. 2008.
- [20] A. I. Teixeira, G. A. Abrams, P. J. Bertics, C. J. Murphy, and P. F. Nealey, "Epithelial contact guidance on well-defined micro- and nanostructured substrates," *J. Cell Sci.*, vol. 116, no. 10, pp. 1881–1892, May 2003.
- [21] C. J. Bettinger, R. Langer, and J. T. Borenstein, "Engineering Substrate Topography at the Micro- and Nanoscale to Control Cell Function," *Angew. Chem. Int. Ed.*, vol. 48, no. 30, pp. 5406–5415, Jul. 2009.
- [22] M. K. Driscoll, X. Sun, C. Guven, J. T. Fourkas, and W. Losert, "Cellular Contact Guidance through Dynamic Sensing of Nanotopography," *ACS Nano*, vol. 8, no. 4, pp. 3546–3555, Apr. 2014.
- [23] S. Fujita, M. Ohshima, and H. Iwata, "Time-lapse observation of cell alignment on nanogrooved patterns," *J. R. Soc. Interface*, vol. 6, no. Suppl 3, pp. S269–S277, Jun. 2009.
- [24] D. A. Lauffenburger and A. F. Horwitz, "Cell Migration: A Physically Integrated Molecular Process," *Cell*, vol. 84, no. 3, pp. 359–369, Feb. 1996.
- [25] T. Bretschneider *et al.*, "The Three-Dimensional Dynamics of Actin Waves, a Model of Cytoskeletal Self-Organization," *Biophys. J.*, vol. 96, no. 7, pp. 2888–2900, Apr. 2009.
- [26] K. Thorn, "A quick guide to light microscopy in cell biology," *Mol. Biol. Cell*, vol. 27, no. 2, pp. 219–222, Jan. 2016.
- [27] G. M. Cooper, "Tools of Cell Biology," *Cell Mol. Approach 2nd Ed.*, 2000.
- [28] S. H. Gage, "Modern Dark-Field Microscopy and the History of Its Development," *Trans. Am. Microsc. Soc.*, vol. 39, no. 2, pp. 95–141, 1920.
- [29] F. Zernike, "Phase contrast, a new method for the microscopic observation of transparent objects," *Physica*, vol. 9, no. 7, pp. 686–698, Jul. 1942.
- [30] W. Lang, "Nomarski differential interference-contrast microscopy," p. 8.
- [31] G. E. Murphy and G. J. Jensen, "Electron Cryotomography," *BioTechniques*, vol. 43, no. 4, pp. 413–421, Oct. 2007.
- [32] A. J. Koster and J. Klumperman, "Electron microscopy in cell biology: integrating structure and function," p. 5.
- [33] S. Inoué, *Handbook of Biological Confocal Microscopy*. Springer, 2006.
- [34] J. W. Lichtman and J.-A. Conchello, "Fluorescence microscopy," *Nat. Methods*, vol. 2, no. 12, pp. 910–919, Dec. 2005.
- [35] K. G. Porter and Y. S. Feig, "The use of DAPI for identifying and counting aquatic microflora," *Limnol. Oceanogr.*, vol. 25, no. 5, pp. 943–948, Sep. 1980.
- [36] M. Chalfie, Y. Tu, G. Euskirchen, W. W. Ward, and D. C. Prasher, "Green fluorescent protein as a marker for gene expression," *Science*, vol. 263, no. 5148, pp. 802–805, Feb. 1994.
- [37] "The Nobel Prize in Chemistry 2008," *NobelPrize.org*. [Online]. Available: <https://www.nobelprize.org/prizes/chemistry/2008/summary/>. [Accessed: 31-Oct-2018].
- [38] J. Riedl *et al.*, "Lifeact: a versatile marker to visualize F-actin," *Nat. Methods*, vol. 5, no. 7, p. 605, Jul. 2008.

- [39] E. Wulf, A. Deboben, F. A. Bautz, H. Faulstich, and T. Wieland, “Fluorescent phallotoxin, a tool for the visualization of cellular actin,” *Proc. Natl. Acad. Sci.*, vol. 76, no. 9, pp. 4498–4502, Sep. 1979.
- [40] R. Y. Tsien and A. Waggoner, “Fluorophores for Confocal Microscopy,” in *Handbook of Biological Confocal Microscopy*, J. B. Pawley, Ed. Boston, MA: Springer US, 1995, pp. 267–279.
- [41] X. Tang, S. A. Lancelle, and P. K. Hepler, “Fluorescence microscopic localization of actin in pollen tubes: Comparison of actin antibody and phalloidin staining,” *Cell Motil.*, vol. 12, no. 4, pp. 216–224, Jan. 1989.
- [42] P. L. Felgner *et al.*, “Lipofection: a highly efficient, lipid-mediated DNA-transfection procedure,” *Proc. Natl. Acad. Sci.*, vol. 84, no. 21, pp. 7413–7417, Nov. 1987.
- [43] H. Potter and R. Heller, “Transfection by Electroporation,” *Curr. Protoc. Mol. Biol. Ed. Frederick M Ausubel Al*, vol. CHAPTER, p. Unit-9.3, May 2003.
- [44] L. Song, E. J. Hennink, I. T. Young, and H. J. Tanke, “Photobleaching kinetics of fluorescein in quantitative fluorescence microscopy,” *Biophys. J.*, vol. 68, no. 6, pp. 2588–2600, Jun. 1995.
- [45] V. Magidson and A. Khodjakov, “Circumventing photodamage in live-cell microscopy,” *Methods Cell Biol.*, vol. 114, 2013.
- [46] G. Ball, R. M. Parton, R. S. Hamilton, and I. Davis, “A cell biologist’s guide to high resolution imaging,” *Methods Enzymol.*, vol. 504, pp. 29–55, 2012.
- [47] L. Schermelleh, R. Heintzmann, and H. Leonhardt, “A guide to super-resolution fluorescence microscopy,” *J. Cell Biol.*, vol. 190, no. 2, pp. 165–175, Jul. 2010.
- [48] J. Howard, “Molecular motors: structural adaptations to cellular functions,” *Nature*, vol. 389, no. 6651, pp. 561–567, Oct. 1997.
- [49] B. Innocenti, V. Parpura, and P. G. Haydon, “Imaging Extracellular Waves of Glutamate during Calcium Signaling in Cultured Astrocytes,” *J. Neurosci.*, vol. 20, no. 5, pp. 1800–1808, Mar. 2000.
- [50] Abbe, Ernst, “Beiträge zur Theorie des Mikroskops und der mikroskopischen Wahrnehmung,” *Arch. Für Mikrosk. Anat.*, vol. 9, no. 1, pp. 413–418, 1873.
- [51] B. Huang, M. Bates, and X. Zhuang, “Super resolution fluorescence microscopy,” *Annu. Rev. Biochem.*, vol. 78, pp. 993–1016, 2009.
- [52] B. Huang, H. Babcock, and X. Zhuang, “Breaking the Diffraction Barrier: Super-Resolution Imaging of Cells,” *Cell*, vol. 143, no. 7, pp. 1047–1058, Dec. 2010.
- [53] E. H. Sygne, “XXXVIII. A suggested method for extending microscopic resolution into the ultra-microscopic region,” *Lond. Edinb. Dublin Philos. Mag. J. Sci.*, vol. 6, no. 35, pp. 356–362, Aug. 1928.
- [54] E. A. Ash and G. Nicholls, “Super-resolution Aperture Scanning Microscope,” *Nature*, vol. 237, no. 5357, pp. 510–512, Jun. 1972.
- [55] E. Betzig, A. Lewis, A. Harootunian, M. Isaacson, and E. Kratschmer, “Near Field Scanning Optical Microscopy (NSOM),” *Biophys. J.*, vol. 49, no. 1, pp. 269–279, Jan. 1986.
- [56] A. Lewis, M. Isaacson, A. Harootunian, and A. Muray, “Development of a 500 Å spatial resolution light microscope: I. light is efficiently transmitted through  $\lambda/16$  diameter apertures,” *Ultramicroscopy*, vol. 13, no. 3, pp. 227–231, Jan. 1984.

- [57] W. Lukosz, "Optical Systems with Resolving Powers Exceeding the Classical Limit\*," *JOSA*, vol. 56, no. 11, pp. 1463–1471, Nov. 1966.
- [58] C. Sheppard, "Super-resolution in confocal imaging," *Opt. - Int. J. Light Electron Opt.*, vol. 80, p. 53, Feb. 1988.
- [59] S. W. Hell and J. Wichmann, "Breaking the diffraction resolution limit by stimulated emission: stimulated-emission-depletion fluorescence microscopy," *Opt. Lett.*, vol. 19, no. 11, p. 780, Jun. 1994.
- [60] R. Heintzmann and C. G. Cremer, "Laterally modulated excitation microscopy: improvement of resolution by using a diffraction grating," presented at the BiOS Europe '98, Stockholm, Sweden, 1999, pp. 185–196.
- [61] "The Nobel Prize in Chemistry 2014," *NobelPrize.org*. [Online]. Available: <https://www.nobelprize.org/prizes/chemistry/2014/summary/>. [Accessed: 02-Nov-2018].
- [62] S. W. Hell, "Far-Field Optical Nanoscopy," *Science*, vol. 316, no. 5828, pp. 1153–1158, May 2007.
- [63] E. Betzig *et al.*, "Imaging Intracellular Fluorescent Proteins at Nanometer Resolution," *Science*, vol. 313, no. 5793, pp. 1642–1645, Sep. 2006.
- [64] M. J. Rust, M. Bates, and X. Zhuang, "Stochastic optical reconstruction microscopy (STORM) provides sub-diffraction-limit image resolution," *Nat. Methods*, vol. 3, no. 10, pp. 793–795, Oct. 2006.
- [65] K. Wicker, "Super-Resolution Fluorescence Microscopy Using Structured Illumination," in *Super-Resolution Microscopy Techniques in the Neurosciences*, E. F. Fornasiero and S. O. Rizzoli, Eds. Totowa, NJ: Humana Press, 2014, pp. 133–165.
- [66] M. G. L. Gustafsson, "Surpassing the lateral resolution limit by a factor of two using structured illumination microscopy," *J. Microsc.*, vol. 198, no. 2, pp. 82–87, May 2000.
- [67] C. B. Müller and J. Enderlein, "Image Scanning Microscopy," *Phys. Rev. Lett.*, vol. 104, no. 19, p. 198101, May 2010.
- [68] F. Ströhl and C. F. Kaminski, "Frontiers in structured illumination microscopy," *Optica*, vol. 3, no. 6, pp. 667–677, Jun. 2016.
- [69] A. G. York *et al.*, "Resolution Doubling in Live, Multicellular Organisms via Multifocal Structured Illumination Microscopy," *Nat. Methods*, vol. 9, no. 7, pp. 749–754, May 2012.
- [70] A. G. York *et al.*, "Instant super-resolution imaging in live cells and embryos via analog image processing," *Nat. Methods*, vol. 10, no. 11, pp. 1122–1126, Nov. 2013.
- [71] G. M. R. De Luca *et al.*, "Re-scan confocal microscopy: scanning twice for better resolution," *Biomed. Opt. Express*, vol. 4, no. 11, pp. 2644–2656, Oct. 2013.
- [72] D. Axelrod, "Total Internal Reflection Fluorescence Microscopy in Cell Biology," *Traffic*, vol. 2, no. 11, pp. 764–774, Nov. 2001.
- [73] P. Kner, B. B. Chhun, E. R. Griffis, L. Winoto, and M. G. L. Gustafsson, "Super-resolution video microscopy of live cells by structured illumination," *Nat. Methods*, vol. 6, no. 5, pp. 339–342, May 2009.
- [74] R. Fiolka, M. Beck, and A. Stemmer, "Structured illumination in total internal reflection fluorescence microscopy using a spatial light modulator," *Opt. Lett.*, vol. 33, no. 14, pp. 1629–1631, Jul. 2008.

- [75] D. J. Stephens and V. J. Allan, “Light Microscopy Techniques for Live Cell Imaging,” *Science*, vol. 300, no. 5616, pp. 82–86, Apr. 2003.
- [76] J. Huisken, J. Swoger, F. D. Bene, J. Wittbrodt, and E. H. K. Stelzer, “Optical Sectioning Deep Inside Live Embryos by Selective Plane Illumination Microscopy,” *Science*, vol. 305, no. 5686, pp. 1007–1009, Aug. 2004.
- [77] M. Weber and J. Huisken, “Light sheet microscopy for real-time developmental biology,” *Curr. Opin. Genet. Dev.*, vol. 21, no. 5, pp. 566–572, Oct. 2011.
- [78] E. Baumgart and U. Kubitscheck, “Scanned light sheet microscopy with confocal slit detection,” *Opt. Express*, vol. 20, no. 19, pp. 21805–21814, Sep. 2012.
- [79] P. Saggau, “New methods and uses for fast optical scanning,” *Curr. Opin. Neurobiol.*, vol. 16, no. 5, pp. 543–550, Oct. 2006.
- [80] I. Veilleux, J. A. Spencer, D. P. Biss, D. Cote, and C. P. Lin, “In Vivo Cell Tracking With Video Rate Multimodality Laser Scanning Microscopy,” *IEEE J. Sel. Top. Quantum Electron.*, vol. 14, no. 1, pp. 10–18, Jan. 2008.
- [81] V. Iyer *et al.*, “Acousto-optic multiphoton laser scanning microscopy (AO-MPLSM) for structural and functional imaging in living brain slices,” in *Multiphoton Microscopy in the Biomedical Sciences V*, 2005, vol. 5700, pp. 90–102.
- [82] W. Piyawattanametha *et al.*, “Fast-scanning two-photon fluorescence imaging based on a microelectromechanical systems two-dimensional scanning mirror,” *Opt. Lett.*, vol. 31, no. 13, pp. 2018–2020, Jul. 2006.
- [83] W. Piyawattanametha *et al.*, “3-D Near-Infrared Fluorescence Imaging Using an MEMS-Based Miniature Dual-Axis Confocal Microscope,” *IEEE J. Sel. Top. Quantum Electron.*, vol. 15, no. 5, pp. 1344–1350, Sep. 2009.
- [84] J. Faix and K. Rottner, “The making of filopodia,” *Curr. Opin. Cell Biol.*, vol. 18, no. 1, pp. 18–25, Feb. 2006.
- [85] P. Weiss and B. Garber, “Shape and Movement of Mesenchyme Cells as Functions of the Physical Structure of the Medium: Contributions to a Quantitative Morphology,” *Proc. Natl. Acad. Sci.*, vol. 38, no. 3, pp. 264–280, Mar. 1952.
- [86] W. A. Loesberg *et al.*, “The threshold at which substrate nanogroove dimensions may influence fibroblast alignment and adhesion,” *Biomaterials*, vol. 28, no. 27, pp. 3944–3951, Sep. 2007.
- [87] E. K. F. Yim, R. M. Reano, S. W. Pang, A. F. Yee, C. S. Chen, and K. W. Leong, “Nanopattern-induced changes in morphology and motility of smooth muscle cells,” *Biomaterials*, vol. 26, no. 26, pp. 5405–5413, Sep. 2005.
- [88] X. Sun, M. J. Hourwitz, E. M. Baker, B. U. S. Schmidt, W. Losert, and J. T. Fourkas, “Replication of biocompatible, nanotopographic surfaces,” *Sci. Rep.*, vol. 8, no. 1, p. 564, Jan. 2018.
- [89] M. G. Vicker, “Eukaryotic Cell Locomotion Depends on the Propagation of Self-Organized Reaction–Diffusion Waves and Oscillations of Actin Filament Assembly,” *Exp. Cell Res.*, vol. 275, no. 1, pp. 54–66, Apr. 2002.
- [90] J. Allard and A. Mogilner, “Traveling waves in actin dynamics and cell motility,” *Curr. Opin. Cell Biol.*, vol. 25, no. 1, pp. 107–115, Feb. 2013.
- [91] C. M. Ketchum *et al.*, “Subcellular topography modulates actin dynamics and signaling in B-cells,” *Mol. Biol. Cell*, vol. 29, no. 14, pp. 1732–1742, May 2018.

- [92] W. M. Morton, K. R. Ayscough, and P. J. McLaughlin, “Latrunculin alters the actin-monomer subunit interface to prevent polymerization,” *Nat. Cell Biol.*, vol. 2, no. 6, pp. 376–378, Jun. 2000.
- [93] G. Gerisch *et al.*, “Mobile Actin Clusters and Traveling Waves in Cells Recovering from Actin Depolymerization,” *Biophys. J.*, vol. 87, no. 5, pp. 3493–3503, Nov. 2004.
- [94] L. B. Case and C. M. Waterman, “Adhesive F-actin Waves: A Novel Integrin-Mediated Adhesion Complex Coupled to Ventral Actin Polymerization,” *PLOS ONE*, vol. 6, no. 11, p. e26631, Nov. 2011.
- [95] M. Fritzsche *et al.*, “Cytoskeletal actin dynamics shape a ramifying actin network underpinning immunological synapse formation,” *Sci. Adv.*, vol. 3, no. 6, p. e1603032, Jun. 2017.
- [96] L. Bozec, G. van der Heijden, and M. Horton, “Collagen Fibrils: Nanoscale Ropes,” *Biophys. J.*, vol. 92, no. 1, pp. 70–75, Jan. 2007.
- [97] S. Maruo and J. T. Fourkas, “Recent progress in multiphoton microfabrication,” *Laser Photonics Rev.*, vol. 2, no. 1–2, pp. 100–111, Apr. 2008.
- [98] L. Lu, S. J. Oswald, H. Ngu, and F. C.-P. Yin, “Mechanical Properties of Actin Stress Fibers in Living Cells,” *Biophys. J.*, vol. 95, no. 12, pp. 6060–6071, Dec. 2008.
- [99] T. Gutschmann *et al.*, “Evidence that Collagen Fibrils in Tendons Are Inhomogeneously Structured in a Tubelike Manner,” *Biophys. J.*, vol. 84, no. 4, pp. 2593–2598, Apr. 2003.
- [100] Han, Sejin, “TYPE I COLLAGEN HOMOTRIMERS; THEIR ROLE IN COLLAGEN FIBRIL FORMATION AND TISSUE REMODELING.”
- [101] S. R. H. Barrett, M. P. F. Sutcliffe, S. Howarth, Z. Li, and J. H. Gillard, “Experimental measurement of the mechanical properties of carotid atherothrombotic plaque fibrous cap,” *J. Biomech.*, vol. 42, no. 11, pp. 1650–1655, Aug. 2009.
- [102] E. Meijering, O. Dzyubachyk, and I. Smal, “Chapter nine - Methods for Cell and Particle Tracking,” in *Methods in Enzymology*, vol. 504, P. M. Conn, Ed. Academic Press, 2012, pp. 183–200.
- [103] B. K. P. Horn and B. G. Schunck, “Determining optical flow,” *Artif. Intell.*, vol. 17, no. 1, pp. 185–203, Aug. 1981.
- [104] V. Ulman and P. Matula, *ESTIMATING LARGE LOCAL MOTION IN LIVE-CELL IMAGING USING VARIATIONAL OPTICAL FLOW Towards Motion Tracking in Live Cell Imaging Using Optical Flow*. .
- [105] J. Delpiano, J. Jara, J. Scheer, O. A. Ramírez, J. Ruiz-del-Solar, and S. Härtel, “Performance of optical flow techniques for motion analysis of fluorescent point signals in confocal microscopy,” *Mach. Vis. Appl.*, vol. 23, no. 4, pp. 675–689, Jul. 2012.
- [106] L. Updated, *Internal Tutorial: Computing 2D and 3D Optical Flow*. J.L.Barron and N.A.Thacker. .
- [107] *A Fiji plugin for Curvature Analysis. Contribute to brouhardlab/Kappa development by creating an account on GitHub*. Brouhard Lab, 2018.
- [108] J. P. Giannini, A. G. York, and H. Shroff, “Anticipating, measuring, and minimizing MEMS mirror scan error to improve laser scanning microscopy’s speed and accuracy,” *PLOS ONE*, vol. 12, no. 10, p. e0185849, Oct. 2017.

- [109] W. Göbel, B. M. Kampa, and F. Helmchen, “Imaging cellular network dynamics in three dimensions using fast 3D laser scanning,” *Nat. Methods*, vol. 4, no. 1, pp. 73–79, Jan. 2007.
- [110] B. F. Grewe, D. Langer, H. Kasper, B. M. Kampa, and F. Helmchen, “High-speed *in vivo* calcium imaging reveals neuronal network activity with near-millisecond precision,” *Nat. Methods*, vol. 7, no. 5, pp. 399–405, May 2010.
- [111] K. Svoboda and R. Yasuda, “Principles of Two-Photon Excitation Microscopy and Its Applications to Neuroscience,” *Neuron*, vol. 50, no. 6, pp. 823–839, Jun. 2006.
- [112] G. Y. Fan, H. Fujisaki, A. Miyawaki, R.-K. Tsay, R. Y. Tsien, and M. H. Ellisman, “Video-Rate Scanning Two-Photon Excitation Fluorescence Microscopy and Ratio Imaging with Cameleons,” *Biophys. J.*, vol. 76, no. 5, pp. 2412–2420, May 1999.
- [113] V. Iyer, B. E. Losavio, and P. Saggau, “Compensation of spatial and temporal dispersion for acousto-optic multiphoton laser-scanning microscopy,” *J. Biomed. Opt.*, vol. 8, no. 3, pp. 460–472, Jul. 2003.
- [114] X. Lv, C. Zhan, S. Zeng, W. R. Chen, and Q. Luo, “Construction of multiphoton laser scanning microscope based on dual-axis acousto-optic deflector,” *Rev. Sci. Instrum.*, vol. 77, no. 4, p. 046101, Apr. 2006.
- [115] K. H. Kim *et al.*, “Two-axis magnetically-driven MEMS scanning catheter for endoscopic high-speed optical coherence tomography,” *Opt. Express*, vol. 15, no. 26, pp. 18130–18140, Dec. 2007.
- [116] Y. Pan, H. Xie, and G. K. Fedder, “Endoscopic optical coherence tomography based on a microelectromechanical mirror,” *Opt. Lett.*, vol. 26, no. 24, pp. 1966–1968, Dec. 2001.
- [117] D. L. Dickensheets and G. S. Kino, “Micromachined scanning confocal optical microscope,” *Opt. Lett.*, vol. 21, no. 10, pp. 764–766, May 1996.
- [118] L. Fu, A. Jain, H. Xie, C. Cranfield, and M. Gu, “Nonlinear optical endoscopy based on a double-clad photonic crystal fiber and a MEMS mirror,” *Opt. Express*, vol. 14, no. 3, p. 1027, Feb. 2006.
- [119] A. Kumar *et al.*, “Dual-view plane illumination microscopy for rapid and spatially isotropic imaging,” *Nat. Protoc.*, vol. 9, no. 11, pp. 2555–2573, Nov. 2014.
- [120] K. J. Åström and T. Hägglund, “The future of PID control,” *Control Eng. Pract.*, vol. 9, no. 11, pp. 1163–1175, Nov. 2001.
- [121] Veljko Milanović, Abhishek Kasturi, James Yang, and Frank Hu, “Closed-loop control of gimbal-less MEMS mirrors for increased bandwidth in LiDAR applications,” 2017, vol. 10191, pp. 101910N-10191–13.
- [122] L. Landweber, “An Iteration Formula for Fredholm Integral Equations of the First Kind,” *Am. J. Math.*, vol. 73, no. 3, pp. 615–624, 1951.
- [123] M. Guo *et al.*, “Single-shot super-resolution total internal reflection fluorescence microscopy,” *Nat. Methods*, vol. 15, no. 6, pp. 425–428, Jun. 2018.
- [124] Poulter, N. S., Pitkeathly, W. T. E., Smith, P. J. & Rappoport, J. Z, *Advanced Fluorescence Microscopy: Methods and Protocols*, vol. Vol. 1251. Springer, New York, 2015.

- [125] R. Fiolka, M. Beck, and A. Stemmer, “Structured illumination in total internal reflection fluorescence microscopy using a spatial light modulator,” *Opt. Lett.*, vol. 33, no. 14, pp. 1629–1631, Jul. 2008.
- [126] E. Chung, D. Kim, Y. Cui, Y.-H. Kim, and P. T. C. So, “Two-Dimensional Standing Wave Total Internal Reflection Fluorescence Microscopy: Superresolution Imaging of Single Molecular and Biological Specimens,” *Biophys. J.*, vol. 93, no. 5, pp. 1747–1757, Sep. 2007.
- [127] O. Gliko, G. D. Reddy, B. Anvari, W. E. Brownell, and P. Saggau, “Standing wave total internal reflection fluorescence microscopy to measure the size of nanostructures in living cells,” *J. Biomed. Opt.*, vol. 11, no. 6, p. 064013, Nov. 2006.
- [128] D. Li *et al.*, “Extended-resolution structured illumination imaging of endocytic and cytoskeletal dynamics,” *Science*, vol. 349, no. 6251, p. aab3500, Aug. 2015.
- [129] S. Roth, C. J. Sheppard, K. Wicker, and R. Heintzmann, “Optical photon reassignment microscopy (OPRA),” *Opt. Nanoscopy*, vol. 2, no. 1, p. 5, Oct. 2013.
- [130] A. Curd, A. Cleasby, K. Makowska, A. York, H. Shroff, and M. Peckham, “Construction of an instant structured illumination microscope,” *Methods*, vol. 88, pp. 37–47, Oct. 2015.
- [131] A. L. Stout and D. Axelrod, “Evanescent field excitation of fluorescence by epi-illumination microscopy,” *Appl. Opt.*, vol. 28, no. 24, pp. 5237–5242, Dec. 1989.
- [132] T. J. Gould, J. R. Myers, and J. Bewersdorf, “Total internal reflection STED microscopy,” *Opt. Express*, vol. 19, no. 14, pp. 13351–13357, Jul. 2011.
- [133] D. T. Burnette *et al.*, “A contractile and counterbalancing adhesion system controls the 3D shape of crawling cells,” *J Cell Biol*, vol. 205, no. 1, pp. 83–96, Apr. 2014.
- [134] K. A. Sochacki, A. M. Dickey, M.-P. Strub, and J. W. Taraska, “Endocytic proteins are partitioned at the edge of the clathrin lattice in mammalian cells,” *Nat. Cell Biol.*, vol. 19, no. 4, pp. 352–361, Apr. 2017.
- [135] K. Faire, C. M. Waterman-Storer, D. Gruber, D. Masson, E. D. Salmon, and J. C. Bulinski, “E-MAP-115 (ensconsin) associates dynamically with microtubules in vivo and is not a physiological modulator of microtubule dynamics,” *J Cell Sci*, vol. 112, no. 23, pp. 4243–4255, Dec. 1999.
- [136] A. L. Miller and W. M. Bement, “Regulation of cytokinesis by Rho GTPase flux,” *Nat. Cell Biol.*, vol. 11, no. 1, pp. 71–77, Jan. 2009.
- [137] A. Apolloni, I. A. Prior, M. Lindsay, R. G. Parton, and J. F. Hancock, “H-ras but Not K-ras Traffics to the Plasma Membrane through the Exocytic Pathway,” *Mol. Cell. Biol.*, vol. 20, no. 7, pp. 2475–2487, Apr. 2000.
- [138] J. B. Grimm *et al.*, “A general method to improve fluorophores for live-cell and single-molecule microscopy,” *Nat. Methods*, vol. 12, no. 3, pp. 244–250, Mar. 2015.
- [139] J. F. Presley, N. B. Cole, T. A. Schroer, K. Hirschberg, K. J. M. Zaal, and J. Lippincott-Schwartz, “ER-to-Golgi transport visualized in living cells,” *Nature*, vol. 389, no. 6646, pp. 81–85, Sep. 1997.
- [140] E. Choy *et al.*, “Endomembrane Trafficking of Ras: The CAAX Motif Targets Proteins to the ER and Golgi,” *Cell*, vol. 98, no. 1, pp. 69–80, Jul. 1999.

- [141] S. Takahashi *et al.*, “Rab11 regulates exocytosis of recycling vesicles at the plasma membrane,” *J Cell Sci*, vol. 125, no. 17, pp. 4049–4057, Sep. 2012.
- [142] H. Shen *et al.*, “Single Particle Tracking: From Theory to Biophysical Applications,” *Chem. Rev.*, vol. 117, no. 11, pp. 7331–7376, Jun. 2017.
- [143] R. Fiolka, “Clearer view for TIRF and oblique illumination microscopy,” *Opt. Express*, vol. 24, no. 26, pp. 29556–29567, Dec. 2016.
- [144] B. P. Olveczky, N. Periasamy, and A. S. Verkman, “Mapping fluorophore distributions in three dimensions by quantitative multiple angle-total internal reflection fluorescence microscopy,” *Biophys. J.*, vol. 73, no. 5, pp. 2836–2847, Nov. 1997.
- [145] P. W. Winter *et al.*, “Two-photon instant structured illumination microscopy improves the depth penetration of super-resolution imaging in thick scattering samples,” *Optica*, vol. 1, no. 3, p. 181, Sep. 2014.
- [146] A. L. Mattheyses and D. Axelrod, “Direct measurement of the evanescent field profile produced by objective-based total internal reflection fluorescence,” *J. Biomed. Opt.*, vol. 11, no. 1, p. 014006, Jan. 2006.
- [147] Y. Fu, P. W. Winter, R. Rojas, V. Wang, M. McAuliffe, and G. H. Patterson, “Axial superresolution via multiangle TIRF microscopy with sequential imaging and photobleaching,” *Proc. Natl. Acad. Sci.*, vol. 113, no. 16, pp. 4368–4373, Apr. 2016.
- [148] W. H. Richardson, “Bayesian-Based Iterative Method of Image Restoration\*,” *JOSA*, vol. 62, no. 1, pp. 55–59, Jan. 1972.
- [149] L. B. Lucy, “An iterative technique for the rectification of observed distributions,” *Astron. J.*, vol. 79, p. 745, Jun. 1974.
- [150] Kota Miura, Curtis Rueden, Mark Hiner, Johannes Schindelin, and Jens Rietdorf, *ImageJ Plugin CorrectBleach V2.0.2*. Zenodo, 2014.
- [151] D. Li and E. Betzig, “Response to Comment on ‘Extended-resolution structured illumination imaging of endocytic and cytoskeletal dynamics,’” *Science*, vol. 352, no. 6285, pp. 527–527, Apr. 2016.
- [152] P. Thevenaz, U. E. Ruttimann, and M. Unser, “A pyramid approach to subpixel registration based on intensity,” *IEEE Trans. Image Process.*, vol. 7, no. 1, pp. 27–41, Jan. 1998.
- [153] J.-Y. Tinevez *et al.*, “TrackMate: An open and extensible platform for single-particle tracking,” *Methods*, vol. 115, pp. 80–90, Feb. 2017.
- [154] A. Choudhury *et al.*, “Rab proteins mediate Golgi transport of caveola-internalized glycosphingolipids and correct lipid trafficking in Niemann-Pick C cells,” *J. Clin. Invest.*, vol. 109, no. 12, pp. 1541–1550, Jun. 2002.
- [155] M. A. Baird *et al.*, “Local pulsatile contractions are an intrinsic property of the myosin 2A motor in the cortical cytoskeleton of adherent cells,” *Mol. Biol. Cell*, vol. 28, no. 2, pp. 240–251, Nov. 2016.
- [156] F. Gittes, B. Mickey, J. Nettleton, and J. Howard, “Flexural rigidity of microtubules and actin filaments measured from thermal fluctuations in shape,” *J. Cell Biol.*, vol. 120, no. 4, pp. 923–934, Feb. 1993.
- [157] C. M. Winterflood, T. Ruckstuhl, D. Verdes, and S. Seeger, “Nanometer Axial Resolution by Three-Dimensional Supercritical Angle Fluorescence Microscopy,” *Phys. Rev. Lett.*, vol. 105, no. 10, p. 108103, Aug. 2010.

[158] E. J. Botcherby, R. Juškaitis, M. J. Booth, and T. Wilson, “An optical technique for remote focusing in microscopy,” *Opt. Commun.*, vol. 281, no. 4, pp. 880–887, Feb. 2008.